Modeling Friction, Wear and Lubrication of Sliding Polyurethane and Polycarbonate Surfaces Representing Printer Components with Molecular Dynamics

By

Carolyn Joy Carkner

A thesis submitted to the Department of Chemistry

In conformity with the requirements for the

Degree of Master of Science

Queen's University

Kingston, Ontario, Canada

(October, 2013)

Abstract

The Xerox Research Centre of Canada has noted that elastomeric cleaning blades in laser printers have a relatively short life expectancy, as they experience high levels of friction and wear while wiping excess toner from commercial photoconducting drums. As such, there has been interest in examining the behaviour related to friction, wear and lubrication of components in laser printers. Molecular dynamics simulations were employed to gain molecular-level insight into the mechanism of wear of the cleaning blade and the effectiveness of lubricants in reducing friction forces. The Dreiding force field was chosen to simulate representations of the photoconducting drum, cleaning blade and the lubricant. They were modeled in bulk and layered forms, and compressed and sheared to examine slip mechanisms and evaluate shear stresses and friction coefficients. It was found that the polycarbonate (PC) component was significantly stronger than either the polyurethane (PU) or octadecane (C18) components, and that the introduction of an interface and/or C18 lubricating material lowered the measured shear strengths to various degrees. The simulations indicated three different slip mechanisms depending on the nature of system. We have observed that shearing may induce structural changes within the PU component (such as ordering) even without a local slip event, which likely contributes to the eventual mechanical failure of the PU cleaning blade. From the models used in this study, it appears that more lubricating material is required than is currently used in practice in order to prevent wear of the PU cleaning blade. As well, the shear strengths and friction coefficients are not significantly reduced with the addition of lubricant for models containing PU. This is, of course, subject to the limitations of the simulations performed.

Acknowledgements

Recognition should be given to a number of sources of support in this work: my supervisor, Dr. Nicholas Mosey, for the series of computational adventures over the last four years, especially in tribochemistry and tribology, as well as his continual encouragement; my "on-site" supervisor, Dr. Adrien Côté, for inviting our contribution to the research at the Xerox Research Centre of Canada (XRCC), hosting me there, and his enthusiasm for the project; High Performance Computing Virtual Laboratory (HPCVL), SHARCNET and SciNet for computational resources; Queen's University, the Department of Chemistry, the Natural Sciences and Engineering Research Council of Canada (NSERC) and XRCC for financial support; and fellow members of the Mosey group for being a constant source of animated discussions and moral support.

Table of Contents

List of Figures

List of Tables

List of Abbreviations and Symbols

a, b, c: Lattice vectors of the simulation cell

AFM: Atomic Force Microscopy

BPA: Bisphenol-A

C18: Octadecane, or 2 Molecular Layers of Octadecane

2C18: 4 Molecular Layers of Octadecane

CD: Component Distribution

CHELPG: CHarges from Electrostatic Potentials using a Grid based method

FD: Fraction Distribution

FEM: Finite Element Model

FF: Force Field

FFM: Friction Force Microscopy

FIB: Focussed Ion Beam

FTIR: Fourier Transform Infrared Spectroscopy

FWHM: Full Width at Half-Maximum

HF: Hartree-Fock

MD: Molecular Dynamics

NPT: Number, Pressure, and Temperature are fixed

NVE: Number, Volume, and Energy are fixed

NVT: Number, Volume, and Temperature are fixed

OPD: Order Parameter Distribution

PC: Polycarbonate

PU: Polyurethane

QC: Quantum Chemical

S: Order Parameter

SD: Slip Distribution

SFA: Surface Forces Apparatus

TP: Thermoplastic

TS: Thermoset

XRCC: Xerox Research Centre of Canada

σ_{ij}: Stress tensor element (i , j)

τ_c: Critical Shear Strength

Chapter 1: Introduction

1.1 Friction, Wear, and Lubrication of Surfaces

Friction corresponds to a force that must be overcome in order to initiate or maintain motion of one object relative to another. It is a resistive force, in the sense that it always resists motion of the system and is only present when another force acts on the system. Friction between surfaces is a familiar occurrence in our everyday lives, from the smoothness of high thread count bed sheets, to the treads on the bottom of shoes gripping the ground, to the efficient movement of small parts in electronic devices.

There are two categories of friction forces. Static friction is associated with initiating motion between objects, while kinetic friction is associated with keeping one object moving relative to another at a constant velocity. The static friction force is generally larger than the kinetic friction force. Consider moving a stationary car in neutral on a level surface. To initiate the turning of wheels a fair amount of applied force is required, but once the motion has begun, less force is required to maintain the motion. The presence of friction requires the continual application of external forces to keep objects in relative motion, which in turn requires the input of energy. As objects slide, this energy is used to overcome friction and is dissipated into the material. As such, high friction in devices is associated with higher energy demands. In addition to the forces and energy demands associated with friction, the relative motion of surfaces can lead to changes in the structure of the underlying materials. These structural changes can range from irreversible alterations in the local bonding between atoms to the loss of material from the surfaces that are in contact. These structural changes all correspond to forms of wear, and are undesirable from the standpoint of device longevity and functionality. While wear can occur whenever surfaces move relative to each other, the presence of high friction often leads to higher

degrees of wear because the system must be subjected to higher forces in order for motion to occur.

Overall, friction and wear can have significant economic and environmental impacts. The increased energy requirements associated with high friction place greater demands on energy resources, with increased costs. Meanwhile, wear can lead to the premature failure of devices, which increases waste and introduces replacement costs. The US Department of Energy stated that "in highly industrialized nations, the total annual cost of friction- and wear-related energy and material losses is estimated to be 5% - 7% of national gross domestic product" [1]. The Energy Systems Division of the same laboratory also noted that "in passenger cars, one-third of the fuel energy is used to overcome friction in the engine, transmission, tires, and brakes. The direct frictional losses, with braking friction excluded, are 28% of the fuel energy" [2]. The concerns regarding energy costs and material loss apply to countless other devices, including printer components, which are of interest in this project.

Friction has been studied for millennia, from at least as early as the lubrication of rollers with animal fat (ancient Egypt and Mesopotamia). Studies by da Vinci (1452-1519) and Amontons (1699) using systems consisting of metal plates pulled by springs on wooden surfaces led to the basic law of friction, called Amontons's law, which is still used today:

$$F = \mu L \qquad \text{(Eq. 1.1)}$$

where F corresponds to the friction force, i.e. the force that must be applied along the direction of motion to initiate or maintain motion, L corresponds to a load acting normal to the interface between the two surfaces that are in motion and μ is called the coefficient of friction. It is important to note that this law indicates that the friction force is independent of the area over which the load is applied and does not depend on sliding velocity. Deviations to both these

outcomes of Amontons's law are known, particularly in the presence of adhesive interactions between the two surfaces in contact, at low length scales, and at high sliding velocity. Nonetheless, this law does describe friction quite accurately in size and velocity regimes that are relevant to most practical applications.

Amontons's law is based on a completely macroscopic view of the surfaces in contact. However, it is known that surfaces are quite rough at the microscopic scale, will small 'hills' called asperities being present at the surface, as shown in Figure 1.1. When two surfaces are brought into contact, the interface between them corresponds to the points at which their asperities touch. The surface area associated with these contact points is much lower than the apparent macroscopic area of the interface. The forces and loads to which the system is subjected during sliding are supported by the small areas associated with the contact points between asperities, which can lead to tremendous local stresses on the order of several gigapascals that reach the shear and compressive strengths of the materials in the contacts. In addition, the dissipation of the energy used to initiate or maintain sliding at these contact points can lead to local temperatures on the order of thousands of Kelvin. These extreme conditions can induce a wide range of chemical reactions, called tribochemical reactions. These reactions can alter surface structures, leading to behaviours ranging from wear to wear inhibition.

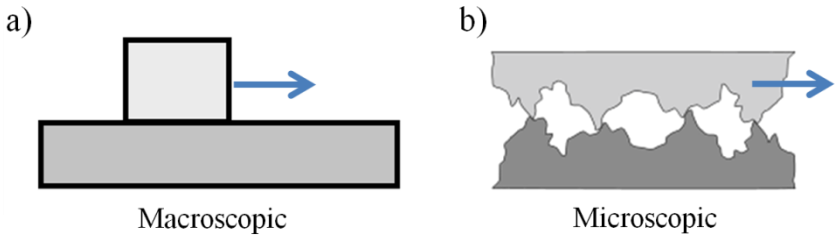

Figure 1.1. Two views of surfaces sliding past each other, on (a) the macroscopic and (b) the microscopic level.

The microscopic view of the interfaces between surfaces in relative motion indicates that friction and wear are dictated by the behaviours of these interfaces at the points where asperities

come into contact with one another. The main strategy used to modulate this behaviour involves introducing lubricants that inhibit asperities from coming into contact with one another, and, depending on the specific details of the lubricants, may also alter the mechanical and chemical properties of the system at the points of asperity contacts. The development of improved lubricants, and indeed the development of a better understanding of friction and wear, can be enhanced by gaining a better understanding of the conditions and processes that occur at the points of asperity contact in sliding interfaces. This has motivated several experimental and theoretical studies into the details of these processes.

1.2 Experimental Methods and Studies

A number of experimental techniques currently exist with the intention of developing a better understanding of friction, wear, and the effects of lubrication. Friction on a surface can be reproduced by sliding a second material (frequently, but not always in the form of a sharp tip) across the surface. Wear can similarly be reproduced if the second material is able to etch the surface and create grooves, which can be subsequently measured. To accurately measure friction and wear of a surface, the devices must have very high resolution and precise movement capabilities.

Atomic force microscopy (AFM) is one of the most widely used experimental methods for studying surfaces and friction forces at the micro- and nanoscopic scales. A basic schematic of an AFM is given in Figure 1.2. As shown in the figure, the AFM corresponds to a microscopically sharp tip that can be displaced vertically with respect to a surface. A laser beam is deflected off a cantilever holding the tip to determine the position of the tip relative to the surface. By moving the tip over the surface, one can construct a height map that provides insight into details such as surface roughness, asperity size and asperity density. Meanwhile, if the force

constant of the cantilever is known in addition to the deflection, one can measure the forces associated with the interaction between the tip and the surface. Such information can be used to obtain friction forces.

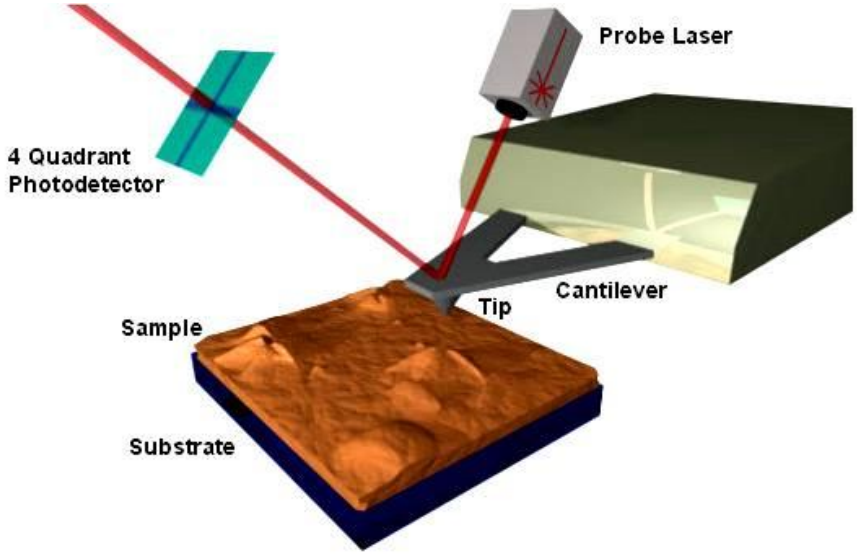

Figure 1.2. A schematic of an AFM setup [3]. As the tip runs along the surface, the laser beam is deflected to the photodetector which monitors its position.

In order to understand the source of friction forces, it is of interest to image the morphology of the surfaces being subjected to these forces. The accurate control of AFM tips allows objects as small as atomic surface asperities to be viewed. A common hindrance of high resolution imaging with AFM is that the tip may disrupt the location of the particles in the process of measurement. For such sensitive measurements, the AFM may be used in non-contact mode, in which the tip is functionalized and can detect attraction to or repulsion from the material. An example of AFM imaging using non-contact mode is shown in Figure 1.3 [4]. The images of pentacene shown in this figure were obtained by using a functionalized AFM tip held at a constant height and amplitude of oscillation over the sample, while the measured frequency of oscillation varied depending on the region over which the tip was being held. This imaging technique was sufficiently resolved to image the carbon-hydrogen bonds. In another study, the AFM has been enhanced to operate in a mode gentle enough so as to not damage living cells

during imaging [5], while in other cases, advancements have been made in three-dimensional AFM imaging [6].

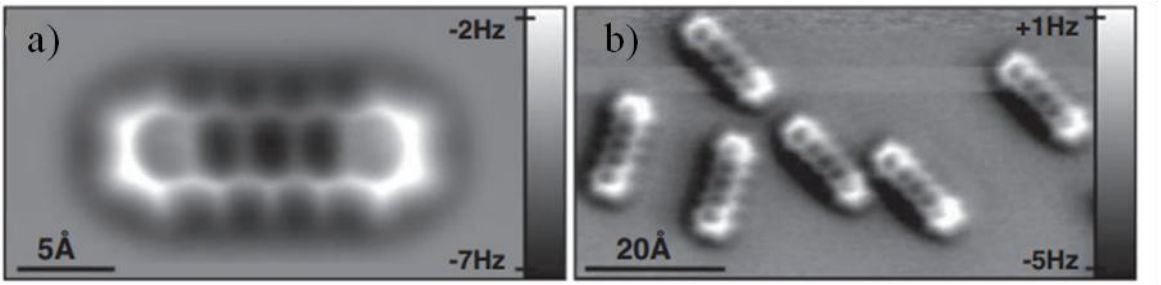

Figure 1.3. Pentacene imaged with AFM on Cu(111) [4]. a) A single pentacene molecule. The experienced frequency shift (Δf) ranged from about -7 to -2 Hz for the image taken with a particular tip height and oscillation amplitude of 0.2 Å. b) Six pentacene molecules. A Δf range of about -5 to +1 Hz taken at a height 0.1 Å higher than that of (a), and an oscillation amplitude of 0.8 Å.

The depth of asperities on a surface is another important detail that can be captured via AFM imaging. With a sufficiently thin AFM tip, deep grooves in a surface may also be measured. Figure 1.4 contains an example of groove depth measurement performed by AFM [7]. The surfaces are composed of bare silicon and platinum deposited on silicon, and the grooves are machined onto the surfaces with a focused ion beam (FIB). These grooves ranged in depth from about 3 to 49 nm. Surface morphologies have also been studied by AFM to gain insights such as the effects of chemical changes to the surfaces [8,9], and effectiveness of adsorption [10].

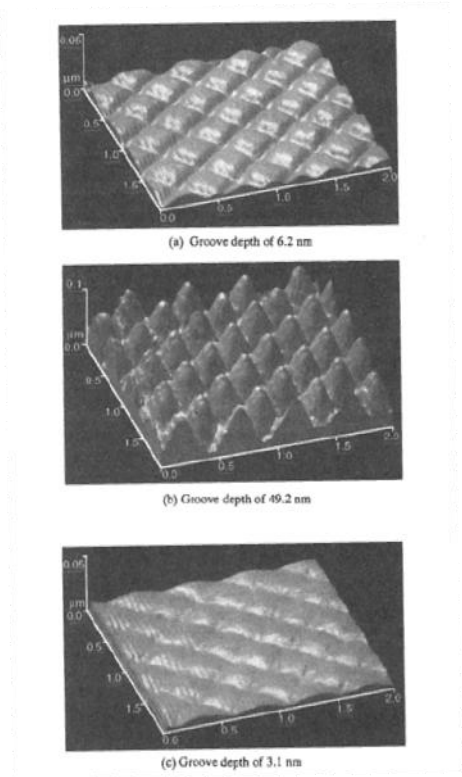

Figure 1.4. AFM image of silicon wafers with machined patterns [7]. The groove depths are (a) 6.2 nm, (b) 49.2 nm, and (c) 3.1 nm.

Though the structure of a surface can give insight to how a material might interact with it, a more direct method would be to directly measure the forces between a material and the surface. AFMs are often equipped to measure surface forces. When used to measure the forces associated with lateral motion of the tip over a surface, these force measurements are referred to as friction force microscopy (FFM). To measure surface forces, the cantilever on which the tip is attached is controlled in an oscillating fashion, while the gap between the tip and the sample is measured and force-distance relationships are obtained. This approach is able to measure forces as low as tens of piconewtons. The direct relationship between silicon asperity height and friction forces was examined with the AFM in the same study used to generate the images in Figure 1.4 [7]. Particularly, the pull-off forces and friction forces with respect to curvature radius of the asperities was plotted. As the groove depth increased, the pull-off force and friction force decreased for both the bare silicon and platinum deposited surfaces. Such measurements of pull-

off forces may be performed in humid conditions or completely submerged in a liquid, and may be measured while stretching single molecules [11,12,13].

Though AFMs are more common, a surface forces apparatus (SFA) is a more direct method for studying how two surfaces interact with each other. A schematic of a SFA is provided in Figure 1.5. Instead of a tip controlled over a surface, an entire other surface is manoeuvred with piezoelectrics with respect to the first surface, such that friction forces may be directly measured. The two surfaces are cylindrical and held perpendicular to each other, such that a relatively small contact area is achieved. The provided image is for a particular application with a solvent suspended between the surfaces. The resolution is comparable to AFM, and the measured forces are similarly on the order of tens of piconewtons.

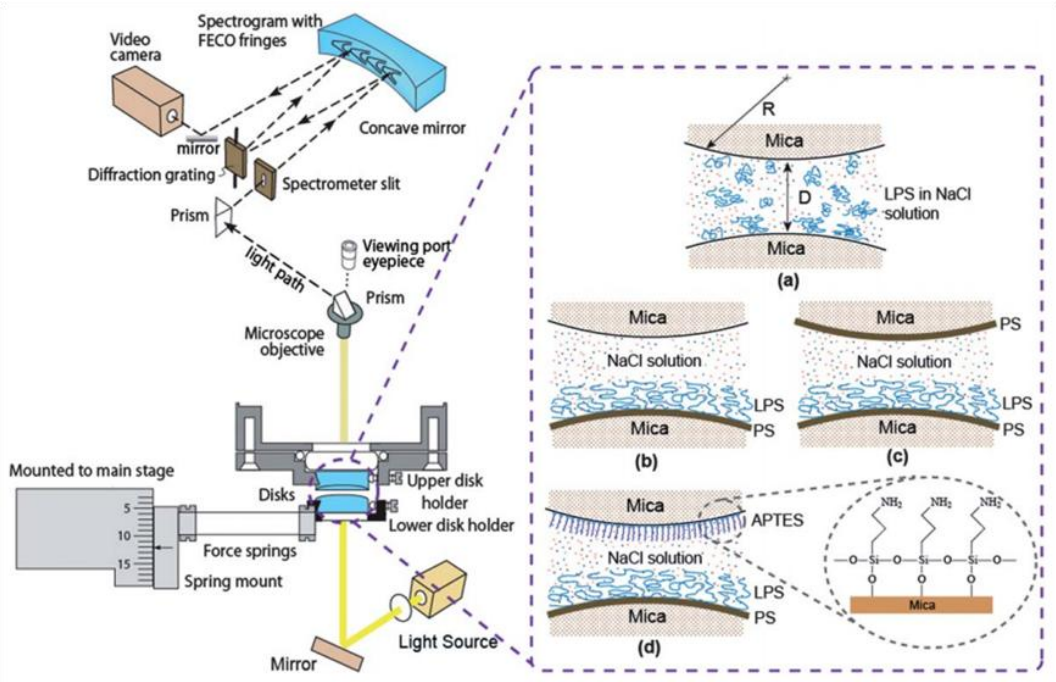

Figure 1.5. A schematic of a SFA [14]. The two surfaces, functionalized in this example with combinations of lipopolysaccharides (LPS), polystyrene (PS), or 3-aminopropyltriethyloxysilane (APTES), are accurately controlled in all three dimensions, and the responsive forces are directly measured.

The interaction forces of surfaces change when the compositions and/or morphologies of surfaces in contact are changed. One study with SFA involved measuring friction between glass

surfaces coated with a monolayer of one of two self-assembling materials, being either phenyltrichlorosilane or benzyltrichlorosilane [15]. The surfaces were found to exhibit low adhesion when coated in a monolayer of either material. Though there are large differences in contact area, load, and pressure, the measured coefficients of friction were found to compare very well to those measured by FFM. Additionally, no strong velocity-dependence was observed for the friction forces. These SFA machines have many techniques associated with them, allowing for electrochemical applications [16,17], and lend themselves very well toward measurements requiring liquid suspended between the surfaces [18,19].

As mentioned earlier, surfaces frequently experience a form of wear when they encounter friction forces. Since there is limited standardization, reproducing wear on the macroscopic scale may be done by any number of case-specific methods, selected to best represent the original scenario. Whatever material, load, direction and rate of motion are best-suited for the situation may be customized. On the other hand, when studying wear on the microscopic scale, only a few methods are available. In a recent review of nano-scale wear [20], the most popular instrument was AFM or a similar mechanism with an alternate tip material. Many properties related to wear are available this way, including wear type, wear coefficient, wear volume, hardness, and atom removal energy barrier.

As alluded to earlier, there are cases where local conditions become so extreme that reactions are induced between surfaces, and this is called a tribochemical reaction. In one tribochemical study [21], stearic acid was dip-coated onto a copper surface supported by a silicon wafer. Both after time and heating, the stearic acid was observed to adsorb to the metal surface, as confirmed by FTIR. When the surface was nanoplowed (groove depths of 30 to 40 nm) after coating, the FTIR results suggested that similar adsorbed structures were being

produced, and that the concentration of adsorbed substance as compared to unadsorbed substance increased as the scratch density increased. It was concluded that the act of nanoplowing encouraged the functionalization of the copper surface. Other studies have even observed the oxidation of hydrocarbons [22]. These reactions occur when oil-soluble metal particles are worn off of the surface and can more readily react with the lubricating hydrocarbons.

To lower friction forces and the effects of wear, lubricants are typically added to surfaces for protection. A standard test for measuring the effectiveness of a lubricant is the four-ball test. In short, the test involves rotating one steel ball on a triangle of three stationary balls. The ball may be rotated at a range of loads and speeds for a length of time, while the other three are submerged in whatever lubricant is being tested. At the end of the test, a "wear scar" is formed on each of the three stationary balls, and the diameter of the scar may be measured. This test was used in one study considering zinc borate as an additive in oil as a lubricant [23]. Oil is known for its lubricating properties, so the oil without additive was tested, as well as with additive for a lower and higher pair of load and time variables. For both sets of conditions, the oil with the zinc borate additive created a smaller wear scar with a diameter about 10% smaller than that of the base oil. Upon analysis of the wear scar, it appeared that the additive may have protected the surface by depositing a boron compound onto it, since a substantial amount of the element was found there, though with a distinct absence of zinc. There exist entire reviews on many types of lubricants and applications, including lubrication of hip joints [24], materials in biodiesel [25], and green ionic liquids [26].

1.3 Theoretical Methods and Studies

The experimental methods discussed above have proven very useful in the context of studying surface structure, friction, wear and the effectiveness of lubricants. However, the length

and time resolutions of these techniques are not adequate to determine the atomic-level mechanisms associated with wear occurring in sliding contacts. As such, numerous theoretical techniques have been developed to examine sliding contacts at small length and time scales. These techniques fall into four general categories depicted in Figure 1.6, which were largely determined by the power of computational resources at the time of their development.

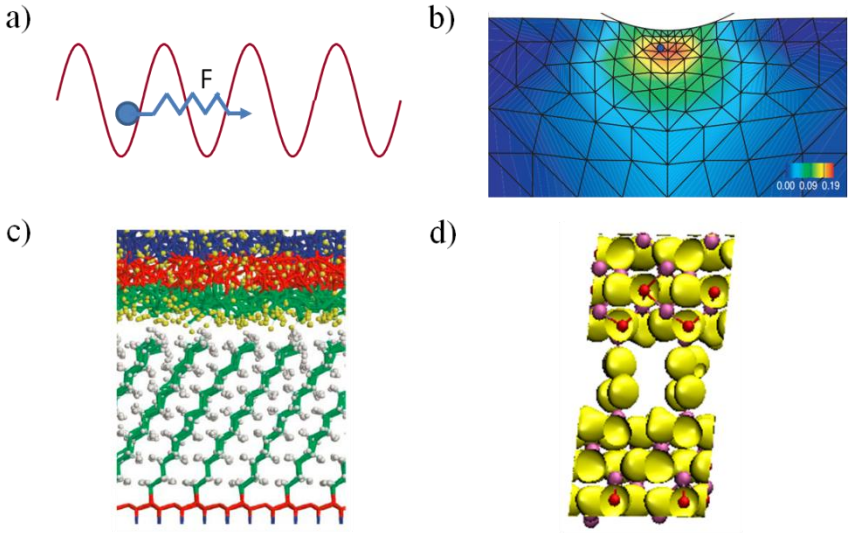

Figure 1.6. Four general categories of theoretical techniques. a) Phenomenological method, in which the motion of a particle with respect to a periodic potential may be calculated. b) Finite element model, where energies and stresses are evaluated at the intersecting points to create a contour plot [27]. c) Force field method, in which particle motion is determined via classical expressions [28]. d) Quantum chemical method, where electron densities dictate the motion of atoms [29].

1.3.1 Phenomenological Models

The least computationally demanding models, and consequently the oldest, are the phenomenological models. The development of these models preceded the existence of computers, and thus significant approximations were made to represent sliding surfaces in a manner that permitted an analytical study of friction using pencil and paper. The key model that arose from this era was the Prandtl-Tomlinson model [30,31], which examines the forces associated with pulling a mass over a sinusoidal potential representing a surface with asperities at regular intervals. It was developed to model plastic behaviour of sliding materials. The potential

energy profile allows for static friction to exist, and the dampened velocity allows for the inclusion of varying temperature effects and kinetic friction, while maintaining a very simple trajectory. A less involved model of surface interactions (Eq. 1.2) involves the extension of Amontons's law (Eq. 1.1) to include the effects of adhesive interactions between surface via a second term that is proportional to the contact area (*A*) [32,33,34]. A more detailed study of this term was published by the Mosey group [35] and is discussed later in Section 1.3.4.

$$F = C_1 A + \mu L \qquad \text{(Eq. 1.2)}$$

1.3.2 Finite Element Models

Upon the development of computers, it became possible to examine more sophisticated models for interacting surfaces. These were typically achieved using finite element simulation techniques, which treated surfaces as a collection of points connecting via various potentials. The data entering the potentials corresponded to experimental properties of the surfaces forming the contact, and thus these methods could be used to gain insight to the interactions between specific types of materials brought into contact with one another. More recently, finite element model (FEM) methods for modeling material deformation and fracture have been developed [36]. This level of modelling is particularly advantageous for engineering applications such as heat transfer, as well as solid and fluid mechanics [37,38]. There are also extensive applications to the biological and medical fields for modelling larger systems such as stresses on bones and tissues [39,40].

1.3.3 Force Fields

Further advances in computers permitted the use of models resolved to the level of individual atoms (or groups of atoms) to study friction. The interactions between the atoms are described with force fields (FF) and the motion of the system is usually achieved in the context

of molecular dynamics (MD), which treats the atoms as classical particles that obey Newton's equations of motion. The equations that underlie MD simulations and force fields are described in Section 2.4.2.

In FF-based MD simulations, the forces acting on the particles are derived from a potential energy expression that accounts for the interactions between the particles in the system. The particles in the system may correspond to individual atoms, so-called united atoms (in which small groups of atoms are lumped together), and bead models (in which larger functional groups such as amino acids are lumped together). The interactions between the particles are described using approximate functional forms containing parameters obtained from experiments or quantum chemical calculations on related systems. These models are useful in permitting studies of systems containing a large number of atoms (tens of thousands of particles) over relatively long timescales (nano- to microseconds). They however, cannot generally examine changes in bonding unless it is specially accommodated for with a reactive force field. FF models have been used to study a wide range of properties related to friction. In particular, these models have been used to simulate friction between surfaces and to better understand the atomic scale behaviour [41,42], as well as load, temperature, and velocity dependences [43]. Large materials, such as those containing polymers, are frequently studied with FF MD [44,45].

Since AFM is a popular tool for studying behaviour at surfaces, it makes sense to simulate such a sharp implement of similar composition to reproduce the trends observed. One simulated AFM study was that of friction on H-terminated diamond surfaces using FF methods [46]. In those simulations, friction along different surface faces and directions was measured with two different tip shapes. These details are illustrated in Figure 1.7. Friction trends, after being normalized, were reproduced for all except for one sliding direction. For the outlying case,

some suggestions for discrepancy were proposed. In a subsequent publication by the same research group [47], similar simulations were performed for a range of temperatures. As the temperature increased, slightly lower shear strengths were observed, as well as pull-off force and work of adhesion, which is consistent with theory.

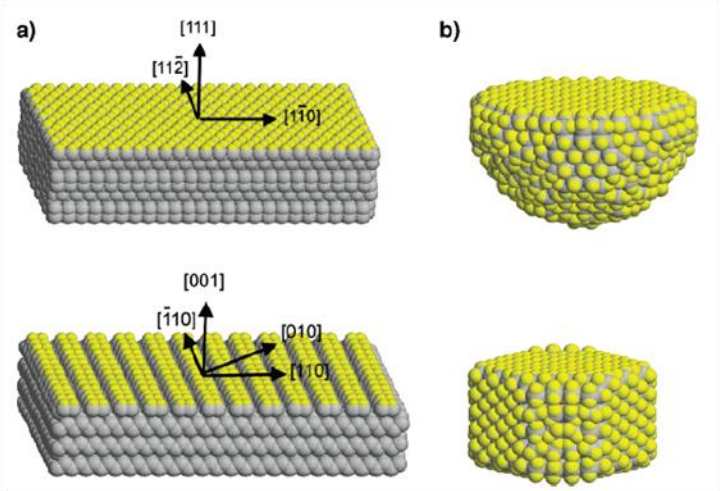

Figure 1.7. Surfaces and tips used. (a) Surfaces tested, including the unique crystallographic sliding directions. (b) The curved and nanowire diamond tips, viewed from the side [46].

Lubricants are frequently introduced between surfaces being sheared to reduce friction forces and inhibit wear. A study of large alkane molecules was simulated with FF MD to observe rheological differences when there are changes in the carbon backbone such as branching [48]. The lubricant was confined between two walls, which moved in opposite directions to simulate the desired type of flow. Molecules with higher levels of branching were found to have weaker layering near the walls. Additionally, they were less affected by the liquid flow because they did not reorient as much as other types of molecules, and were determined to perform better as a lubricant than smaller molecules. Many other simulated lubrication studies exist, including those of oils, diesel, and ionic lubricants [49,50,51].

1.3.4 Quantum Chemistry

In recent years, computers have become sufficiently powerful to permit studies of chemical systems resolved to the level of the electronic structure. These techniques employ quantum chemical (QC) methods to determine the energy of the system and forces acting upon the atoms in the system, by means of a Hamiltonian. QC may be subdivided by a spectrum of levels of theory based on Hamiltonian parameterization, ranging from essentially no parameterization in *ab initio* methods, to semi-empirical and empirical methods, in which parameters are introduced in attempts to reduce computational effort.

So-called static quantum chemical calculations, in which the energy of the system is evaluated with the nuclei fixed at specific positions, effectively involve examining the system at 0 K. By evaluating the energy for structures moved in specific ways, e.g. subjected to specific deformations, quantum chemical methods have permitted the determination of the mechanical strengths of materials and the changes in energy associated with slip processes. These static quantum chemical approaches have been used to examine adhesion and shear strengths of diamond interfaces [52], elastic constants of zinc blende and wurtzite III nitrides [53], and the friction mechanism of fluorographene and graphane [54].

Quantum chemical methods have also been used in conjunction with molecular dynamics methods to provide insight into slip processes under dynamical conditions using model systems that are resolved to the level of the electronic structure. Such simulations are able to capture changes in bonding that can be related to wear, tribochemical reactions and friction forces. However, such methods are limited to examining small systems (a few hundred atoms at most) over short time scales (a few hundred picoseconds at most). The Mosey group has a history of studying tribological and tribochemical processes with QC MD simulations of periodically

repeated sliding functionalized alumina surfaces [29,35,55]. The images in Figure 1.8 and 1.9 are examples of some of the research that has been done.

The structures in Figure 1.8 correspond to illustrated models of bulk alumina and hydroxylated alumina surfaces undergoing slip. QC-based MD simulations of these systems shed light into the effects of adhesive interactions between sliding surfaces [35]. In the case of bulk alumina (Figure 1.8a), the slip processes involved brittle fracture of the material as it moved along the slip direction. The associated static friction force was large, and could be attributed to the strengths of the bonds across the interface on which slip occurred. The hydroxylated interfaces (Figures 1.8b and c) exhibited different compositions dependent on the normal load. At low normal loads (Figure 1.8b), the hydroxyl groups on the two surfaces forming the interface interacted with each other via hydrogen bonds. Slip involved the dissociation of the weak bonds, leading to relatively low friction forces. At higher loads (Figure 1.8c), proton transfer occurred across the interface, transforming the hydroxyl groups into water molecules. During slip, the oxygen atoms in water molecules bonded to one side of the interface form Al-O bonds with aluminum ions on the other side of the interface. These bonds had to break for slip to occur, which led to large friction forces. The ability to model the bond formation and dissociation processes associated with slip by using QC-based MD led to the development of a physically-based model of the form given in Eq. 1.2, which describes the effects of adhesive interactions between surfaces on friction forces.

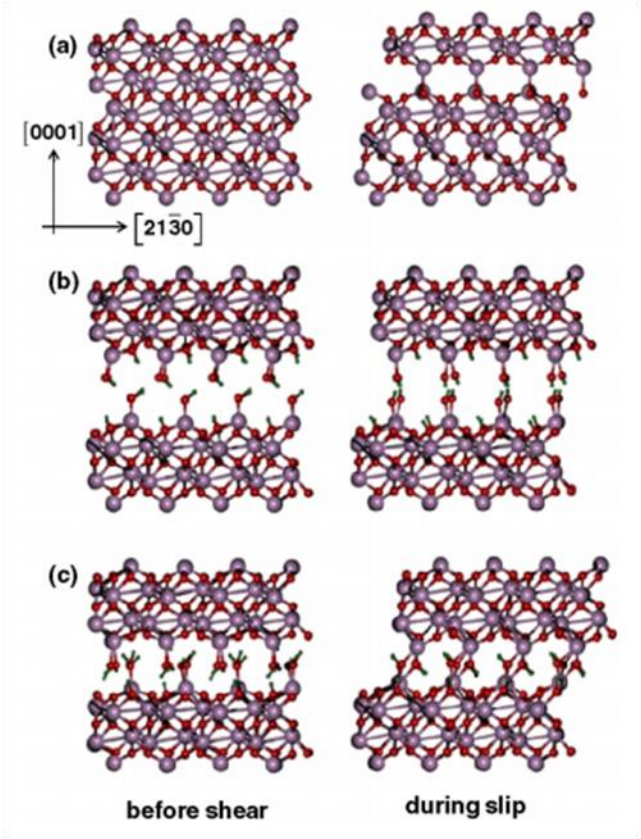

Figure 1.8. Bulk and water-functionalized alumina surfaces, before and during slip due to shear strain [35]. Shown are slip mechanisms for (a) bulk and (b, c) water-functionalized alumina, with 0, 0 and 8 nN of normal load respectively. The simulation cell is repeated by two in the direction of shear.

QC-based MD simulations have also been used to examine the reactions that occur between molecules representing different chemical functional groups under the conditions experienced within sliding contacts. In one study, acetaldehyde-functionalized alumina surfaces (Figure 1.9) were sheared at various normal loads to induce reactions between the aldehyde components and the associated sheared strengths were determined. The results showed that the aldehydes polymerized under high loads, which led to a range of slip mechanisms. The presence of the polymers was found to be advantageous with respect to wear for slip mechanisms that did not involve bond rupture. Meanwhile, in cases that did involve bond rupture, the simulations suggested that the friction forces required to initiate motion of the surfaces may be reduced as the polymer length increased. Overall, the results of that study suggested that it may be possible to

use reactions occurring within sliding contacts to achieve lubrication and indicate that larger lubricant molecules may be more effective at lowering levels of friction.

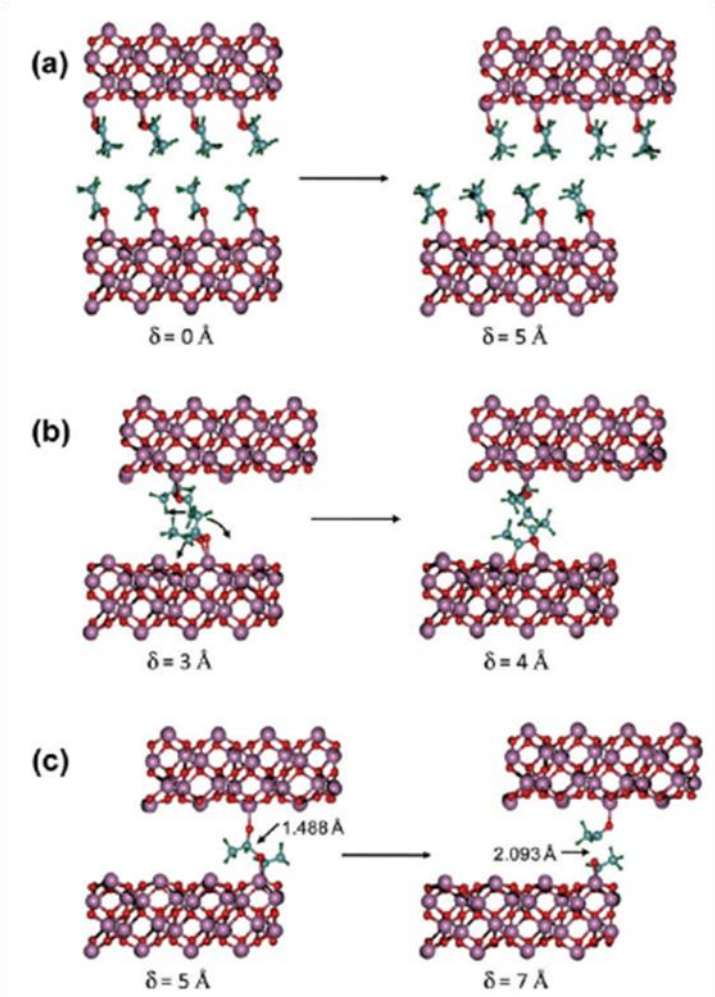

Figure 1.9. Aldehyde-functionalized alumina surfaces under shear strain [55]. Normal pressures of (a) 0.0 GPa, (b) 7.5 GPa, and (c) 10.0 GPa have been applied to the cells. The reactive slip events shown are emphasized, with the unreacted groups removed for parts b and c. The simulation cell is repeated by two in the direction of shear.

Despite the ability to model chemical reactions, the computational demands of QC-based MD simulations impose limitations that may inhibit a direct comparison of the results of those simulations with real-world systems. For example, the QC-based MD studies mentioned above employed models containing between 100 and 200 atoms, were performed over timescales

corresponding to tens of picoseconds, and employed sliding rates of 100 m/s. Meanwhile, real-world systems are much larger, and sliding occurs over longer time scales at lower velocities.

1.4 Scope and Goals

The project reported in this thesis was undertaken in collaboration with the Xerox Research Centre of Canada (XRCC). The research focuses on examining behaviour related to friction, wear and lubrication of components in laser printers. A schematic of a laser printer is shown in Figure 1.10. In short, a photoconducting drum (2 in the figure) transfers toner to the paper to be fused, while any excess toner is removed by a cleaning blade (11 in the figure). This cleaning blade has a short life expectancy, as it experiences high levels of friction and wear. A significant number of patents have been published by XRCC with the aim of prolonging the functional life of the cleaning blade via alterations in the blade shape or means of contact [56] as well as the addition of lubricant to the surface of the photoconducting drum just ahead of the cleaning blade [57]. In the close up shown in Figure 1.11, one can see the way that the cleaning blade is placed in order to remove excess toner from the photoconducting drum. A more in-detail look at the composition of these components is available in Section 2.1.

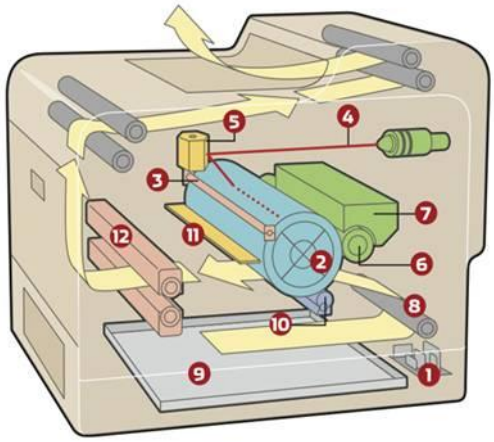

Figure 1.10. A schematic of a laser printer [58]. The components of interest are (2) the photoconducting drum, and (11) the cleaning blade.

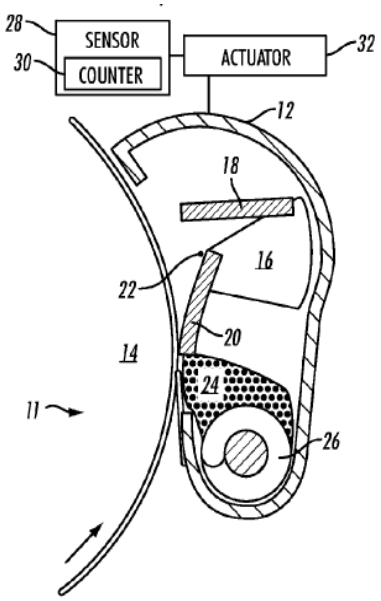

Figure 1.11. An illustration of the cleaning mechanism [59]. The photoreceptor or photoconducting drum **14** rotates counter clockwise, while the cleaning blade **20** wipes off the excess toner **24**.

The objective of this thesis is to gain a better understanding of the conditions, slip mechanisms, and lubrication possibilities at the point of contact between the cleaning blade and the commercial photoconducting drum coated in toner and/or lubricant. As discussed above, MD simulations are useful for studying friction, wear and lubrication at the atomic level. As such, FF-based MD simulations were performed on a variety of model systems representing interfaces containing the materials present at the point of contact between the cleaning blade and the photoconducting drum. Specifically, interfaces were formed between representative models of polyurethane (representing the cleaning blade) and polycarbonate (representing a commercial drum) with and without a simple alkane lubricant. The simulations examined slip along these interfaces and yielded a range of quantities related to structural details and shear stresses that can be used to determine the friction forces, coefficients and slip mechanisms. The results demonstrate that the slip mechanism involves a rapid alignment of the polymers in the region of the slip interface(s) along the slip direction. The friction forces are found to depend on the

weaker material in the system, and the ability of the lubricant to lower friction is found to depend on the amount of lubricant in the system.

The content of the rest of the report is organized as follows. The materials and methods are outlined in Chapter 2, which includes detailed descriptions of the systems and how the simulations were performed, as well as how the data was analyzed. The results are presented in Chapter 3 with summarized plots of the data collected for each different category of model (i.e. bulk, dry interfacial, singly lubricated interfacial, and doubly lubricated interfacial). Following the results, Chapters 4 and 5 include the discussion and conclusion of the results, respectively.

Chapter 2: Materials & Methods

This project aims to use molecular dynamics (MD) simulations to study the friction and wear properties of materials associated with the contact between laser printer components corresponding to a commercial photoconducting drum composed of a polycarbonate material and an elastomeric cleaning blade composed of diphenylmethylene diisocyanate and polytetramethylene ether glycol. Lubrication of the drum with octadecane is proposed as means to improve sliding between these two surfaces; a route to improve printer performance. The materials used to construct the model systems examined in the simulations are discussed in Section 2.1, and the construction of these models is discussed in Section 2.2. The manner in which the MD simulations were performed is described in Section 2.3 and the potential energy functions used in these simulations are outlined in Section 2.4. All calculations reported in this work were performed with the Large-scale Atomic/Molecular Massively Parallel Simulator (LAMMPS) simulation package [60], while the construction of model systems and analysis of results relied on codes written in-house.

2.1 Materials

The commercial photoconducting drum of interest is composed of a polycarbonate (PC) material with an arylamine transport hole, though the PC provides the mechanical robustness. In the absence of specific details regarding the chemical structure and composition of the drum, the simulations were performed using bisphenol-A polycarbonate (BPA-PC). This material has been thoroughly studied [61], which makes it an excellent basis for our model systems because data are available to compare against during parameterization and results analysis. The specific model of BPA-PC considered in this work consisted of 20 repeated BPA units, and is shown in Figure 2.1a.

The elastomer used in the cleaning blade is described in a patent by the Xerox Corporation [62]. This elastomer was modeled using polymers composed of a combination of diphenylmethylene diisocyanate and polytetramethylene ether glycol. The selected structure of each polyurethane (PU) molecule is such that there are 5 ether segments interspersed with single diisocyanates. Each ether segment contains 40 repeated tetramethylene glycol units. The final molecular structure is shown in Figure 2.1b.

Lubricants are used to inhibit wear of the drum/blade contact [63]. The lubricant was modeled by a thin layer of representative straight-chained alkane molecules, octadecane (C18). The structure of the lubricant molecules is shown in Figure 2.1c.

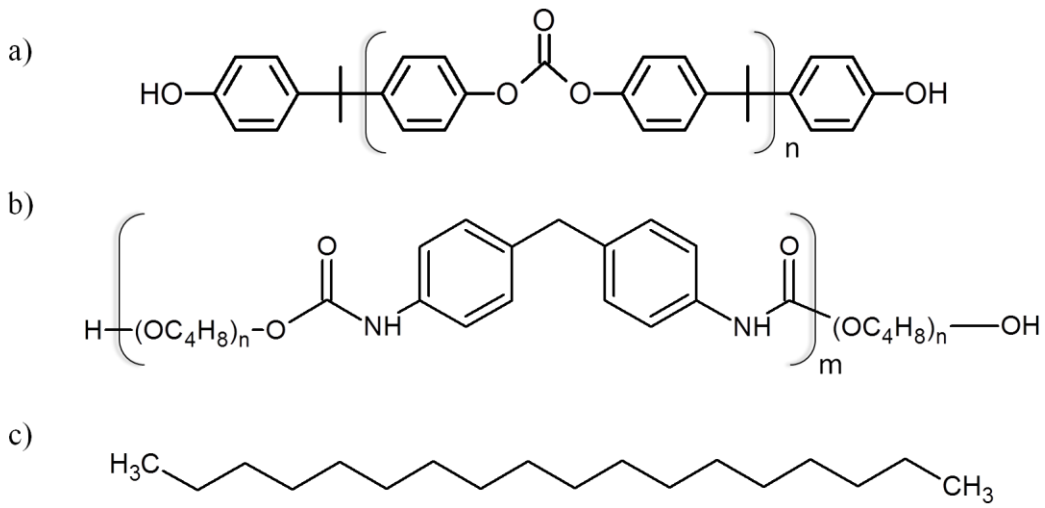

Figure 2.1. Molecular structures used for the modeling of the three materials. (a) BPA-PC repeats the denoted section with n = 19 for a total of 20 units, (b) PU repeats the denoted sections n = 40 and m = 4 times, and (c) the C18 lubricant is as shown.

2.2 Construction of Simulation Cells

In order to model friction and wear, it is necessary to deform the system in a manner consistent with sliding, shearing and/or compression. To do this, the system is placed in a simulation cell treated with periodic boundary conditions. The simulation cell can then be deformed in a controlled manner via strain or external stresses to obtain the desired mechanical properties. The different models considered in these simulations correspond to bulk

representations of the polymers, models in which slabs of the materials were placed on top of each other to model sliding in the presence of an interface, and models in which slabs of the materials were separated by the lubricant. The construction of the bulk systems is described in Section 2.2.1, whereas the construction of systems containing dry and lubricated interfaces are described in Sections 2.2.2 and 2.2.3, respectively. Perl scripts were written and used to automate all steps involved in the construction of these systems.

2.2.1 Bulk Systems

Systems were constructed to perform simulations on the bulk PC, PU, and C18 materials. As noted above, the PC system consisted of polymers containing 20 BPA repeat units, whereas the PU system consisted of five ether segments that were each separated by one diisocyanate unit. The ether segments consisted of 40 tetramethyl glycol units. The following approach was taken to construct the polymers. The basic repeat unit was constructed using the Gaussview software package [64] and the coordinates of that unit were saved. This structure was then repeated to yield a polymer of the desired length with proper end units. Once a polymer of the desired material was formed, it was placed in the simulation cell at a randomly selected position with a randomly selected orientation. This process was repeated until the desired number of polymers was placed in the simulation cell, being 20 for PC, 5 for PU, and 20 for C18.

The process above yields an amorphous structure, which is expected for the materials considered in this work, but the randomized construction process does not likely yield a structure with a low energy. To yield lower energy structures, which are more likely to represent the actual material, the geometries were first optimized and then equilibrated at a temperature of 300 K through two sets of MD simulations, which are illustrated qualitatively in Figure 2.2. The first MD simulation involved linearly compressing the simulation cell dimensions to just beyond the

point at which the bulk system reached the density of the reference material. Once compression was complete, an MD simulation was performed in which the dimensions of the orthogonal simulation cell were allowed to change to maintain an external pressure of 0.0 GPa. The system was equilibrated in this simulation until the volume of the system stabilized.

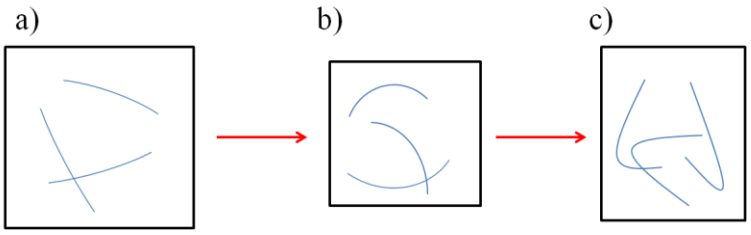

Figure 2.2. A schematic of the equilibration process. Part (a) is the initial optimized structure. Part (b) is the linear compression of all cell dimensions, at 300 K. Part (c) is an NPT equilibration with 0.0 GPa of external pressure and at 300 K. Throughout the equilibration process, the large molecules evolve from their initial set geometries to lower energy conformations.

2.2.2 Dry Interfacial Systems

Layered models representing PC/PC, PC/PU and PU/PU interfaces were also constructed in this work. These models allow one to determine the mechanical properties associated with the motion of one material relative to another when an interface exists between the materials. These layered models were generated by constructing separate slab models for each material that extended in the *x*-*y* plane. The slabs for each material forming the interface were then brought together in a single simulation cell to form the layered system.

The specific steps involved in the formation of the slabs and layered structures were as follows. First, a slab was constructed by taking the bulk amorphous cells that were constructed as described in Section 2.2.1 with the periodic boundary conditions along the *z* direction removed. This yields a material that extends infinitely in the *x*-*y* plane via periodic boundary conditions, but has a finite thickness along the *z* direction. The interfacial structures were then formed by layering these systems together, separated by an appropriate amount of vacuum space along the *z* direction (~10 Å in all cases) to ensure the layers did not overlap, and reintroducing periodic

boundary conditions along *z*. In the case of a single material (PC/PC or PU/PU), this process simply involved reintroducing periodic boundary conditions along the *z* direction for a cell formed by a single replication of the initial bulk simulation cell along the *z* direction. For cases where two different slabs formed the interface (PC/PU), each slab was incorporated into a single simulation cell with dimensions in the *x*-*y* plane that were adjusted to ensure the lateral dimensions of both slabs were adequately accommodated. The layered structures were then equilibrated in a similar fashion to the bulk material. The structures, i.e. the simulation cell and atomic positions, were initially optimized and equilibrated in MD simulations with a fixed cell. A subsequent MD simulation was performed in which the *x* and *y* dimensions were fixed while the cell was compressed along the *z* direction to an external pressure of 100,000 atm (~ 10 GPa). The system was then allowed to equilibrate with varying amounts of normal pressure to prepare models for friction force and coefficient measurements.

2.2.3 Lubricated Interfacial Systems

The lubricated systems consisted of models in which C18 molecules were introduced between slabs of PC and/or PU. These lubricated systems were constructed by separating the layers in the appropriate dry interfacial system formed as described in Section 2.2.2 and introducing the C18 molecules into additional space between these layers. The first step in this process consisted of constructing and equilibrating a C18 slab system of a sufficient size to ensure there would be roughly two or four molecular layers of the C18 lubricant. An amount of two molecular layers of lubricant was based on advice of XRCC. This layer of lubricant was achieved by placing the desired number of C18 molecules, ranging from 50 to 100 for every two molecular layers, randomly into a simulation cell with lateral dimensions that were the same as those of the dry interfacial systems into which the lubricant would be incorporated. The

equilibrated slabs from the appropriate dry interfacial system were then separated by an amount equalling the thickness of the equilibrated C18 system with ample vacuum space (~10 Å) on each side, and the lubricant was introduced into the resulting space. The entire system was then equilibrated via the equilibration approach described above in Section 2.2.1.

2.3 Evaluation of mechanical properties

It was of interest in this project to evaluate compressive and shear strengths. This is achieved by deforming the cell in specific ways. The compressive strengths of the materials were obtained by subjecting the system to a linearly increasing compressive stress along the *z* direction and obtaining the resulting strain-time relationship. It is not feasible to shear the systems at an experimentally accessible rate. Instead, the stress rate that was selected was chosen such that the simulations could be completed in a reasonable amount of computational time. Experiments typically achieve strain rates on the order of 10^2 s^{-1}, with specially designed instruments [65] for 10^4 s^{-1}, while the simulations are sheared at strain rates on the order of 10^9 s^{-1}. It is possible that at such extreme rates, the mechanism by which the material yields or fails may be affected.

The compressive stress rate used in the bulk PC and bulk PU simulations was 1.62 GPa/ns. Generic representations of this process and a sample strain-time plot are shown in Figure 2.3. The compressive strength is taken as the external stress at which the first significant shift in the strain-time plot occurs. This break in the plot occurs because the system undergoes an irreversible change in structure due to the applied stress, $\sigma_{zz,}$ at that point which equals the compressive strength.

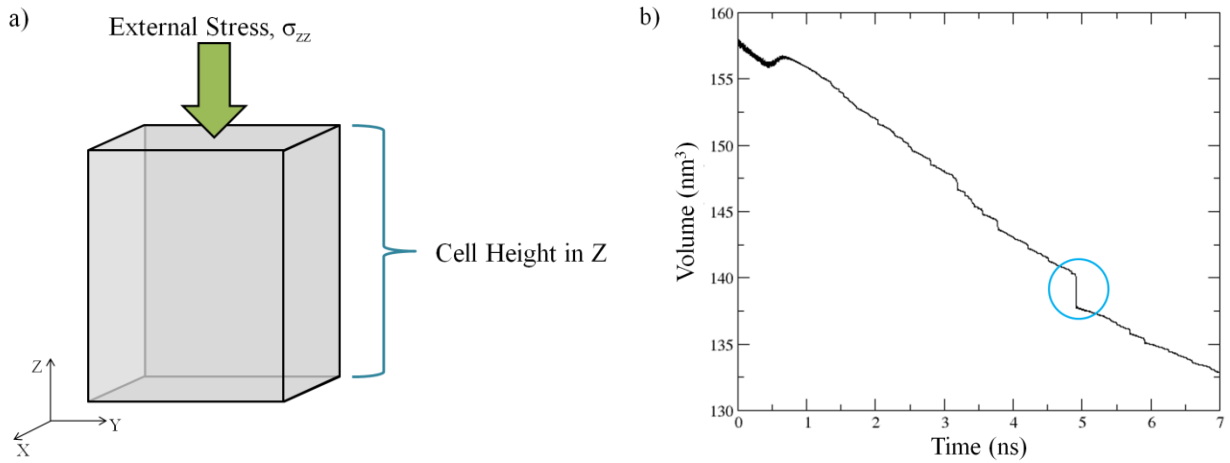

Figure 2.3. A schematic of the compression process and data obtained from compression. (a) The compression process involves subjecting the cell to an external load, σ_{zz}, which is increased at a rate of 1.62 GPa/ns. (b) A plot of cell volume as a function of compression time. Applying the increasing compressive stress leads to a reduction in cell height, and a corresponding reduction in cell volume. The circled break in the plot corresponds to the point at which the system yields to the compressive stress. The applied stress at this yield point corresponds to the compressive strength of the material.

The systems were sheared by deforming the simulation cell in such a way that either the *x* or *y* components of the **c** lattice vector were changed by linearly increasing the external stress applied to the components of the simulation cell and allowing the cell to respond. For all systems except for bulk PC and bulk PU, the stress was increased at a rate of 1.62 GPa/ns. While shear was occurring, the *z* component of the **c** lattice vector was allowed to vary to maintain a constant normal load. Generic representations of this procedure and the resulting internal stress-time relationships are shown in Figure 2.4. The plot shows that during shear, the internal stress acting along the shear direction increases linearly at a rate matching the rate at which the applied stress increases along that direction. A peak in the stress-time is reached, followed by a sharp drop in the internal stress. This is associated with the slip event and the external stress applied to the system at that point corresponds to shear strength, τ_c. Given the fact that the external and internal stresses are in equilibrium up to the point at which slip occurs, it is also possible to associate the internal stress at the point of slip with the shear strength of the system. The procedure described

above allows the shear strengths to be obtained while the system is subject to different normal loads, σ_{zz}, acting normal to the slip direction. The slope of a plot of τ_c versus σ_{zz} yields the friction coefficient. Since these amorphous systems have no obviously preferred slip directions, in some cases separate simulations were performed in which shear was achieved by varying either the *x* or *y* component of **c** in positive and negative directions. This yields up to four separate values of the shear strength for each model system at each normal load.

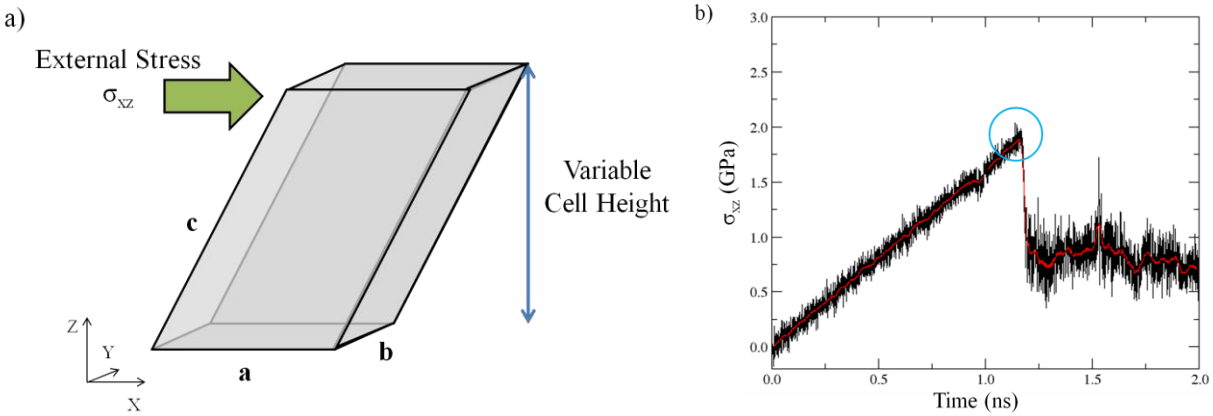

Figure 2.4. A schematic of the shear procedure and data obtained during shear. (a) The deformation of the simulation cell along the *x* direction by applying a shear stress, σ_{xz}, that increases linearly with time. The height of the simulation cell is allowed to vary to maintain a constant normal load, σ_{zz}, during the simulation. (b) The internal shear stress along *x* as a function of shear time. The maximum in the plot is associated with the slip event and corresponds to the shear strength of the material.

Since there is an apparent limitation in the software used for the number of steps a simulation can accumulate, it was not reasonable for the shear strengths of the bulk PC and bulk PU systems to be reached by linearly increasing the external shear stress. The shear strengths of these bulk materials were instead evaluated by increasing the *x* component of the **c** vector at a constant rate. The tilt factor of the simulation cell is measured as a fraction of the distance the top of the cell is displaced (the *x* component of the **c** vector) over the height of the cell (the *z* component of the **c** vector). It was increased at a constant strain rate of 1.0 ns^{-1}, which has a comparable stress rate to the stress-controlled shearing simulations at the onset of shear, but reaches greater stress rates as the system continues to shear.

In all dynamics simulation steps, a temperature of 300 K was imposed on the system. Since any work done on the system should result in large temperature fluctuations, the temperature was controlled by a thermostat in order to mimic the effect of the bulk material's ability to draw heat from high temperature locations and redistribute it throughout the rest of the material.

2.4 Molecular Dynamics

2.4.1 General details

As noted above, molecular dynamics (MD) simulations were used in this study. These simulations aim to model the atomic level behaviour of the system by treating the atoms in a system as particles that move according to Newton's equations of motion. On the molecular scale, MD simulation is used as a tool for examining how a system evolves over time. Various conditions may be controlled simultaneously to simulate experimental or ideal conditions. An extensive list of features may be extracted from the simulations, including the data required to calculate the key material properties and slip mechanisms studied here. The movement of the particles within the defined environment is governed by particular equations of motion which are discussed in Section 2.4.2. Much of the validity of properties or events obtained through simulations is directly dependent on the appropriate selection of parameters and techniques required, which are discussed in Sections 2.4.3 and 2.4.4. The specific software package that was used is called "Large-scale Atomic/Molecular Massively Parallel Simulator" (LAMMPS) [60].

2.4.2 Integrating trajectories

The standard velocity-Verlet trajectory integrator in LAMMPS was used for all simulations. In this method, both the particle positions and velocities are updated for each time step. Equations for this motion are given below, Eqs. 2.1 and 2.2.

$$\boldsymbol{r}(t + \Delta t) = r(t) + \boldsymbol{v}(t)\Delta t + \frac{1}{2}\boldsymbol{a}(t)\Delta t^2 \quad \text{(Eq. 2.1)}$$

$$\boldsymbol{v}(t + \Delta t) = \boldsymbol{v}(t) + \frac{1}{2}\big(\boldsymbol{a}(t) + \boldsymbol{a}(t + \Delta t)\big)\Delta t \quad \text{(Eq. 2.2)}$$

where ***r***, ***v***, and ***a*** indicate the positions, velocities and accelerations of the particles at a given point in time.

The atomic accelerations are obtained by first obtaining the forces acting on the atom by differentiation of the potential energy, *U*, of the system with respect to the atomic positions, i.e. $\mathbf{F}_i = -\nabla_i U$. The forces are then converted into accelerations via Newton's second law of motion, i.e. $\mathbf{a}_i = \mathbf{F}_i/m_i$. The potential energy function from which the atomic forces are derived is described below. Once the accelerations are evaluated, they are used in conjunction with the current atomic velocities to advance the atomic positions from their current values, $\boldsymbol{r}(t)$, to their values at a slightly later point in time, $\boldsymbol{r}(t+\Delta t)$ according to Eq. 2.1. The velocities are also updated over time using information regarding the atomic accelerations according to Eq. 2.2. In this manner, Eqs. 2.1 and 2.2 sequentially update the positions and velocities of the particles over time, thereby generating trajectories corresponding to the atomic-level motions of the systems under study.

2.4.3 Controlling temperature and pressure

It is necessary to control the temperature and pressure of the system to model its behaviour under a given set of thermodynamic conditions. In the present study, this was achieved by using the combined thermostat and barostat developed by Martyna and coworkers [66]. The thermostat is based on the conventional Nose-Hoover thermostat, which uses an extended Hamiltonian to mimic a system immersed in a heat bath with which it can exchange energy to maintain a target temperature. The barostat functions in a similar manner by allowing the cell to

deform in a manner analogous to performing work against a piston to maintain a desired pressure. The equations of motion associated with this thermostat/barostat combination are:

$$\dot{\boldsymbol{r}}_{\boldsymbol{i}} = \frac{\boldsymbol{p_i}}{m_i} + \frac{p_\epsilon}{W}\boldsymbol{r_i} \quad \text{(Eq. 2.3)}$$

$$\dot{\boldsymbol{p}}_{\boldsymbol{i}} = \boldsymbol{F_i} - \left(1 + \frac{1}{N}\right)\frac{p_\epsilon}{W}\boldsymbol{p_i} - \frac{p_\xi}{Q}\boldsymbol{p_i} \quad \text{(Eq. 2.4)}$$

$$\dot{V} = \frac{3Vp_\epsilon}{W} \quad \text{(Eq. 2.5)}$$

$$\dot{p_\epsilon} = 3V(P_{int} - P_{ext}) + \frac{1}{N}\sum_{i=1}^{N}\frac{\boldsymbol{p_i^2}}{m_i} - \frac{p_\xi}{Q}p_\epsilon \quad \text{(Eq. 2.6)}$$

$$\dot{\xi} = \frac{p_\xi}{Q} \quad \text{(Eq. 2.7)}$$

$$\dot{p_\xi} = \sum_{i=1}^{N}\frac{\boldsymbol{p_i^2}}{m_i} + \frac{p_\epsilon^2}{W} - (3N+1)k_BT \quad \text{(Eq. 2.8)}$$

$$Q = 3Nk_BT/\omega_T^2 \quad \text{(Eq. 2.9)}$$

$$W = (3N+3)k_BT/\omega_P^2 \quad \text{(Eq. 2.10)}$$

These equations affect the rates of change in six variables: position, $\mathbf{r_i}$, (Eq. 2.3), particle momentum, $\mathbf{p_i}$, (Eq. 2.4), volume, *V*, (Eq. 2.5), barostat momentum, p_ϵ, (Eq. 2.6), thermostat position, ξ, (Eq. 2.7), and thermostat momentum, p_ξ, (Eq. 2.8). The total force acting on each particle is $\mathbf{F_i}$. We have assumed a 3-dimentional system with no constraints, so *N* represents the number of particles. Each particle has a mass of m_i, while the thermostat and barostat are given masses of *Q* and *W*, respectively. In the case of a constant volume simulation, i.e. (NVT) conditions, the barostat momentum and rate of volume change are both zero, and therefore so are Eqs. 2.5 and 2.6. This causes a number of terms from the other NPT equations (2.3 through 2.10) to also equate to zero. The values chosen for ω_T and ω_P represent the frequency at which the respective thermostats fluctuate.

2.4.4 Simulation parameters

The use of Eqs. 2.1 through 2.10 requires the selection of various parameters. In particular, it is necessary to define a time step for the simulations, Δt, as well as the masses of the thermostat and barostat. In LAMMPS, the latter are defined using parameters T_{damp} and P_{damp}, which are directly related to ω_T and ω_P.

The time step is a critical parameter to choose in the simulation. If the time step is chosen to be too long, the integration of Newton's equations will be poor and the resulting trajectories will be meaningless. The choice of a time step that is too long is often evident by a large drift in the total energy of the system, which should be conserved in Newtonian dynamics. Meanwhile, the use of a very small time step will require a large number of MD steps, each with their own force evaluation to be performed, which will slow down the simulation. Thus one aims to choose the largest value of Δt that conserves the total energy of the system to an acceptable level.

The value of Δt used in this work was selected by examining conservation of total energy under constant (NVE) conditions using a system of polyethylene molecules with Δt = 0.5, 1.0 and 2.0 fs. The total energies during 1 ns simulations performed with these values of Δt are shown in Figure 2.5. A time step of 0.5 fs was ultimately selected, as less than 0.5 kcal/mol was lost by the end of the 1 ns run. It is noted that this corresponds to a drift in total energy of 0.5 kcal/mol distributed over the thousands of atoms in a typical simulation cell. This amount of energy is negligible compared to the amount of energy introduced to shear the systems to the point at which slip occurs. A time step of 0.5 fs conserved the total Hamiltonian used in the simulations performed under NPT conditions to the same level as that seen for the simulations performed under NVE conditions.

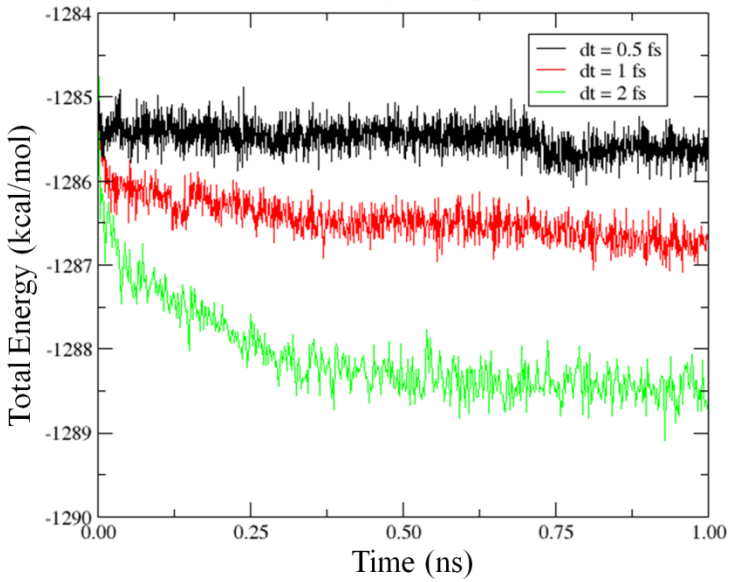

Figure 2.5. A test for conservation of energy with different time step sizes, using the NVE ensemble.

The thermostats and barostats implemented in LAMMPS require that a damping parameter be provided for each of the controls, labeled T_{damp} and P_{damp}, respectively. These values have units of time (fs in this case) which is an approximate determination of how long it should take for the temperature or pressure to relax. A set of values around the magnitude of those recommended by the documentation were selected to test for both parameters. The resulting plots of temperature and pressure as functions of time are presented in Figures 2.6 and 2.7, respectively. It is evident in Figure 2.6 that larger values of T_{damp} result in a more delayed response to changing temperature, which was an immediate jump to 300 K. Similarly in Figure 2.7, larger values of P_{damp} result in larger oscillations about the external pressure of 0.0 GPa in this case. From this data, values of 50.0 fs and 500.0 fs were chosen for T_{damp} and P_{damp}, respectively.

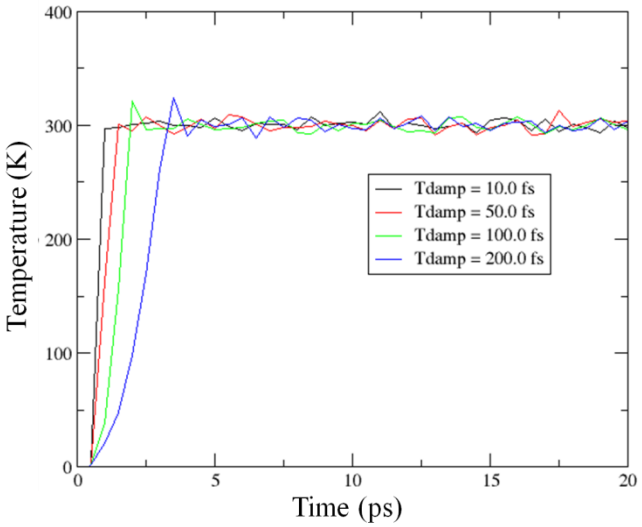

Figure 2.6. A test for relaxation of temperature with different damping parameter values, using the NVT ensemble. Only a sample from the early portion of the simulation is shown to see the difference in the plots.

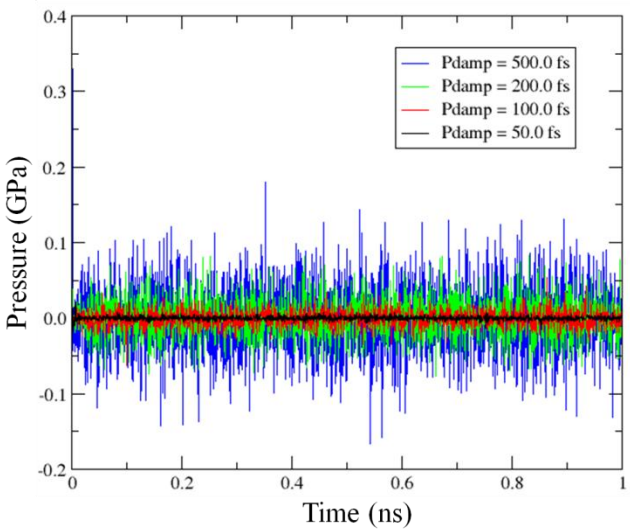

Figure 2.7. A test for relaxation of pressure with different damping parameter values, using the NPT ensemble.

2.5 Dreiding FF

2.5.1 Selection

As noted above, the forces acting on the atoms are obtained by differentiating the potential energy of the system with respect to the nuclear positions. The present work obtained the potential using the Dreiding force field [67]. This force field provides a set of generic parameters that can be used to study materials composed of main group elements in a variety of

chemical states, e.g. different states of hybridization. The use of such a generic force field simplifies the study of different types of materials, but the lack of specificity with respect to the parameters may compromise accuracy. However, the use of a more specific force field would require us to devote a substantial amount of time to the parameterization. Since the present study aims to evaluate trends in values (shear strength as a function of load) for a common series of materials and obtain qualitative interpretations, it was decided to sacrifice the potential quantitative accuracy that could be obtained by using a more specific force field to permit the available time to be applied to studying the various systems of interest with the generic Dreiding force field. Perl scripts were written and used to automate all steps involved in the assignment of the Dreiding parameters.

2.5.2 Potential Energy Contributions

In the Dreiding force field, each atom is defined by a label which is unique based on the hybridization of the atom, and which is associated with other equilibrium values, such as bond radius and bond angle. Any interactions defined by combinations of atoms have the potential to be unique based on these atomic labels. The total potential energy, *U*, is the sum of all of the energy contributions that follow, being bond stretches, angle bends, torsions, and non-bonded interactions. The total expression is given in Eq. 2.11.

$$U = \sum_{bonds} E_{IJ} + \sum_{angles} E_{IJK} + \sum_{dihedrals} E_{IJKL} + \sum_{impropers} E_{IJKL} + \sum_{pairs} E_{vdw} + \sum_{pairs} E_{Coulomb} \quad \text{(Eq. 2.11)}$$

All bonding interactions of length *R*, are described by the harmonic potential in Eq. 2.12a.

$$E_{IJ} = \frac{1}{2} K_{IJ}(R - R_0)^2 \quad \text{(Eq. 2.12a)}$$

$$K_{IJ} = n \times 700 \ \ kcal/mol\text{Å}^2 \quad \text{(Eq. 2.12b)}$$

$$R_{IJ}^0 = R_I^0 + R_J^0 - \delta \quad \text{(Eq. 2.12c)}$$

The force constant, K_{IJ}, only varies with the bond order n and does not depend on the atom types (I and J). Equilibrium bond lengths, R_0, are the sum of individual bond radii, altered by a value of $\delta = 0.01$ Å, as shown in Eq. 2.12c.

The potential for angle bending is also chosen to be harmonic, as shown in Eq. 2.13a.

$$E_{IJK} = \frac{1}{2} K_{IJK} \left[\theta_{IJK} - \theta_J^0\right]^2 \quad \text{(Eq. 2.13a)}$$

$$K_{IJK} = 100 \ kcal/mol \cdot rad^2 \quad \text{(Eq. 2.13b)}$$

The angle, θ_{IJK}, is defined by three connected atoms of types I, J and K. The force constant, K_{IJK}, is the same for all types of bonds, and the equilibrium angle, θ^0, only depends on the unique bond angle value for centre atom of type J.

Dihedral angles are defined by four atoms (types I, J, K and L) bonded sequentially in a row. The dihedral angle these four atoms create is defined to be the angle between the two planes defined by atoms IJK and JKL. The potential for dihedral angle φ is shown in Eq. 2.14.

$$E_{IJKL} = \frac{1}{2} V_{JK} \left\{1 - \cos\left[n_{JK}\left(\varphi - \varphi_{JK}^0\right)\right]\right\} \quad \text{(Eq. 2.14)}$$

All three constants only depend on the centre two atoms J and K. The constant, V_{JK}, only depends on the hybridization of J and K, and ranges in value from 0.0 to 45 kcal/mol. The periodicity, n_{JK}, is related to the symmetry of the torsion. The equilibrium dihedral angle is φ^0_{JK}, such that the potential is always equal to or greater than zero.

For an atom of type I, bonded to three other atoms of type J, K and L, the improper torsion angle, Ψ, is defined to be the angle between the plane formed by atoms I, J and K, and the bond between atoms I and L. The inversion potential is shown in Eq. 2.15.

$$E_{IJKL} = \frac{1}{2} \frac{K_I}{\sin^2 \Psi_I^0} (\cos \Psi - \cos \Psi_I^0)^2 \quad \text{(Eq. 2.15)}$$

The equilibrium improper torsion is related to the hybridization of the centre atom I, such that planar sites are given a value of $\Psi^0 = 0°$, and non-planar sites $\Psi^0 = 54.74°$. The force constant,

K_I, is almost always 40 kcal/mol·rad^2, except when centre atoms are in the nitrogen column, in which case the force constant is zero.

Non-bonded interactions are also considered in this force field, which include van der Waals (Eq. 2.16) and Coulomb potentials (Eq. 2.17).

$$E_{vdw} = D_0 \left[\left(\frac{R_0}{R_{IJ}} \right)^{12} - \left(\frac{R_0}{R_{IJ}} \right)^{6} \right], \quad R_{IJ} < R_c \qquad \text{(Eq. 2.16)}$$

$$E_{Coulomb} = \frac{C Q_I Q_J}{\epsilon R_{IJ}}, \quad R_{IJ} < R_c \qquad \text{(Eq. 2.17)}$$

For both non-bonded equations, R_{IJ} is the distance separating atoms I and J. The R_0 and D_0 terms are the van der Waals bond lengths which are unique for each atom type, and are mixed geometrically based on atomic values. ϵ is the dielectric constant, which is typically set to 1. Q_I and Q_J are the atomic partial charges, and the factor of C exists as a conversion to appropriate units. The respective R_c values are radial cutoffs, which exclude interactions beyond the designated points in an effort to reduce computational cost. Both of these non-bonded interactions are excluded for pairs of atoms that are connected via one or two bonds.

Atomic charges are required to obtain Coulomb interactions, but are not as generic as the other required parameters in the Dreiding force field. Not only can charges vary greatly depending on the bonding environment, they can also fluctuate as the subtle chemical environment adjusts throughout the simulations. In order to obtain atomic charges, CHELPG calculations [68] were performed on small model representations of the polymers optimized using HF/6-31G(d,p). In the case of the C18 material, Mulliken atomic charges [69,70] were more reasonable to use than CHELPG. Charges of atoms in equivalent bonding environments were averaged, and as the full polymer was built, any charge accumulation was uniformly

removed from the molecule. The atomic charges were then scaled, within reason, to best reproduce experimental densities of reference materials.

2.6 Densities

Final volumes were taken from the equilibrated charge type and scaling tests. The best charges and types were selected, and the final density comparisons are tabulated in Table 2.1.

Table 2.1. Comparison of Simulated and Experimental Densities

Simulated Material	*Density (g/cc)*	*Experimental Material*	*Density (g/cc)* [71]
PC	1.15	Bisphenol-a polycarbonate	1.20
PU	0.72	Polytetramethylene ether glycol	0.98
C18	0.58	Octadecane	0.78

The data in Table 2.1 show that the density of PC accurately reproduces that of the reference system. In this case, the polymers comprising the simulated and reference systems are of identical composition. This indicates that Dreiding force-field can reproduce the material's properties to a reasonable degree of accuracy.

The data for PU indicate a large difference between the densities of the simulated and reference materials. This difference can be attributed to differences in the structures and compositions of these systems. The simulated material corresponds to a cell containing the polymers shown in Figure 2.1b. Meanwhile, the reference material consists of very long polymers composed of polytetramethylene ether glycol units. In addition, the polymers in the reference material, as well as the materials used in printer components, are cross-linked, which leads to an increase in density.

The comparison of the simulated and reference densities for C18 is complicated by the fact that this system has a melting point near room temperature. As such, the simulations performed at 300 K may not be sampling the solid system. However, the small nature of the simulation cell combined with their periodic repetition may affect the ability of the system to

adopt a configuration consistent with the liquid state. Optimization of the atomic structure and simulation cell, which yields structures at 0 K, yielded densities of ~1.0 g/cc, indicating that the density can be sensitive to temperature. This has been observed in experimental studies showing that the density of C18 can vary substantially with changes in temperature [72].

2.7 Analysis Methods

2.7.1 Movies

A common diagnostic tool in MD simulations is viewing a key event with movie visualization software. A movie file contains the Cartesian coordinates for each atom, for each frame separated by a specified time interval. Though these movie files are readily generated and viewed, they are most effective when there is a limited amount of material, and when the event of interest happens over a very short timescale (i.e. a few movie frames). For the simulations performed here, there is a large volume of material throughout which the slip event is distributed, so a precise location cannot be given to the event. Furthermore, the slip event does not occur rapidly, but rather over a sizeable length of time. Because of these limitations, movie analysis offers little support in locating key events. These events are quantified by a number of methods described in the sections to follow, and movie frames are used for confirmation of the location of the various materials at that point in time.

2.7.2 Shear Strength

As described in Section 2.3 on mechanical properties, the shear strength of a material may be used as a tool for locating the main slip event. All elements of the internal stress tensor are generated at requested intervals during the simulation, and the one associated with the direction of increasing external stress can be plotted to identify the point at which the material slips. The stress at this point corresponds to the shear strength, τ_c. These values can be obtained

with different normal loads, σ_{zz}, and the slope of a plot of τ_c versus σ_{zz} yields the friction coefficient.

2.7.3 Order Parameter from Bond Vector Components

Order parameters are typically used to quantify how structured a material is, which is of particular interest in phase transitions of mesomorphic materials [73]. The order of a single vector is defined in Eq. 2.18, where S is the order parameter, and θ is the angle between the vector and the direction of perfect orientation.

$$S = \frac{1}{2}(3\cos^2\theta - 1) \qquad \text{(Eq. 2.18)}$$

Since all of the atomic positions are known at requested steps during the simulations, and each bond pair is defined when the system is initially built, one could imagine being able to project each of these bonds onto the three Cartesian axes. In the equilibrated material, the bonds should all have random orientations and show no favour along any axis. As the system is sheared, however, the molecules reorganize in such a way that they begin to orient along the direction of shear. This can be seen by plotting the alignment of the bonds with respect to this direction. For the case of the materials studied here undergoing shear along the *x* direction, the equation for order parameter is altered to the form in Eq. 2.19.

$$S = \frac{1}{2}\left(\frac{3x^2}{r^2} - 1\right) = \frac{1}{2}\left(\frac{3x^2}{x^2+y^2+z^2} - 1\right) \qquad \text{(Eq. 2.19)}$$

The values for *x*, *y*, and *z* are the respective cumulative projections of the bonds (all except for those with hydrogen atoms) along the three axes. The *x* in the numerator is substituted for *y* when analyzing the simulations that are sheared in *y* instead of *x*. An order parameter value of 0 indicates perfectly random alignment and no favour in the direction of shear, whereas a value of 1 indicates perfect directional alignment. Since the projections are calculated on a per-bond basis (rather than per-molecule etc.) it is impossible for the systems to attain perfect alignment.

Once the material reaches its shear strength, the plot of the order parameter changes in behaviour such that it aligns in the direction of shear at an increasing rate. In the cases when more than one type of material is contributing to the system, an order parameter may be evaluated for each of the individual components. In this way, the material experiencing greater amounts of slip can be identified. An example of a PC slab with a C18 lubricant layer is shown here in Figure 2.8. The simulation cell may also be separated into fractions with an order parameter evaluated for each, as appears in Chapter 4, in order to locate the region of highest ordering.

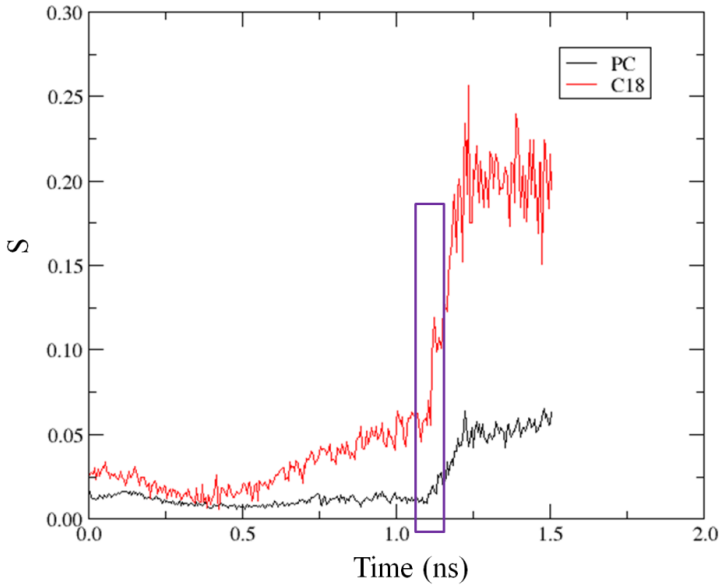

Figure 2.8. A plot comparing the change in order parameter for the two materials in a lubricated PC model. The region in the purple box indicates where the maximum internal stress, or shear strength, is reached.

2.7.4 Slip Distribution

In a perfectly elastic material, we expect deformation to occur uniformly, and with no slip. Under such circumstances, a plot of the displacement of the material as a function of height should be a straight line with a slope related to shear strain, and a plot of the relative displacements of neighbouring fractions of the material would be a vertical line. This behaviour is illustrated in the plots in Figure 2.9.

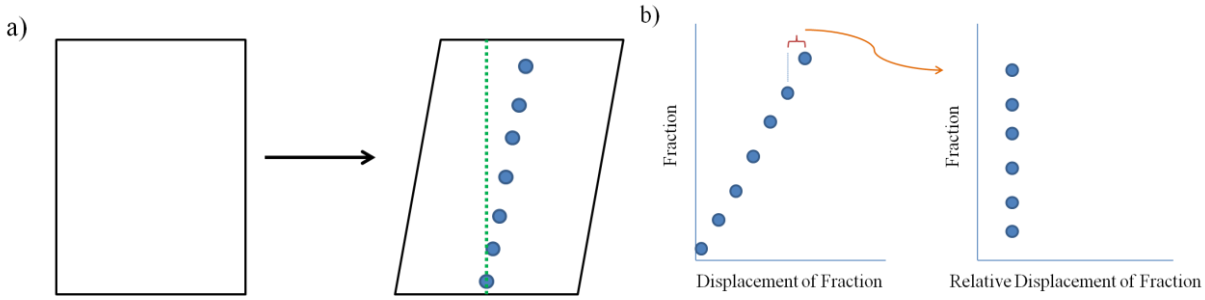

Figure 2.9. The schematic (a) shows how an elastic material might deform under shear stress. The graphs (b) show the displacement and relative displacement of the fractions. Because the deformation is evenly distributed along the material, it results in a flat "slip distribution", as shown in the second graph.

Were the material very brittle (no deformation except the slip), and the slip confined to a single plane, plotting the relative deformation in a similar way would present itself as a single peak along an otherwise flat line of no magnitude. This behaviour is illustrated by the plots in Figure 2.10.

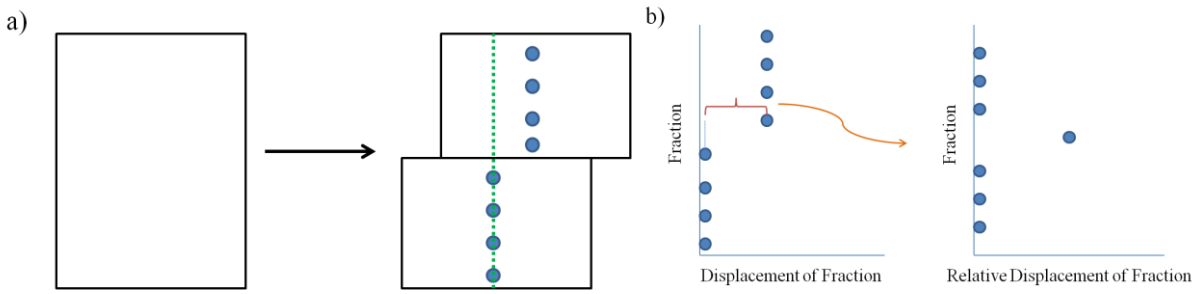

Figure 2.10. The schematic on the left shows how a brittle material might deform under shear stress. Because the deformation is localized, it results in a sharp "slip distribution", as shown in the graph on the far right.

Since the material being studied is neither perfectly elastic nor brittle, there will be a distribution of relative motions, the greatest of which should be located around the region where the main slip event occurs. The average lateral motion (in *x* or *y*, depending on the direction of shear) of each 10% fraction along the *z* axis was monitored during the shearing simulations. The relative motions with respect to neighbouring fractions were plotted near the time of the determined slip event. Since the active sections of these plots roughly resembled Gaussian distribution functions, the plots were fit to such an equation and the full width at half maximum

(FWHM) of the tallest available peak was extracted as a means of quantifying the distribution of slip (on occasion, slip was not very localized and two peaks were available). The fitting of a Gaussian curve is not meant to be meaningful itself, but was rather used as a tool to compare the regions of highest motion among the various simulations quantitatively. An example of the motion exhibited over a time segment, and the resulting relative motions are shown in Figure 2.11.

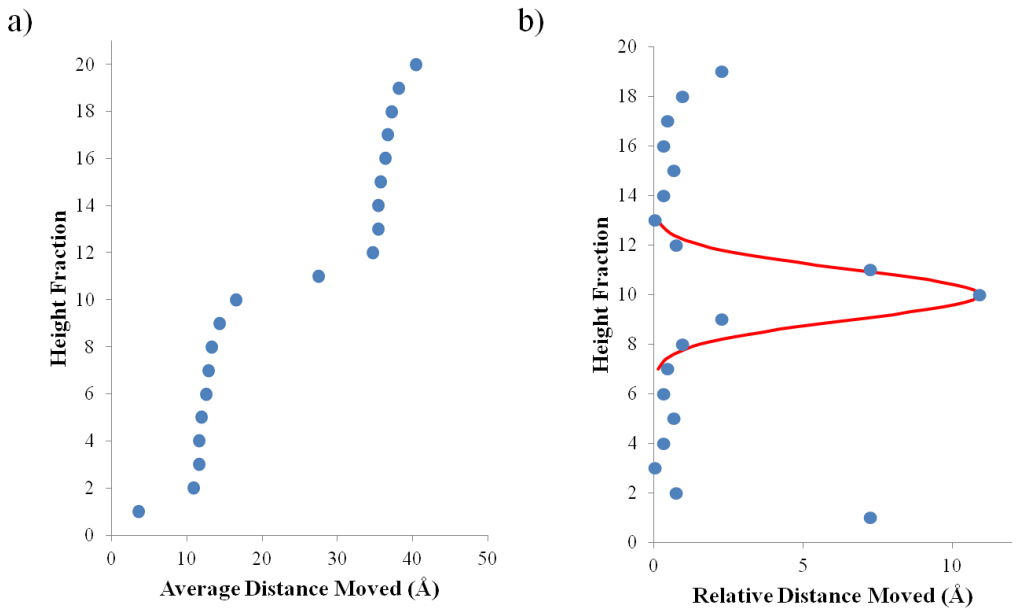

Figure 2.11. Plots of the motion of fractions of a material with an interface. Data was extended in the z-direction to represent an additional periodic repeat in order to be sure to capture and effects at the edge of the cell (hence an apparent height of 200%). Graph (a) shows the way that each fraction (10% of the height of the cell) has moved in one particular time segment around the time of slip. Graph (b) plots the difference between these average motions. The most active section of the distribution of motion can easily be approximated by a Gaussian-type curve, as shown in red. The FWHM of this particular peak is 2.39 fractions, or 23.9% of the cell height.

2.7.5 Material Distributions

The amounts of each material in the various height fractions of the cell were examined by evaluating the material distributions described below. Determining the amount of each material in each fraction helps correlate the locations at which slip and ordering of the material occurs with the type of material present at that location. In the evaluation of the material distributions,

weight was only given to non-hydrogen atoms, and since a list of such important bonds was already being used for the order distribution plots, the material locations were based on the location of bonds, which is quite similar to the individual atom locations.

The first representation, shown in Figure 2.12, is a component distribution, which quantifies the fraction of the total amount of a given material within a given fraction of the cell. This quantity is obtaining by dividing the number of bonds associated with a given material in a given height fraction of the cell by the total number of bonds associated with the same material in the entire cell. Integrating one of the curves that is produced along one full cell height yields 100%. There may, however, be a significant difference in the total amount of material available for each component.

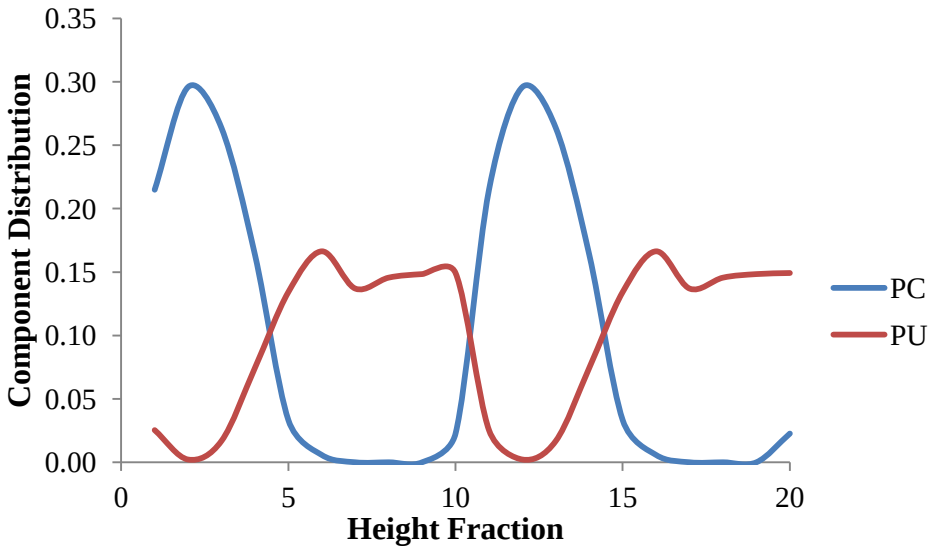

Figure 2.12. A component distribution of a PC/PU model. The fraction of material of the whole component is plotted for each fraction of cell height. A second periodic cell is plotted for clarity.

The second representation, shown in Figure 2.13, is a fraction distribution, which quantifies the amount of each material in a given height fraction. This quantity is evaluated by dividing the number of bonds associated with a given material in a height fraction by the total number of bonds in that height fraction. As such, the total amount of the material adds up to

100% in each fraction and the point where the curves for two materials cross correspond to locations where the system has equal amounts of each component. This distribution is useful in analyzing the composition of the system when there are multiple components that do not have equal amounts of material.

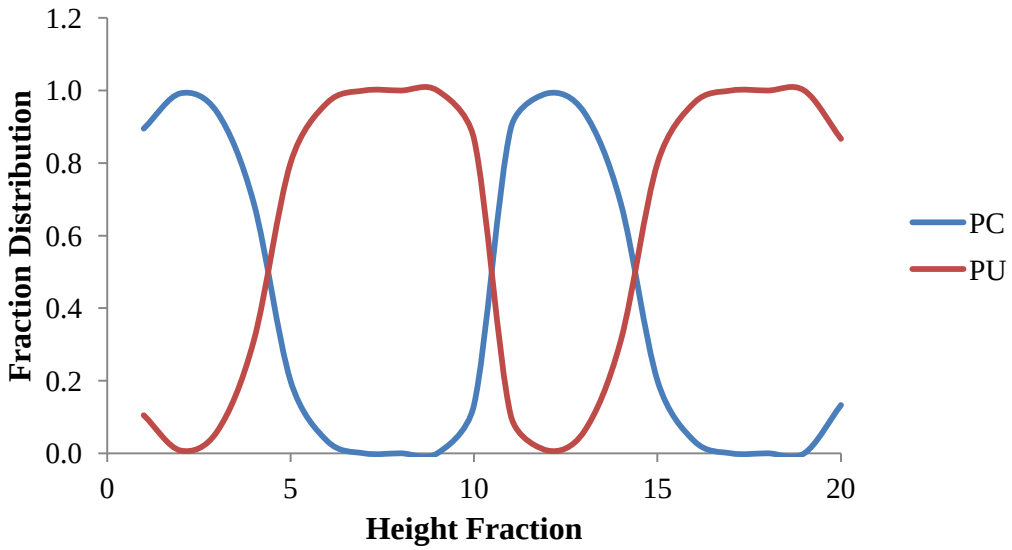

Figure 2.13. A fraction distribution of a PC/PU model. The composition of each fraction of cell height is plotted. A second periodic cell is plotted for clarity.

Chapter 3: Results

This chapter provides the results obtained in the simulations. The results are organized first by the type of system, then by the types of analysis done for each system. The chapter begins with an examination of the results of simulations of the bulk materials in Section 3.1. The results of simulations on dry interfaces are examined in Section 3.2. The outcomes of the simulations of systems with different levels of lubrication are then reported in Section 3.3 and 3.4. Each of these sections provides data for shear strengths, friction coefficients, order parameters, and slip distributions. Selected plots are provided to show any differences in character that were observed between the different simulations.

3.1 Bulk Material

The bulk models were created using the method described in Section 2.2.1. MD simulations were performed to obtain compressive and shear strengths of the materials by the methods in Section 2.3. The shear strengths are later compared to those of the models with interfaces, to demonstrate their differences.

3.1.1 Compressive Strengths

The determination of friction coefficients requires the evaluation of the shear strengths of the material at various normal loads. The compressive strength of the materials provides some insight into the selection of a reasonable set of normal loads to be considered for this purpose. As such, the compressive strengths of bulk PC and PU were evaluated as described in Section 2.3. In both cases, these materials were compressed by applying a compressive stress along the *z* axis that increased from 0 to 11.3 GPa over a period of 7 ns. The data (see Figure 2.3b) showed that PC yielded at a normal load of approximately 8 GPa, while PU did not yield within the range of stresses considered. Since the simulated value of ~8 GPa is based on a single simulation, it was

decided to round the compressive strength to 10 GPa and use this as an upper bound on the range of normal loads considered in the simulations.

3.1.2 Shear Strengths

The shear strengths of the bulk PC, PU and C18 models were evaluated according to the procedures described in Section 2.3. Recall that for bulk PC and PU, the tilt factor of the simulation cell was increased at a constant strain rate of 1.0 ns^{-1} due to limitations in the ability of the LAMMPS software to perform a simulation with an increasing external shear stress over a sufficient number of time steps to observe slip. Meanwhile, for the bulk C18 model, the σ_{xz} external stress component was increased at a rate of 1.62 GPa/ns. Plots of the stress-time relationships for each of these systems are given for each of these materials in Figure 3.1. In order to extract each shear strength, τ_c, a running average curve, with the data averaged over a range of 50 points, was constructed for each plot. The value of 50 provided sufficient smoothness of pressure fluctuations at the point of slip to select a clear maximum value, while retaining the general trend produced by the data. The maximum of this running average at the point of slip was assigned as the τ_c.

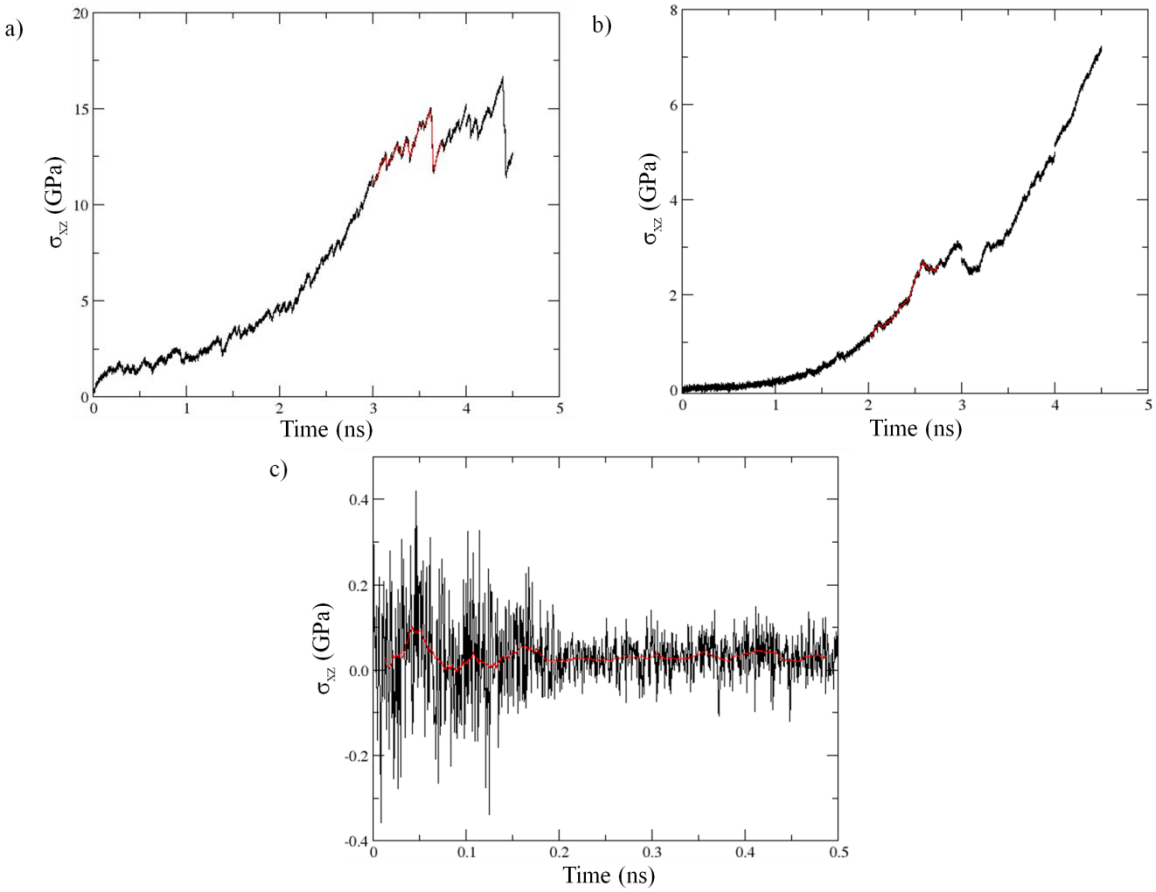

Figure 3.1. Shear strength plots for the three bulk models. Stress-time relationships are for (a) PC, (b) PU, and (c) C18. The black curve is obtained from the raw data, and the red curve is a running average over sets of 50 points.

The values of τ_c obtained for each system are given in Table 3.1 along with their associated cell heights. The data show that PC has the highest shear strength (14.90 GPa), while PU has a much lower strength of 2.70 GPa. As expected, the C18 lubricant has the lowest shear strength at 0.10 GPa. The relative order of the shear strengths of PC and PU are consistent with the relative order of the strengths of these materials measured in experiments, which are also included in Table 3.1. These reference material shear strengths were taken from two polycarbonate results, and one polyurethane result which was the densest available PU foam (0.80 g/cc, which is comparable to the simulated density of 0.72 g/cc) with an available measured shear strength. However, the results demonstrate that the calculated shear strengths are several orders of magnitude higher than the corresponding experimental values. This discrepancy

between calculated and experimental strengths is well-known and originates from the size-dependence of mechanical strength.

To assess whether the magnitude of this discrepancy is reasonable, the number of times, *N*, the simulation cell must be repeated along the *z* axis to reproduce the experimental strength was determined by the following expression [74]:

$$N = \left(\frac{\tau_c^{calc}}{\tau_c^{exp}}\right)^2 \quad \text{(Eq. 3.1)}$$

where τ_c^{calc} and τ_c^{exp} are the calculated and experimental shear strengths. The resulting values of *N* were then used to estimate the thickness of the experimental systems required to yield the experimental strengths. The resulting extrapolated thicknesses are on the order of 100s of μm, which is consistent with the sizes of materials usually used to perform strength measurements. Thus, while differences in the reference systems and experimental models complicates a direct comparison of the calculated shear strengths with those of the reference systems, the use of the calculated shear strengths to predict the sizes of experimental systems yields reasonable results. This indicates that the calculated shear strengths are likely reasonable values for these materials.

Table 3.1. Comparison of bulk PC, PU and C18 shear strengths, with comparison to reference material data. The reference materials were either thermoplastic (TP) or thermoset (TS).

Simulated			*Experimental* [75]		
Material	τ_c *(GPa)*	*Cell Height (nm)*	*Material*	τ_c *(MPa)*	*Extrapolated Thickness (μm)*
PC	14.90	5.37	PC (TP)	63.4	297
PU	2.70	6.48	PU (TS Foam)	16.0	185
C18	0.10	2.59	-	-	-

3.1.3 Order Parameters

The order parameters described in Section 2.7.3 were also evaluated during the simulations in which the PC, PU and C18 systems were sheared. The resulting plots are shown in

Figure 3.2. Recall that the order parameter provides a measure of the alignment of the bonds in the system with the shear direction. The data thus indicate an increasing alignment of the bonds along the shear direction over time for the PC and PU systems until the slip occurs at around 3.5 ns and 2.5 ns respectively, when there is some disturbance in the smoothness before continuing to increase. Meanwhile, the C18 system undergoes a rapid alignment of the bonds along the slip direction when slip occurs at ~0.05 ns.

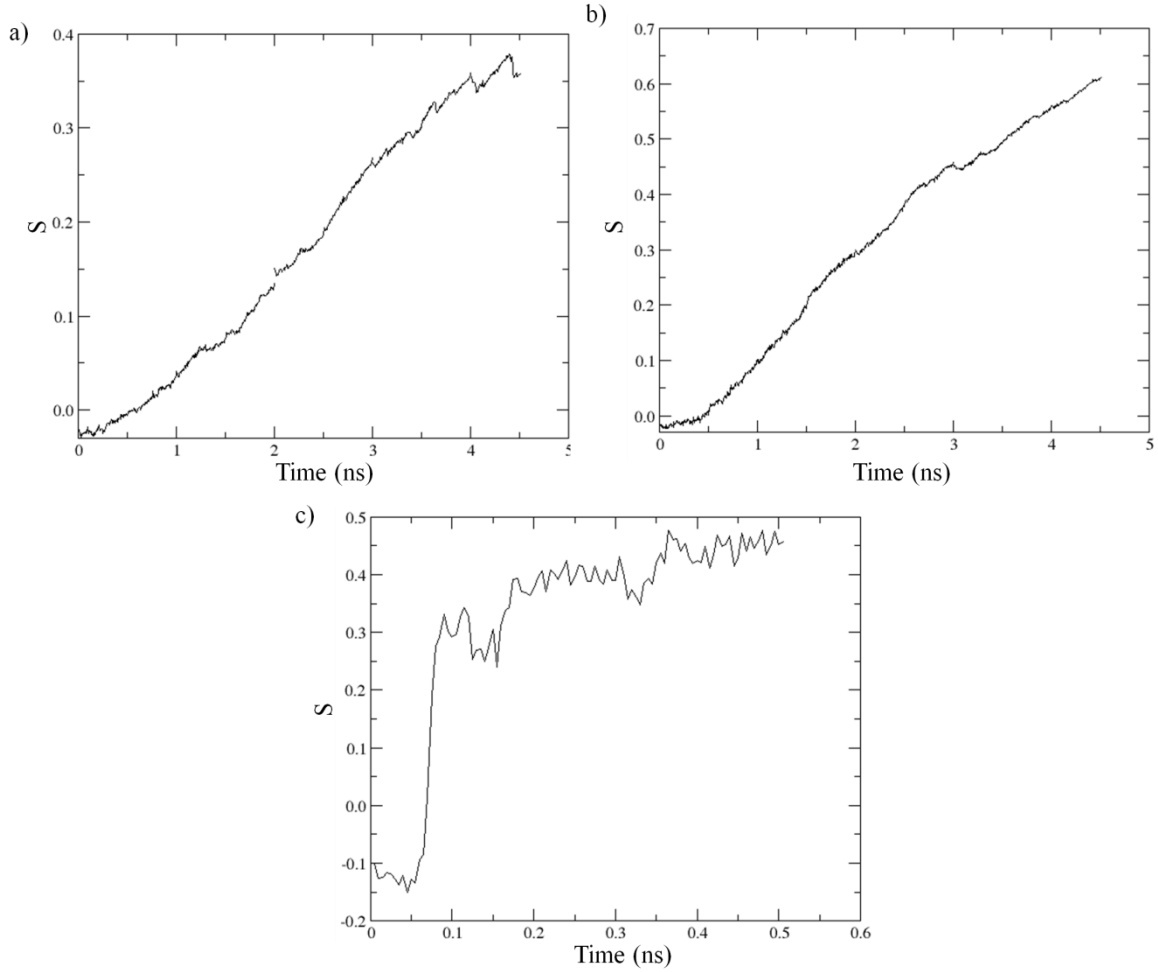

Figure 3.2. Order parameter plots of the three bulk materials, (a) PC, (b) PU, and (c) C18.

3.1.4 Slip Distributions

The slip distributions were quantified according to the approach described in Section 2.7.4. The FWHMs of the Gaussian functions fitted through the slip distributions are reported in

Table 3.2 for each system as both a distance and as a percentage of the thickness of the simulation cell. These data indicate the slip process for the bulk PC and PU systems occurs within a fairly localized portion of the simulation cell, as evidenced by FHWM of 12.1 and 12.9 % of cell height for PC and PU, respectively. Meanwhile, slip occurs throughout a broader range of the cell for C18, with a FWHM of 38.4%.

Table 3.2. Slip distribution values for each of the bulk models.

Bulk Material	*FWHM (%)*	*FWHM (Å)*
PC	12.1	6.5
PU	12.9	8.4
C18	38.4	9.9

3.2 Interfacial Systems (PC/PC, PU/PU and PC/PU)

Three different dry interfacial systems were constructed: PC/PC, PU/PU, and PC/PU. The construction of these models is described in Section 2.2.2. Recall that during the construction an amount of vacuum space was left before the equilibration process. Though this gap was inserted initially, by the end of the equilibration process it is not visible with animation software, and is still not clearly defined when the material above and below the inserted interface are coloured differently. This level of surface roughness and intermingling hinders the ability to analyze an animation of the simulation to identify changes in structure. Nonetheless, the results of the simulations still permit the study of the slip process in terms of shear strengths, ordering of bond directions and widths of slip distributions.

3.2.1 Rapid Compression

As described in Section 2.2.2, the models with interfaces were compressed as part of their preparation for shear. The external stress σ_{zz} was increased rapidly to ~10 GPa to compress the cell along the *z* direction, while the *x* and *y* dimensions of the cell were fixed. The resulting cell volumes are plotted in Figure 3.3 for the four different models of PC/PC and PU/PU. The

smooth deformation of the PU/PU models is attributed to its natural soft elastic properties, and the near stepwise deformation of the PC/PC models to its natural brittle properties. These features are especially apparent in the insets.

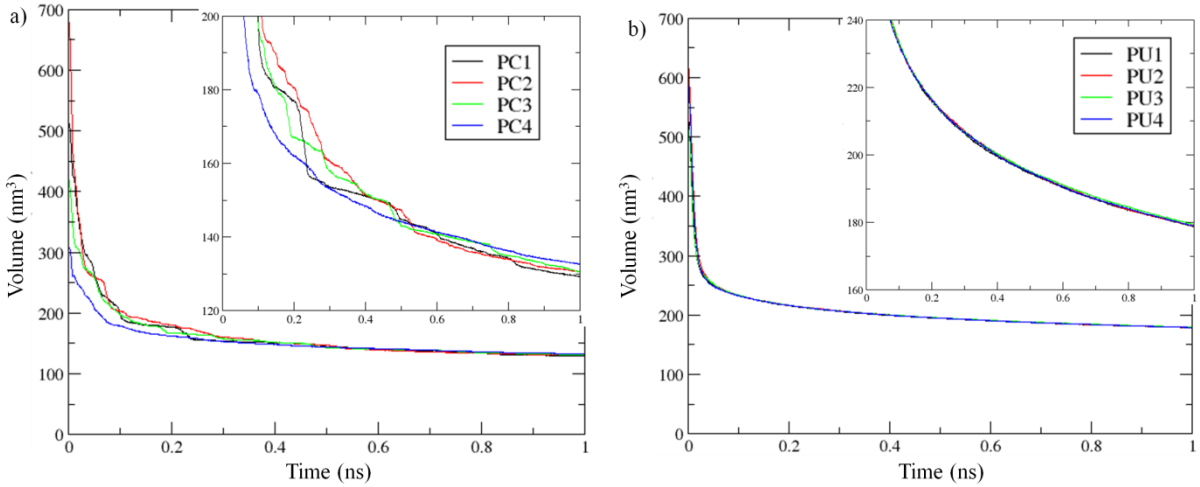

Figure 3.3. Plots of volume with response to increasing external pressure for (a) the four PC/PC models, and (b) the four PU/PU models. The respective insets better display the changes at higher normal load.

3.2.2 Shear Strengths

The method used for obtaining shear strengths is explained in Section 2.3, in which an external stress was applied to the simulation cell to cause it to shear. The data associated with the three differently composed dry interfaces are presented here. Linear fits are used to obtain coefficients of friction, which are summarized in Section 3.2.3. The normal pressures used were selected in units of atm, which are smaller than GPa by a factor of 9869.23. This means, for instance, that the system was subjected to a normal load of 10.13 GPa when a normal pressure of 100,000 atm was used. For the sake of simplicity, these normal loads will be rounded to the nearest 0.5 GPa (e.g. 10.13 will be referred to as 10 GPa); however, the actual normal loads used in the simulations have been used in the plots and analysis of data.

PC/PC

The shear strengths as a function of normal load are provided in Figure 3.4 for the four dry PC/PC models. Four distinct simulations were performed for each system at normal loads of 0, 5, and 10 GPa. These simulations differed in the direction in which the system was sheared, with directions of $\pm x$ and $\pm y$ being considered in all cases. The data illustrate the value of τ_c obtained for a given system is relatively insensitive to the shear direction. The data exhibit a linear relationship between τ_c and the normal load for all systems, which is anticipated because Amontons's law indicates there should be a linear relationship between these quantities. To ensure the linear relationship held, additional simulations were performed in which the PC4 model was sheared along the positive x direction at normal loads of 2.5 and 7.5 GPa. The resulting shear strengths lie close to the linear fit of the data for this system with normal loads of 0, 5, and 10 GPa, indicating that the linear relationship is valid.

The shear strengths for the PC1, PC2, and PC3 systems increase with normal load from values between 2 and 3 GPa when the load is zero to between 4 and 5 GPa at a normal load of 10 GPa. The shear strengths of the PC4 system are somewhat lower, increasing from ~0.5 GPa to ~2 GPa over the same range of normal loads. The differences between the strengths of PC4 and the other systems can likely be attributed to the fact that PC4 had a lower density. Recall that bulk PC had a shear strength of 14.9 GPa without the application of a normal load. As such, these results indicate that the introduction of an interface results in a significant reduction in the shear strength of PC even thought that interface may not be easily identified through visualization of the system.

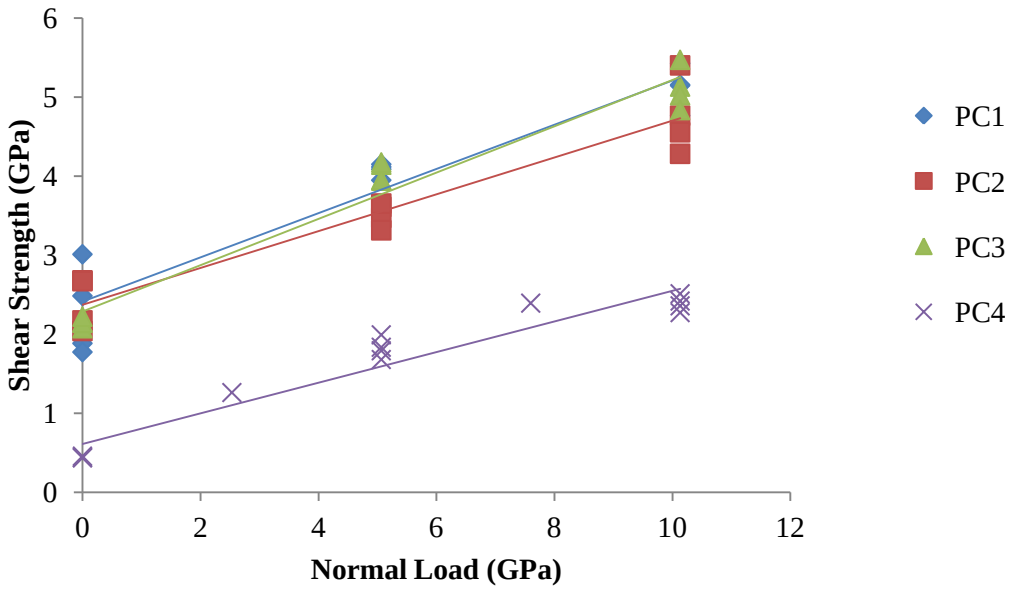

Figure 3.4. Shear strengths of the four dry PC/PC interface models. Lines of best fit are shown for each. The lower shear strengths of the PC4 model are easily explained by its noticeably lower density. The lines of best fit were based only on the shear strengths at 0, 5 and 10 GPa. Those at 2.5 and 7.5 GPa are displayed to emphasize the linear trend.

The shear strengths obtained from all simulations with normal loads of 0, 5, and 10 GPa were averaged and used to construct the relationship between τ_c and normal load shown in Figure 3.5. The data obtained with normal loads of 2.5 and 7.5 GPa for PC4 were excluded from this plot to ensure a consistent number of points were averaged at each normal load. The line provided is a fit of the original shear strengths at those three normal loads, and has a slope the same as the average of the slopes of the four models. These are provided in Section 3.2.3.

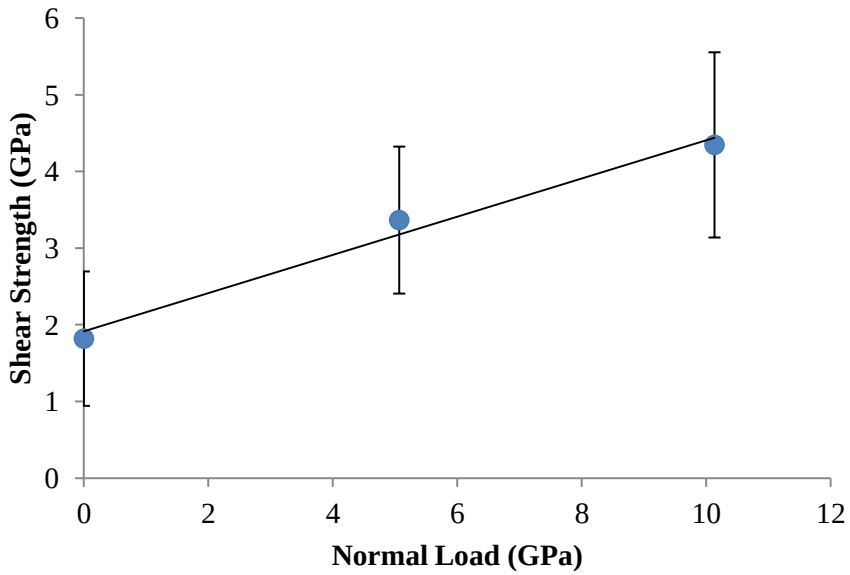

Figure 3.5. Shear strengths of the dry PC/PC models. Average shear strengths of the PC/PC interface models with error bars and an average line of best fit.

PU/PU

Simulations analogous to those discussed above for the PC/PC system were performed with four PU/PU dry interfaces. Once again four values of τ_c were obtained for each system at the three primary normal loads. These values were quite similar for all systems and simulations. The shear strengths were averaged at each normal load, with the resulting relationship between τ_c and the normal load summarized in Figure 3.6. These data show that the shear strength of the PU/PU system increases from ~0 GPa to 1.5 GPa over the range of normal loads considered. By comparison, the shear strength of bulk PU in the absence of a normal load was 2.7 GPa. Once again, this illustrates that the introduction of an interface lowers τ_c.

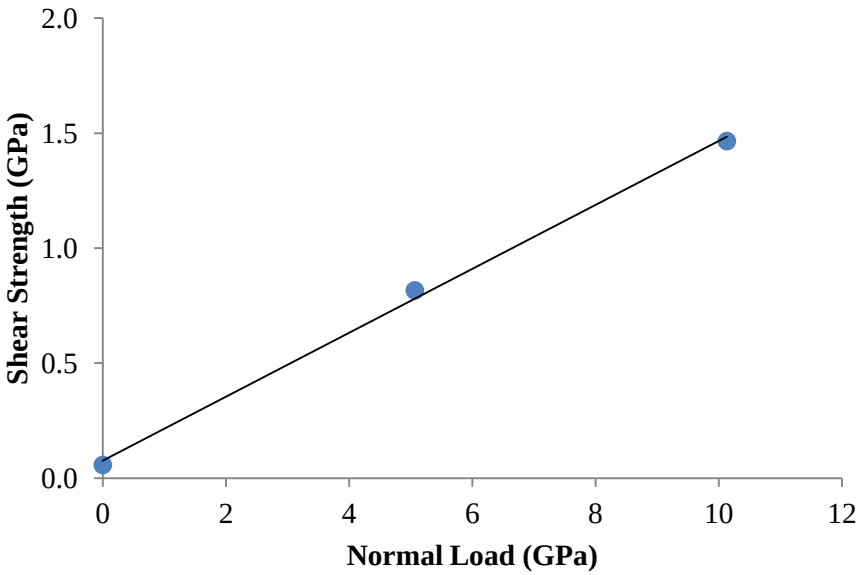

Figure 3.6. Shear strengths of the dry PU/PU models. Average shear strengths of the PU/PU interface models with error bars and an average line of best fit. The error bars are too small to be seen here.

PC/PU

Shear strengths were evaluated for six dry PC/PU models at normal loads of 0, 5, and 10 GPa. The values obtained in all simulations were quite similar at each normal load, and the averages of these values are reported in Figure 3.7. The data once again exhibit a linear relationship between τ_c and the normal load. From a quantitative standpoint, τ_c increases from ~0 GPa in the absence of a normal load to ~1.7 GPa when the normal load is near 10 GPa.

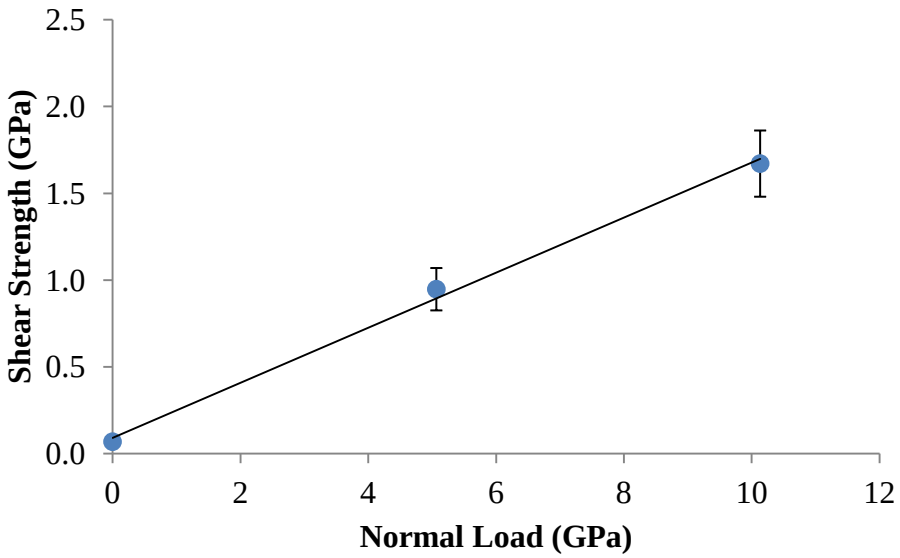

Figure 3.7. Shear strengths of the dry PC/PU models. Average shear strengths of the PC/PU interface models with error bars and an average line of best fit. Some error bars are too small to be seen here.

3.2.3 Friction Coefficients

The slopes of the fitted lines in the data of Section 3.2.2 correspond to the friction coefficients associated with these interfaces. The friction coefficients obtained for each of the dry interface models are tabulated in Table 3.3. The data demonstrate that the PC/PU and PU/PU system have very similar friction coefficients of 0.158 and 0.139, respectively. Meanwhile, the PC/PC interface has a higher friction coefficient of 0.249. The similarity between the friction coefficients of the PC/PU and PU/PU interfaces suggests that friction in the PC/PU system is determined by the PU component.

Table 3.3. Coefficient of friction and correlation coefficient for each dry interface model. Though some intermediate normal loads were simulated, they were not included in the linear fits.

Material	*Coeff. of Friction*	*Linear Fit R^2*
PC1	0.280 ± 0.058	0.910
PC2	0.233 ± 0.037	0.911
PC3	0.293 ± 0.032	0.960
PC4	0.192 ± 0.009	0.960
Average PC/PC	0.249 ± 0.054	
PU1	0.138 ± 0.002	0.998
PU2	0.140 ± 0.005	0.997
PU3	0.139 ± 0.005	0.995
PU4	0.138 ± 0.004	0.996
Average PU/PU	0.139 ± 0.004	
PC1/PU1	0.193 ± 0.013	0.995
PC1/PU3	0.143 ± 0.004	0.995
PC1/PU4	0.154 ± 0.004	0.998
PC2/PU1	0.158 ± 0.001	0.996
PC3/PU3	0.163 ± 0.006	0.999
PC4/PU3	0.140 ± 0.004	0.995
Average PC/PU	0.158 ± 0.019	

3.2.4 Order Parameters

The bond order parameter, *S*, described in Section 2.7.3 was evaluated during the simulation of each system. This order parameter will help illustrate structural changes consistent with an alignment of the system along the shear direction. Representative plots of *S* obtained from simulations of each type of interface considered at different loads are examined below. The plots given below all exhibit the qualitatively common feature of a sudden increase of *S* at the point of slip. This suggests that slip occurs along with a rapid change in the structure of the system.

PC/PC

The order parameters obtained for simulations of the PC4 model sheared along the *x* direction at normal loads of 0, 2.5, 5, 7.5, and 10 GPa are shown in Figure 3.8. In all cases, a drastic increase in *S* is observed at the same point in the simulation where slip occurred. In all

cases, the order parameter flattens after undergoing this sudden jump. The value of the *S* reached after slip occurred seems to increase with the normal load, though there is not an exact relationship between this value of *S* and the normal load. This observation suggests that the reorganization of the material during slip is greater at higher normal loads, which makes sense in light of the fact that increased density of the system at higher normal loads will increases interactions between the molecules contained in the system. It is also worth noting that the time at which the sudden jump in *S*, and hence slip, occurs increases steadily with the normal load. This indicates that it is necessary to shear the system to a greater extent to induce slip at higher normal loads.

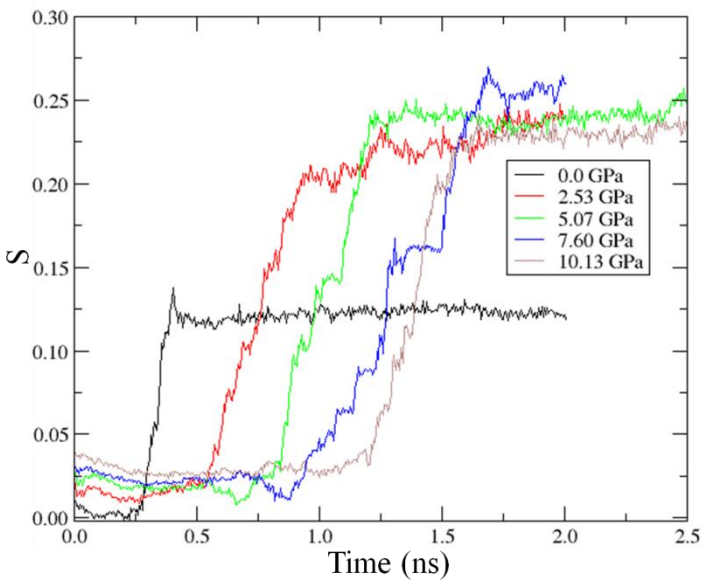

Figure 3.8. Order parameter samples for a range of normal loads during shear. The particular system is PC4, sheared in the *x* direction.

PU/PU

The values of *S* obtained during simulations of the PU4 interface model sheared along the *x* direction at normal loads of 0, 2.5, 5, 7.5, and 10 GPa are shown in Figure 3.9. The data are analogous to those reported above for the PC/PC interface, with relatively sharp increases in *S* occurring with slip. It is worth noting that the increases in *S* for this system are less steep than

those for the PC/PC interface indicating that slip in the PU/PU system involves a slower reorganization of the structure.

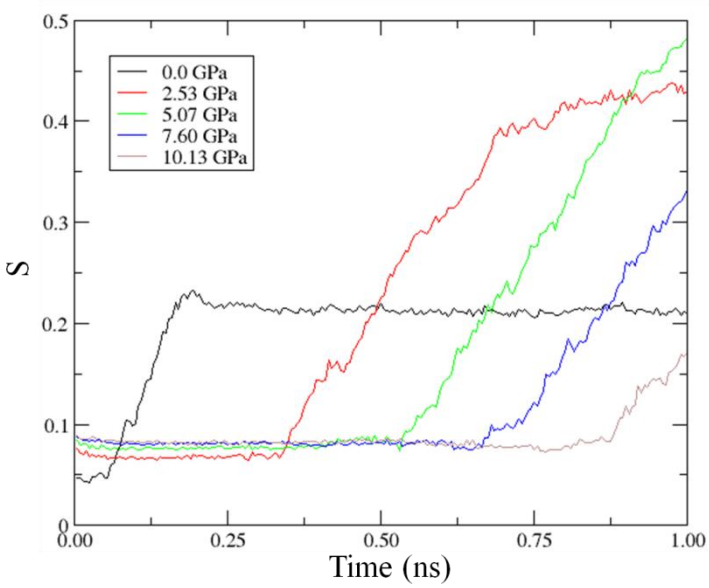

Figure 3.9. Order parameter samples for a range of normal loads during shear. The particular system is PU4, sheared in the *x* direction.

PC/PU

The values of *S* for the PC1/PU4 interface model sheared along the *x* direction at five different normal loads are summarized in Figure 3.10. Since there are two different materials present in this model, the order parameter analysis was performed separately for each. The data for the PU portion of the interface exhibit the sharp increases noted above for the systems containing interfaces between the same materials. Meanwhile, such sharp increases are not nearly as evident for the PC portion of the interface. In addition, the values of *S* reached for the PU portion are an order of magnitude greater than those reached for the PC component. Overall, this suggests that the slip process in the PC/PU interfaces is dominated by the reorganization of PU, with little effect on the structure of the PC component. This is consistent with the shear strengths and friction coefficients of the PU/PC interface described above.

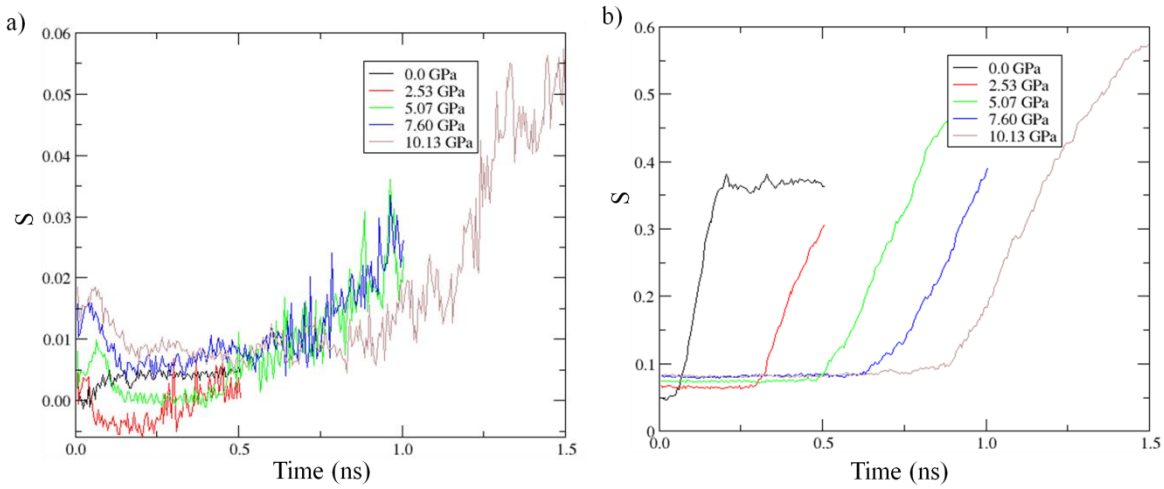

Figure 3.10. Order parameter samples for a range of normal loads during shear. The particular system is PC1/PU4, sheared in the *x* direction, with separate graphs for (a) the PC portion, and (b) the PU portion.

3.2.5 Slip Distributions

The slip distributions were evaluated with the method described in Section 2.7.4. Data for the three different types of dry interfaces are presented in Figures 3.11 and 3.12. It is important to note that the simulated systems may have significantly different cell heights. Data collected for normal loads of 2.5 and 7.5 GPa were omitted, since they were single measurements, and every other normal load had 16 or 24 measurements.

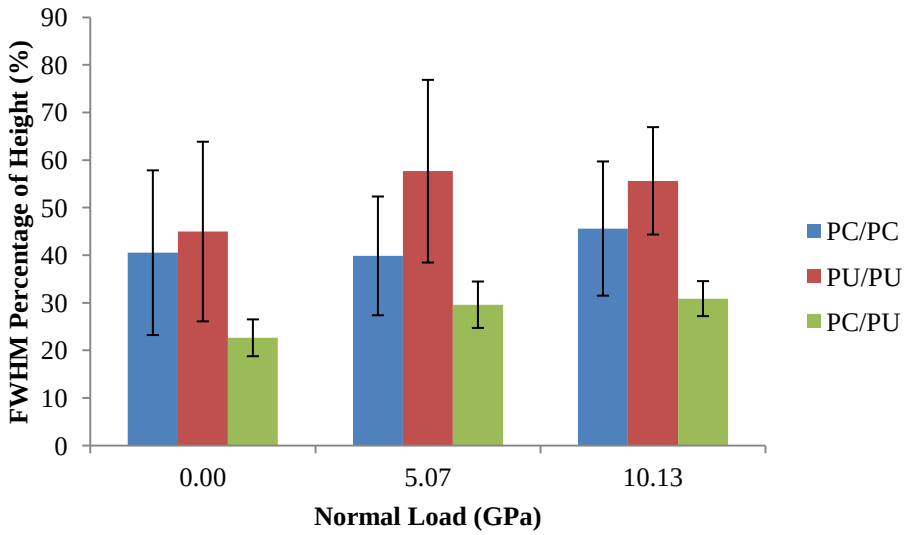

Figure 3.11. The FWHM of slip distribution as a height percent of the models with dry interfaces. Error bars are available from the 16, 16 and 24 measurements at each normal load for the PC/PC, PU/PU and PC/PU models, respectively.

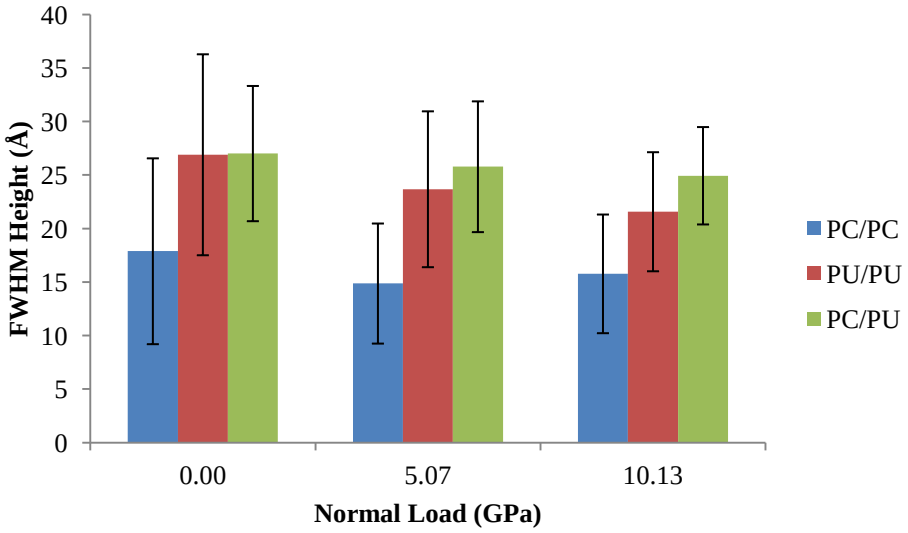

Figure 3.12. The FWHM of slip distribution as a height of the models with dry interfaces. Error bars are available from the 16, 16 and 24 measurements at each normal load for the PC/PC, PU/PU and PC/PU models, respectively.

The large FWHM percentage of height that slips for the PU/PU models suggests that a large portion of the cell is involved in the slip process and that it is widely distributed. Though there is a noticeably lower percentage of height involved in slip for the PC/PU models, it is attributed to the difference in cell heights (approximately twice as high as those of PC/PC and PU/PU). The absolute FWHM heights of the slip distribution suggests that the volume of

material involved in the slip process is more comparable between the PU/PU and PC/PU models, meanwhile the absolute FWHM heights for the PC/PC models are smaller, and therefore the slip process is more localized. As the normal load increases, the cells become more compressed, resulting in higher material densities. Overall, there is a very slight increase in percentage of cell height involved in the slip process as the normal load increases, suggesting that an increase in material involved in the slip process increases. Meanwhile, there is a very slight decrease in measured height, suggesting that the volume of material involved in the slip process decreases. The source of trends between the different models will become more evident when they are thoroughly analyzed in the discussion in Chapter 4.

3.3 Lubricated Systems (2 Molecular Layers)

Octadecane was added as a lubricant in the interfaces of the dry models described above. The construction of these lubricated models is described in Section 2.2.3, in which a slab of lubricating C18 was added to the interface of the previously defined dry interfacial models. Throughout this section, this amount of lubricant will be considered the "singly lubricated model" to keep it distinct for the later section which will be considered the "doubly lubricated model".

3.3.1 Shear Strengths

The method used for obtaining shear strengths is explained in Section 2.3, in which an external stress was applied to the simulation cell to cause it to shear. The data associated with the three differently composed lubricated interfaces are presented here. Linear fits are used to obtain coefficients of friction, which are summarized in Section 3.2.3.

PC/C18/PC

The shear strengths for the four singly lubricated PC/C18/PC models are provided in Figure 3.13, and range between 0 and 3 GPa under normal loads up to near 10 GPa. The significantly lower shear strengths upon the addition of C18 lubricant suggests that it plays a role in reducing the friction force. Similar to the difference with PC4 that was seen in the dry interfacial data in Figure 3.4, the lower shear strengths of the lubricated PC4 model are easily explained by its noticeably lower density. The values at normal loads of 2.5 and 7.5 GPa were included to emphasize the linear trend, but were excluded from the linear fit as well as the summary graph in Figure 3.14. The points for the summary graphs are an average of the individual shear strengths at each normal load, and the error bars are a standard deviation. The line shown was fit through the original data for those normal loads, and the slope is the same as the average of the four models with the same points. Recall that the shear strengths of bulk PC and bulk C18 with zero normal load were 14.9 and 0.1 GPa, respectively.

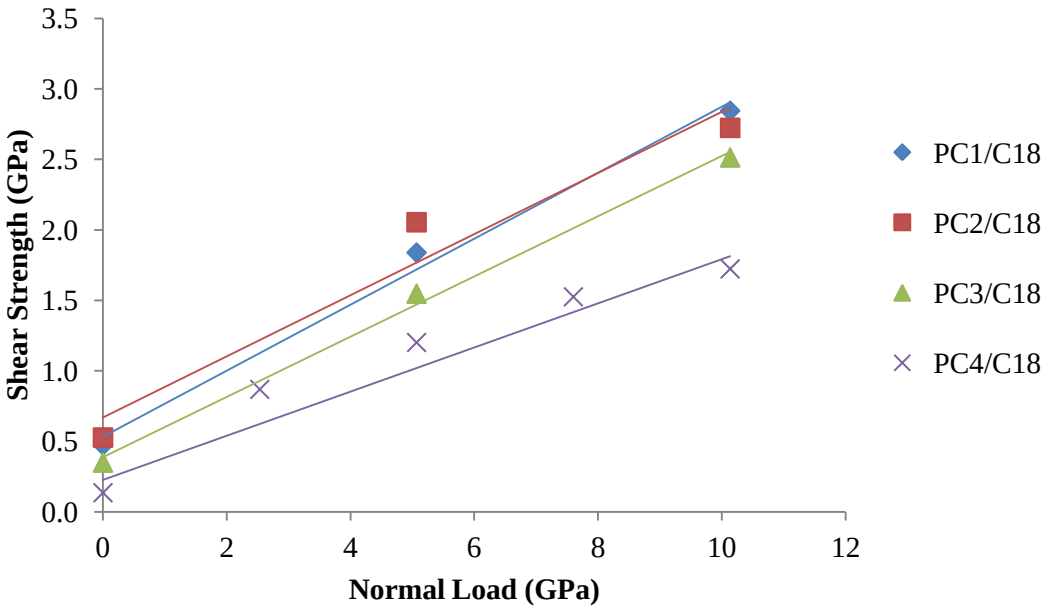

Figure 3.13. Shear strengths of the four singly lubricated PC/C18/PC interface models. Lines of best fit are shown for each. The lower shear strengths of the PC4 model are easily explained by its noticeably lower density. The lines of best fit were based only on the shear strengths at 0, 5 and 10 GPa. Those at 2.5 and 7.5 GPa are displayed to emphasize the linear trend.

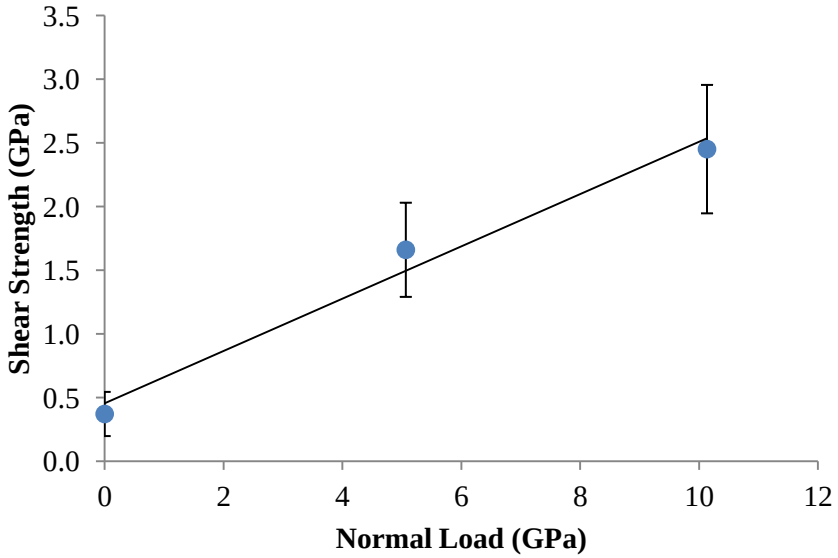

Figure 3.14. Shear strengths of the singly lubricated PC/C18/PC models. Average shear strengths of the singly lubricated PC/C18/PC interface models with error bars and an average line of best fit.

PU/C18/PU

The shear strengths for singly lubricated PU/C18/PU range between 0 and 1.5 GPa under normal loads up to 10 GPa. These are noticeably smaller than the shear strengths of the singly lubricated PC/C18/PC, which suggests that the friction forces here are not yet independent of surface composition. They are also slightly lower than those of dry interfacial PU/PU, which suggests that the C18 lubricant plays some role in lowering the shear strength. The plot provided in Figure 3.15 only contains the average values, since there was such good agreement between the different PU/C18/PU models, as is made evident by the small error bars. Recall that the shear strengths of bulk PU and bulk C18 with zero normal load were 2.7 and 0.1 GPa, respectively.

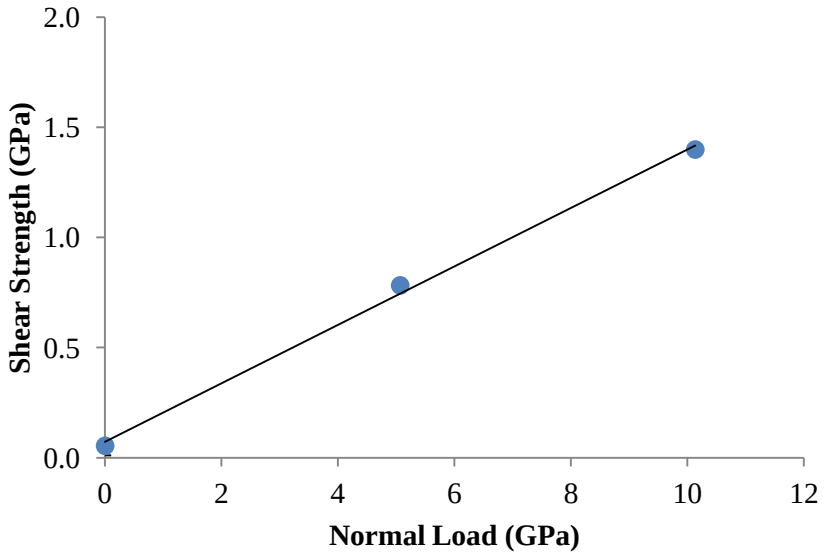

Figure 3.15. Shear strengths of the singly lubricated PU/C18/PU models. Average shear strengths of the singly lubricated PU/C18/PU interface models with error bars and an average line of best fit.

PC/C18/PU

The shear strengths for singly lubricated PC/C18/PU range between 0 and 1.75 GPa under normal loads up to 10 GPa. This lies somewhere between those of the lubricated PC/C18/PC and the lubricated PU/C18/PU models, reinforcing the idea that the surfaces still

play a role in the friction forces. The plot provided in Figure 3.16 only contains the average values, since there was such good agreement between the different PC/C18/PU models. The line provided was fit in the same way as described for each of the previous similar plots. Recall that the shear strengths of bulk PC, bulk PU and bulk C18 with zero normal load were 14.9, 2.7 and 0.1 GPa, respectively.

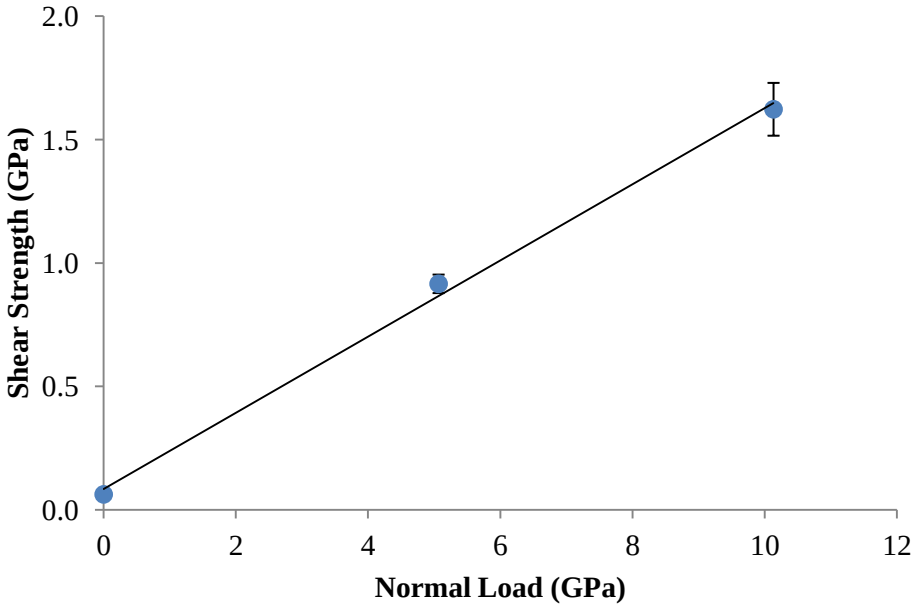

Figure 3.16. Shear strengths of the singly lubricated PC/C18/PU models. Average shear strengths of the singly lubricated PC/C18/PU interface models with error bars and an average line of best fit.

3.3.2 Friction Coefficients

The slopes of the fitted lines in the data of Section 3.3.1 are the friction coefficients associated with the material. Values of the individual slopes are tabulated in Table 3.4. It is worthwhile to point out that the coefficients of friction for the PC/C18/PU models (0.154) are roughly between those of the PC/C18/PC (0.205) and PU/C18/PU (0.133) models, though closer to the latter in a similar fashion to the comparison of the dry interfacial friction coefficients. Further comparisons between friction coefficients are made later on in the following chapter.

Table 3.4. Coefficient of friction and correlation coefficient for each singly lubricated interface model.

Lubricated Material	*Coeff. of Friction*	*Linear Fit R^2*
PC1	0.234	0.992
PC2	0.217	0.952
PC3	0.214	0.996
PC4	0.157	0.962
Average PC/C18/PC	0.205 ± 0.034	
PU1	0.137	0.999
PU2	0.130	0.995
PU3	0.130	0.997
PU4	0.134	0.999
Average PU/C18/PU	0.133 ± 0.003	
PC1/PU1	0.158	0.997
PC1/PU3	0.139	0.994
PC1/PU4	0.147	0.990
PC2/PU1	0.165	0.999
PC3/PU3	0.164	0.999
PC4/PU3	0.151	0.998
Average PC/C18/PU	0.154 ± 0.010	

3.3.3 Order Parameters

In a similar comparison as in the dry interfacial models, the order parameter plots are decomposed into separate plots for each material in the system. The mobility of the lubricant component perhaps makes the associated plots less comprehensive than the more rigid polymeric components, but still exhibit noticeable trends. These plots give a sense of the level of orientation exhibited in each of the components in the direction of shear.

PC/C18/PC

The order parameters for the components of singly lubricated PC4 sheared in the *x* direction for which five normal loads were tested, are shown in Figure 3.17. It is obvious that the PC material exhibits much less change in order than the C18 material does at the point of slip, though not an order of magnitude less as observed for the dry PC/PU model. It is clear that the

C18 lubricant does not prevent the PC component from being affected by sliding at non-zero normal loads.

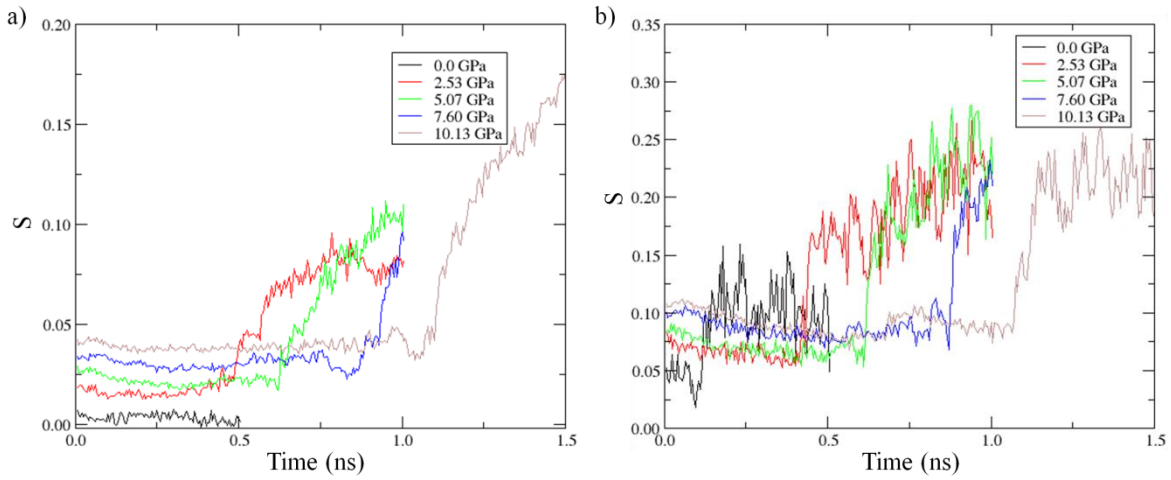

Figure 3.17. Order parameter samples for a range of normal loads during shear. The particular system is singly lubricated PC4, sheared in the *x* direction, with separate graphs for (a) the PC portion, and (b) the C18 portion.

PU/C18/PU

The order parameters for the components of singly lubricated PU4 sheared in the *x* direction for which five normal loads were tested, are shown in Figure 3.18. Note how the PU material deforms significantly, even while singly lubricated, though not as much as while it was dry. The lubricant appears to not even take on as much orientation as the PU does at higher normal loads, as they have comparable *S* values at 2.5 GPa of normal load. The rates at which the two components alter are also comparable to each other.

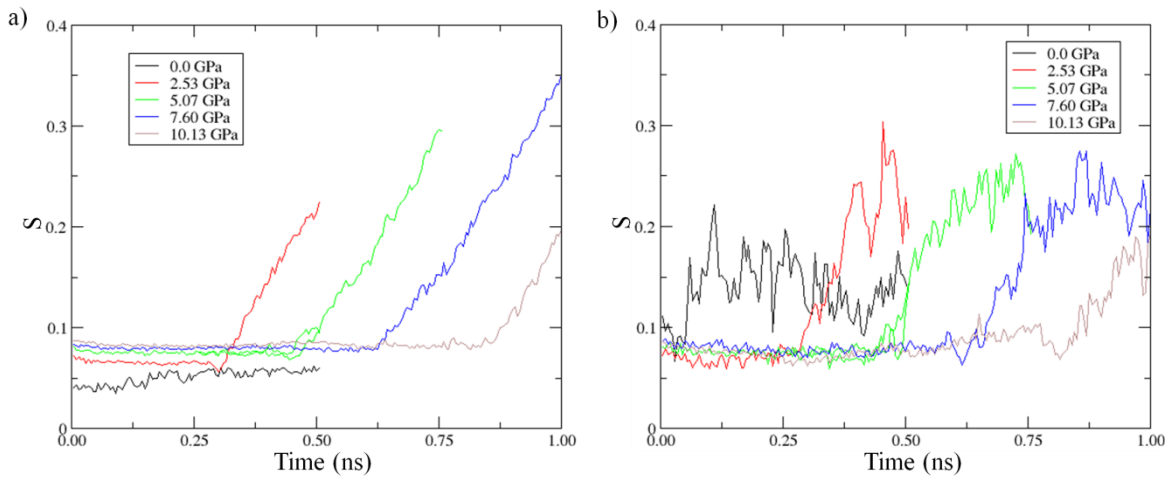

Figure 3.18. Order parameter samples for a range of normal loads during shear. The particular system is singly lubricated PU4, sheared in the *x* direction, with separate graphs for (a) the PU portion, and (b) the C18 portion.

PC/C18/PU

The order parameters for the components of singly lubricated PC1/C18/PU4 sheared in the *x* direction for which five normal loads were tested, are shown in Figure 3.19. For comparison sake, the PC component shows effectively no response in order, especially when compared to the other two components. The C18 lubricant is just as responsive as in the previous two models; however, the PU component responds as drastically as it did in the dry model with no lubrication at all. It is not even able to maintain its structure in the absence of normal load. The response time of the lubricant is however, faster than that of the PU. Further investigation of this is later on in the following chapter, which should provide a source for this behaviour.

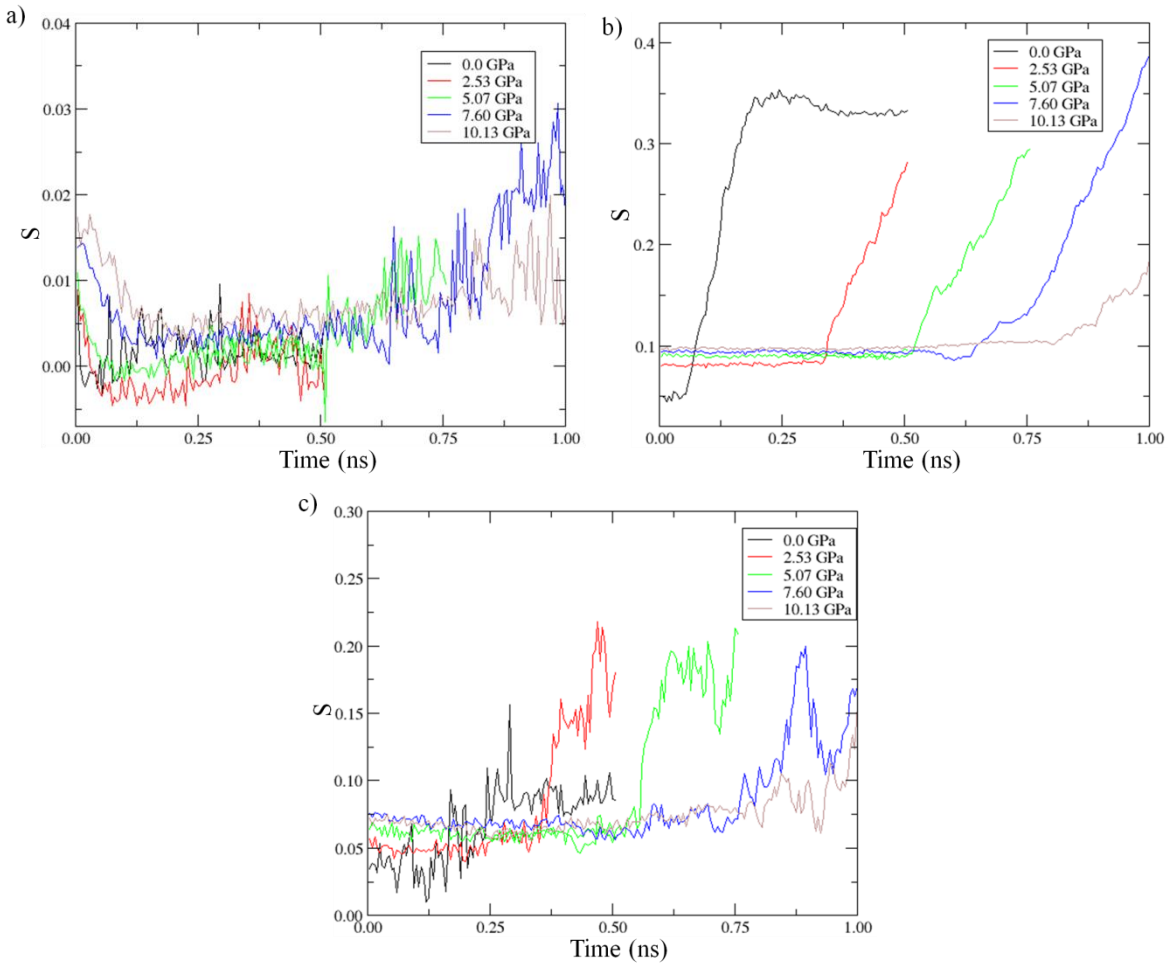

Figure 3.19. Order parameter samples for a range of normal loads during shear. The particular system is singly lubricated PC1/C18/PU4, sheared in the *x* direction, with separate graphs for (a) the PC portion, (b) the PU portion, and (c) the C18 portion.

3.3.4 Slip Distributions

The slip distributions were evaluated with the method described in Section 2.7.4. Data for the three differently comprised dry interfaces are presented here in Figures 3.20 and 3.21. It is important to remember that the simulations may have significantly different cell heights. Data collected for 2.5 and 7.5 GPa were omitted, since they were single measurements, and every other normal load had 4 or 6 measurements.

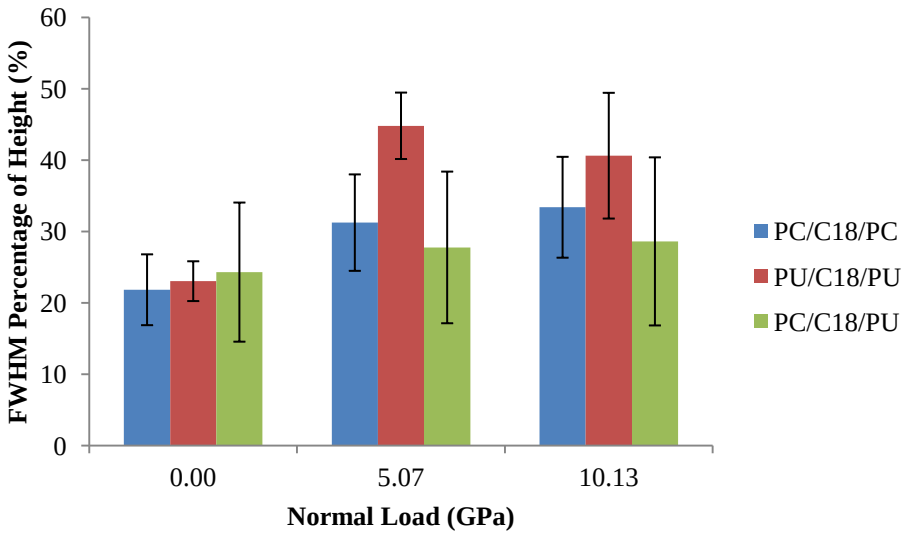

Figure 3.20. The FWHM of slip distribution as a height percent of the models with singly lubricated interfaces. Error bars are available from the 4, 4 and 6 measurements at each normal load for the PC/C18/PC, PU/C18/PU and PC/C18/PU models, respectively, except 2.5 and 7.5, for which there was only one measurement of each.

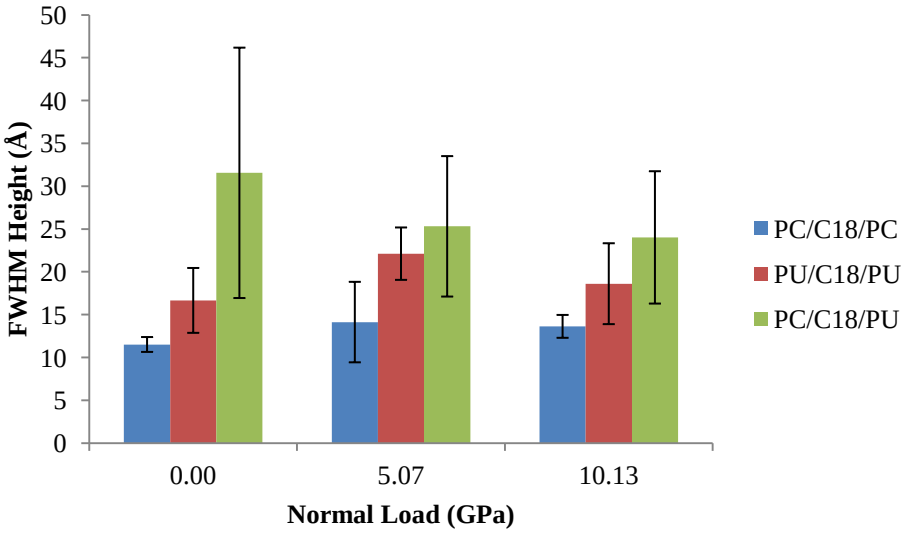

Figure 3.21. The FWHM of slip distribution as a height of the models with singly lubricated interfaces. Error bars are available from the 4, 4 and 6 measurements at each normal load for the PC/C18/PC, PU/C18/PU and PC/C18/PU models, respectively, except 2.5 and 7.5, for which there was only one measurement of each.

More distinctly than in the dry interfacial models, the FWHM percentage height seems to increase as the normal load increases. In cases where the absolute FWHM height is relatively smaller compared to the dry interfacial models, this suggests that slip is more localized with the

addition of lubricant. Here, they also suggest that the volume of material involved in the slip process is noticeably greater for the lubricated PC/C18/PU models than the lubricated PC/C18/PC and PU/C18/PU models, which is not anticipated, as the PC components do not contribute significantly to the deformation and increase in order parameter (refer to Section 3.3.3). Additionally, the amount of material contributing to the slip is sometimes surprisingly increased from the values for the dry interfacial material. Later, the original slip distribution plots (which the FWHM values were extracted from) will be compared to material distribution plots to get a sense of where in the model the slip is occurring, and how this plays a role in the values of slip distribution that are observed here.

3.4 Lubricated Systems (4 Molecular Layers)

Since the results of the singly lubricated models did not seem to provide sufficient lubrication of the surfaces, an additional slab of lubricant was inserted to examine the effects thereof. The construction of these models is described in Section 2.2.3, in which a double slab of lubricating C18 (2C18) was added to the interface of the previously defined dry interfacial models. Throughout this section, this amount of lubricant will be considered the "doubly lubricated model", to keep it distinct from the earlier section, which was considered the "singly lubricated model".

3.4.1 Shear Strengths

The method used for obtaining shear strengths is explained in Section 2.3, in which an external stress was applied to the simulation cell to cause it to shear. The data associated with the three differently composed lubricated interfaces are presented here. Linear fits are used to obtain coefficients of friction, which are summarized in Section 3.2.3.

PC/2C18/PC

The shear strengths for the four doubly lubricated PC/2C18/PC models are provided in Figure 3.22, and range between 0 and 2 GPa under normal loads up to near 10 GPa. Significantly lower shear strengths including adhesion forces are observed upon the addition of a second slab of C18 lubricant. The values for normal loads of 2.5 and 7.5 GPa were excluded from the linear fit as well as the graph. The points provided are an average of the individual shear strengths at each normal load, and the error bars are a standard deviation. It is interesting to note that the error in measurement has also decreased for interfacial PC as lubrication has increased. The line shown was fit through the original data for those normal loads, and the slope is the same as the average of the four models with the same points. Recall that the shear strengths of bulk PC and bulk C18 with zero normal load were 14.9 and 0.1 GPa, respectively.

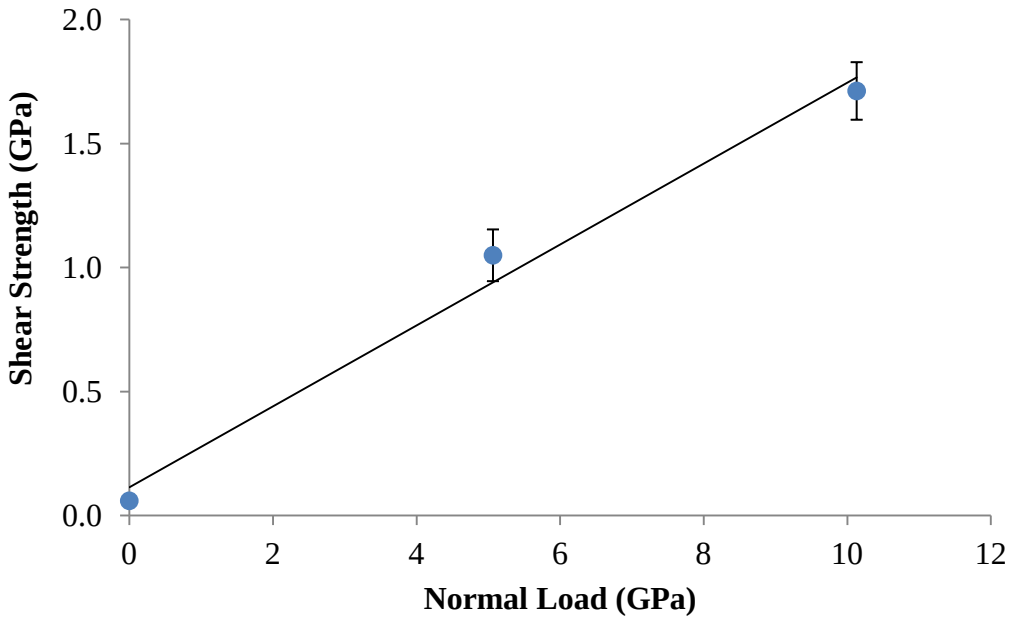

Figure 3.22. Shear strengths of the doubly lubricated PC models. Average shear strengths of the doubly lubricated PC/2C18/PC interface models with error bars and an average line of best fit.

PU/2C18/PU

The shear strengths for doubly lubricated PU/C18/PU range between 0 and 1.4 GPa under normal loads up to near 10 GPa. These are somewhat smaller than the shear strengths of the singly lubricated PU, and still lower than the doubly lubricated PC. The C18 lubricant is clearly playing some role in lowering the shear strengths, though there is still some effect that the surfaces contribute. The plot provided in Figure 3.23 only contains the average values, since there was such good agreement between the different PU/C18/PU models, as is made evident by the small error bars. Recall that the shear strengths of bulk PU and bulk C18 with zero normal load were 2.7 and 0.1 GPa, respectively.

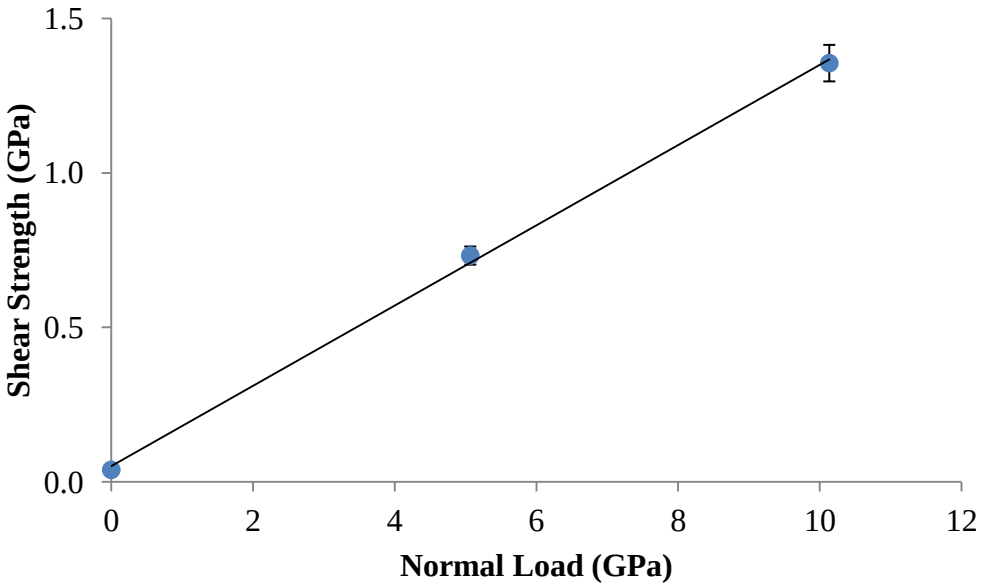

Figure 3.23. Shear strengths of the doubly lubricated PC/2C18/PC models. Average shear strengths of the doubly lubricated PC/2C18/PC interface models with error bars and an average line of best fit.

PC/2C18/PU

The shear strengths for doubly lubricated PC/2C18/PU range between 0 and 1.5 GPa under normal loads up to 10 GPa, which is a slight decrease from the values obtained with single lubrication. These values lie somewhere between those of the two other doubly lubricated

models, again reinforcing the idea that the surfaces still play a role in the friction forces. The plot provided in Figure 3.24 only contains the average values, since there was such good agreement between the different PC/2C18/PU models. The line provided was fit in the same way as described for each of the previous similar plots. Recall that the shear strengths of bulk PC, bulk PU and bulk C18 with zero normal load were 14.9, 2.7 and 0.1 GPa, respectively.

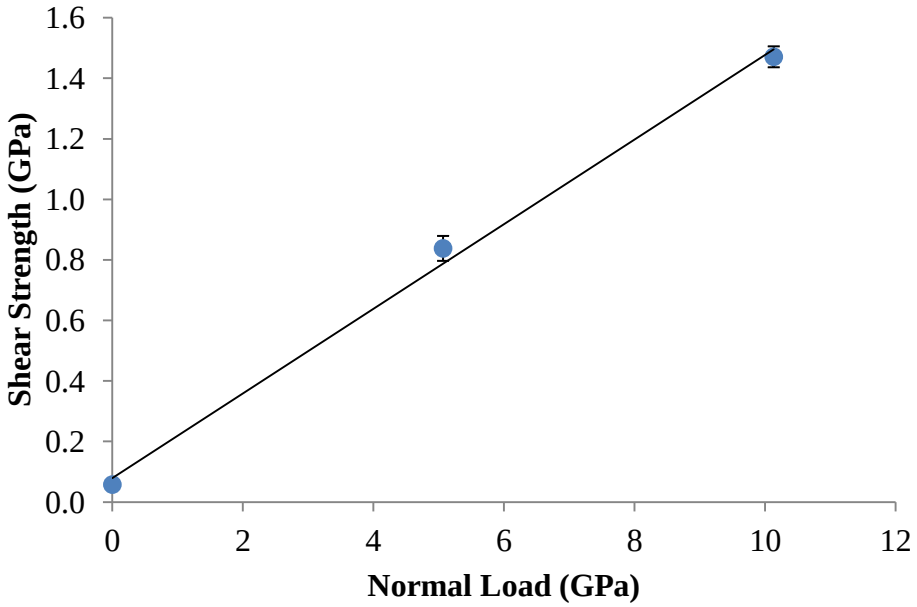

Figure 3.24. Shear strengths of the doubly lubricated PC/2C18/PU models. Average shear strengths of the doubly lubricated PC/2C18/PU interface models with error bars and an average line of best fit.

3.4.2 Friction Coefficients

The slopes of the fitted lines in the data of Section 3.4.1 are the friction coefficients associated with the material. Values of the individual slopes are tabulated in Table 3.4. It is worthwhile to point out that the coefficients of friction for the PC/2C18/PU models (0.139) are roughly between those of the PC/2C18/PC (0.163) and PU/2C18/PU (0.130) models, though closer to the latter in a similar fashion to the comparison of the dry and singly lubricated interfacial friction coefficients. Further comparisons are made later on in the following chapter.

Table 3.5. Coefficient of friction and correlation coefficient for each singly lubricated interface model.

Lubricated Material	*Coeff. of Friction*	*Linear Fit R^2*
PC1	0.171	0.993
PC2	0.155	0.946
PC3	0.176	0.995
PC4	0.151	0.995
Average PC/2C18/PC	0.163 ± 0.012	
PU1	0.125	0.998
PU2	0.133	0.999
PU3	0.125	0.998
PU4	0.137	0.999
Average PU/2C18/PU	0.130 ± 0.006	
PC1/PU1	0.144	0.993
PC1/PU3	0.141	0.996
PC1/PU4	0.135	0.996
PC2/PU1	0.138	0.993
PC3/PU3	0.142	0.998
PC4/PU3	0.137	0.999
Average PC/2C18/PU	0.139 ± 0.003	

3.4.3 Order Parameters

In a similar comparison as in the other interfacial models, the order parameter plots are decomposed into separate plots for each material in the system. The mobility of the lubricant component is somewhat more defined here with the increase in volume, and exhibits more noticeable trends. These plots give a sense of the level of orientation exhibited in each of the components in the direction of shear.

PC/2C18/PC

The order parameters for the components of doubly lubricated PC4 sheared in the *x* direction for which five normal loads were tested, are shown in Figure 3.25. It is obvious that the PC material exhibits much less change in order than the C18 material does at the point of slip; slightly less change than the singly lubricated analog showed, though not an order of magnitude less as observed for the dry PC/PU model. It is clear that the C18 lubricant does not prevent the

PC component from being affected by sliding at higher normal loads, but is effective at protecting the PC material from deforming to a certain degree.

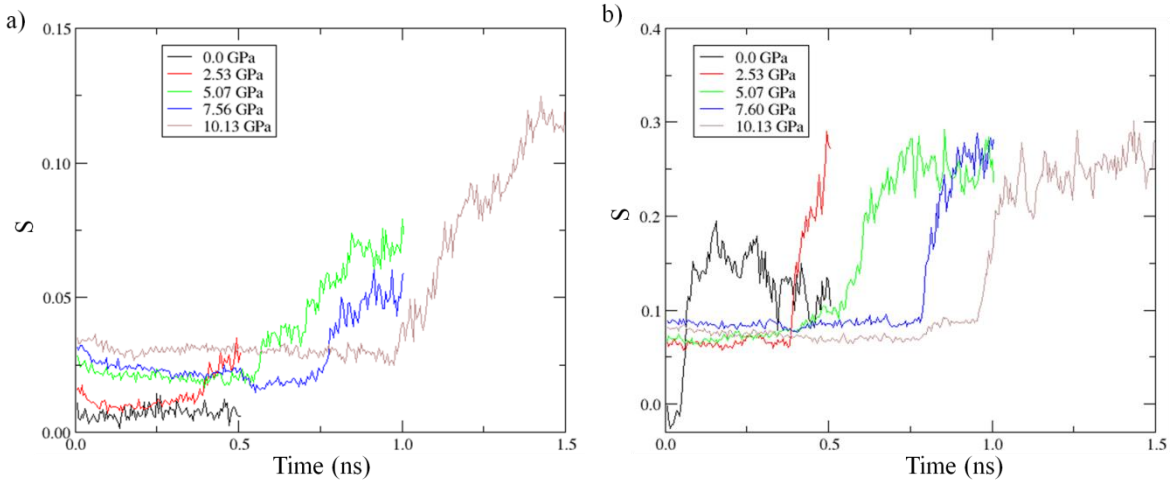

Figure 3.25. Order parameter samples for a range of normal loads during shear. The particular system is doubly lubricated PC4, sheared in the *x* direction, with separate graphs for (a) the PC portion, and (b) the C18 portion.

PU/2C18/PU

The order parameters for the components of doubly lubricated PU4 sheared in the *x* direction for which five normal loads were tested, are shown in Figure 3.26. The ordering exhibited is almost identical to that of the singly lubricated analog. This suggests that the addition of more lubricant does very little in the way of keeping the PU material from deforming during shear, though it does have a lower rate of ordering once slip has occurred.

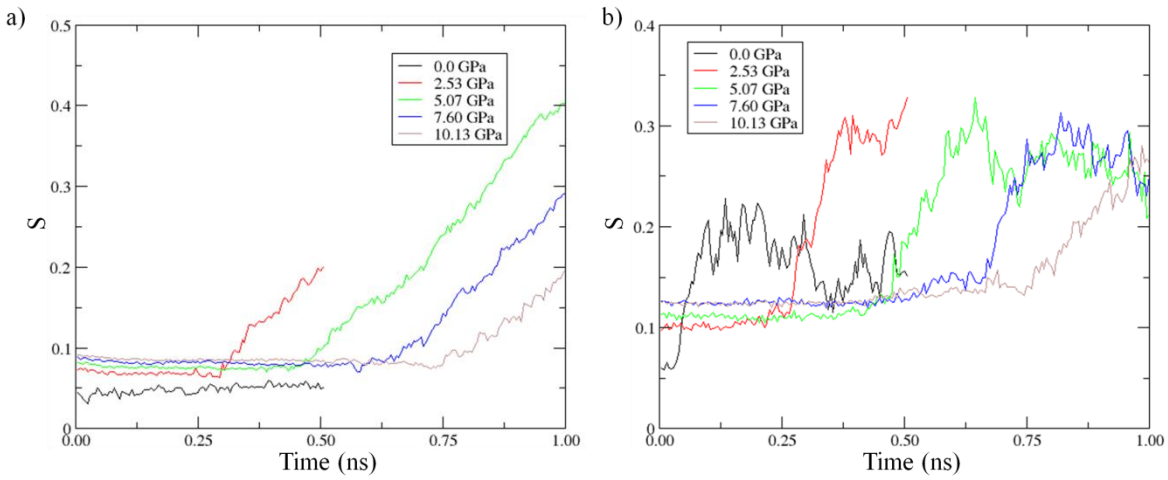

Figure 3.26. Order parameter samples for a range of normal loads during shear. The particular system is doubly lubricated PU4, sheared in the *x* direction, with separate graphs for (a) the PU portion, and (b) the C18 portion.

PC/2C18/PU

The order parameters for the components of doubly lubricated PC1/2C18/PU4 sheared in the *x* direction for which five normal loads were tested, are shown in Figure 3.27. The PC component shows effectively no response in order, especially when compared to the other two components. The C18 lubricant is just as responsive as in all of the previous plots, however the PU component responds somewhat less drastically than the singly lubricated analog, and responds almost exactly the same as the doubly lubricated PU model. The lubricant responds quite suddenly at the point of slip, while the PU component has a gradual increase of ordering. Further investigation of this is presented later on in the following chapter.

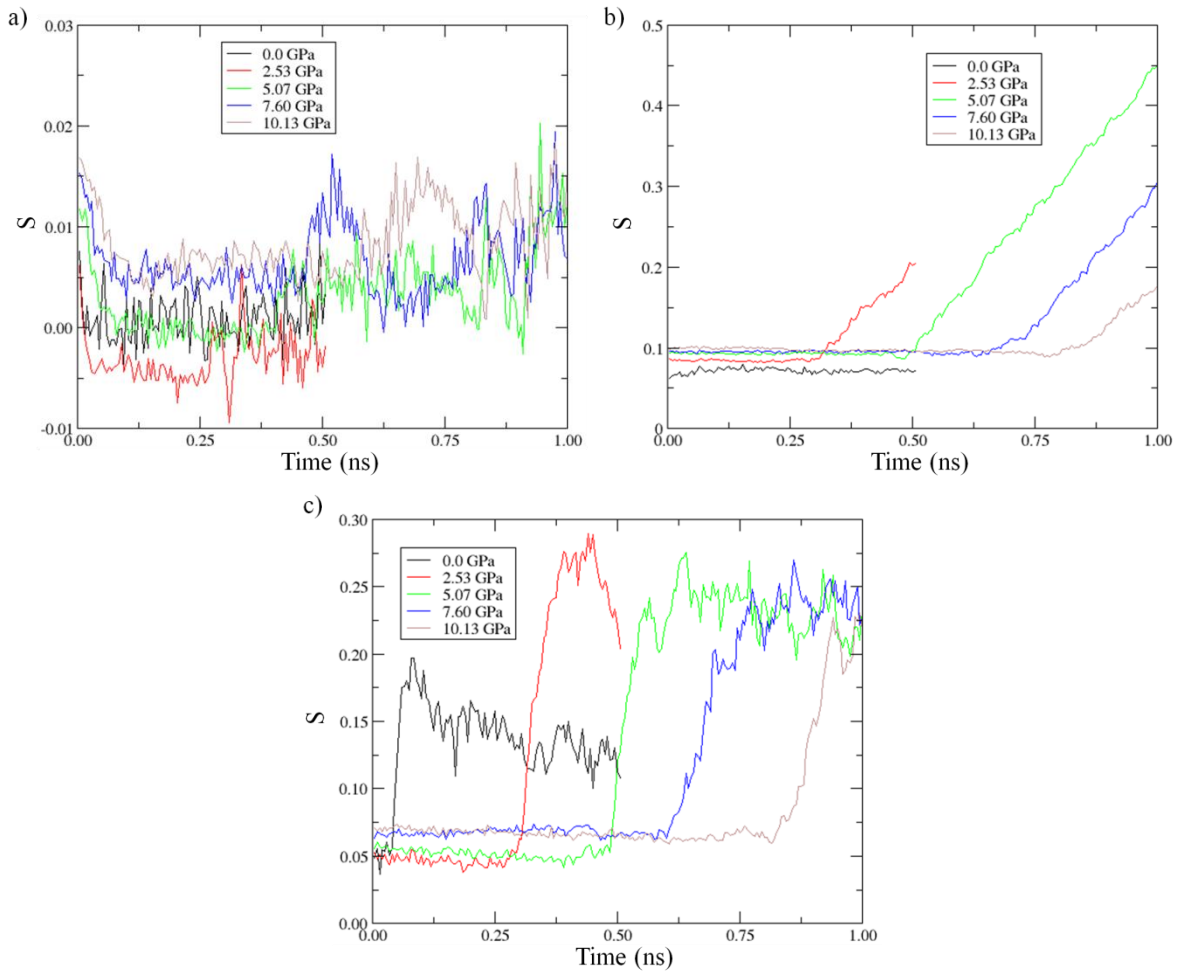

Figure 3.27. Order parameter samples for a range of normal loads during shear. The particular system is doubly lubricated PC1/2C18/PU4, sheared in the *x* direction, with separate graphs for (a) the PC portion, (b) the PU portion, and (c) the C18 portion.

3.4.4 Slip Distributions

The slip distributions were evaluated with the method described in Section 2.7.4. Data for the three differently comprised doubly lubricated interfaces are presented here in Figures 3.28 and 3.29. It is important to remember that the simulations may have significantly different cell heights. Data collected for 2.5 and 7.5 GPa were omitted, since they were single measurements, and every other normal load had 4 or 6 measurements.

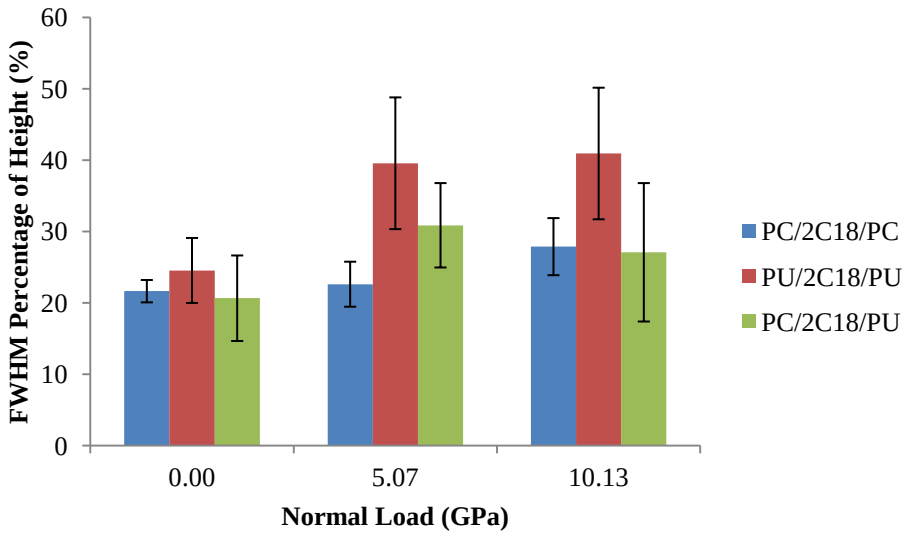

Figure 3.28. The FWHM of slip distribution as a height percent of the models with doubly lubricated interfaces. Error bars are available from the 4, 4 and 6 measurements at each normal load for the PC/2C18/PC, PU/2C18/PU and PC/2C18/PU models, respectively, except 2.5 and 7.5, for which there was only one measurement of each.

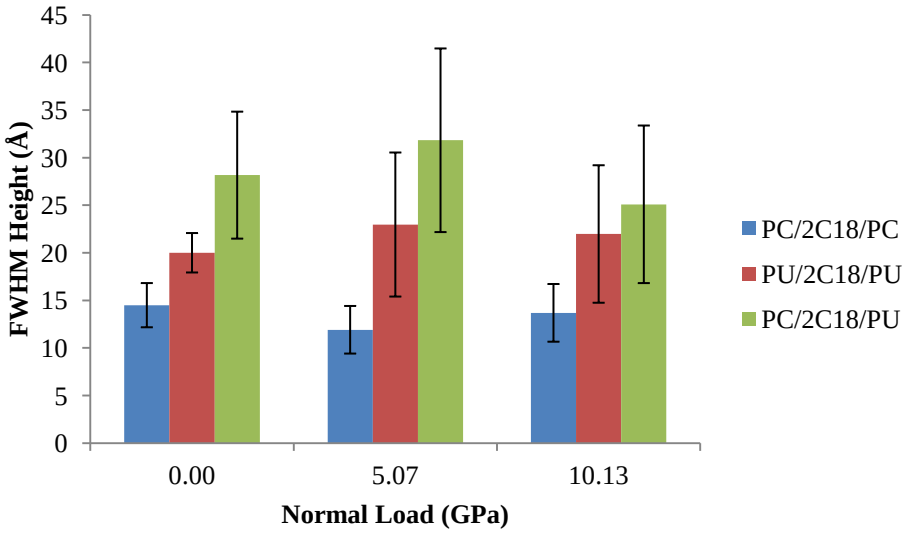

Figure 3.29. The FWHM of slip distribution as a height of the models with doubly lubricated interfaces. Error bars are available from the 4, 4 and 6 measurements at each normal load for the PC/2C18/PC, PU/2C18/PU and PC/2C18/PU models, respectively, except 2.5 and 7.5, for which there was only one measurement of each.

The absolute FWHM heights of the slip distribution suggests that the volume of material involved in the slip process is noticeably greater for the doubly lubricated PC/2C18/PU models than the doubly lubricated PC/2C18/PC and PU/2C18/PU models, which is not anticipated, as

the PC components do not contribute significantly to the deformation and increase in order parameter (refer to Section 3.4.3). Both of the slip distribution plots for the doubly lubricated models are similar to those of the singly lubricated models. Despite this, it will be seen in the next section that there is a shift in wear mechanism between the two levels of lubrication, when the original slip distribution plots (from which the FWHM values were extracted) will be compared to material distribution plots to get a sense of where in the models the slip is occurring, and how this plays a role in the values of slip distribution that are observed here.

Chapter 4: Discussion

The results presented in Chapter 3 shed light on quantitative details regarding the strengths and structures of the various models considered in the simulations. In this chapter, these results are examined and compared to develop slip mechanisms for these systems, to gain insight into the role of the lubricant, and to shed light on how the mechanical properties of the materials in contact affect the slip mechanism. The shear strengths of each interface at all levels of lubrication are compared in Section 4.1. An analogous comparison of the friction coefficients is provided in Section 4.2. Section 4.3 provides a detailed analysis of the position within the cell at which slip occurs, the alignment of the material in the cell with the slip direction and the composition of the cell. This analysis will provide the basis for determining the slip mechanisms for these interfaces. These slip mechanisms are then described in detail in Section 4.4.

4.1 Comparison of Shear Strengths

The average shear strengths obtained at different normal loads for each level of lubrication (dry, singly lubricated, and doubly lubricated) are given in Figure 4.1 for the PC/PC, PU/PU and PC/PU interfaces. In all plots, the symbols designate values of the shear strength obtained by averaging over the results of all simulations performed with that interface, level of lubrication, and normal load. The errors indicated in the plot represent one standard deviation. Comparing the shear strengths of the same type of interface with different levels of lubrication facilitates an examination of the effects of the lubricant on the strength of the interface.

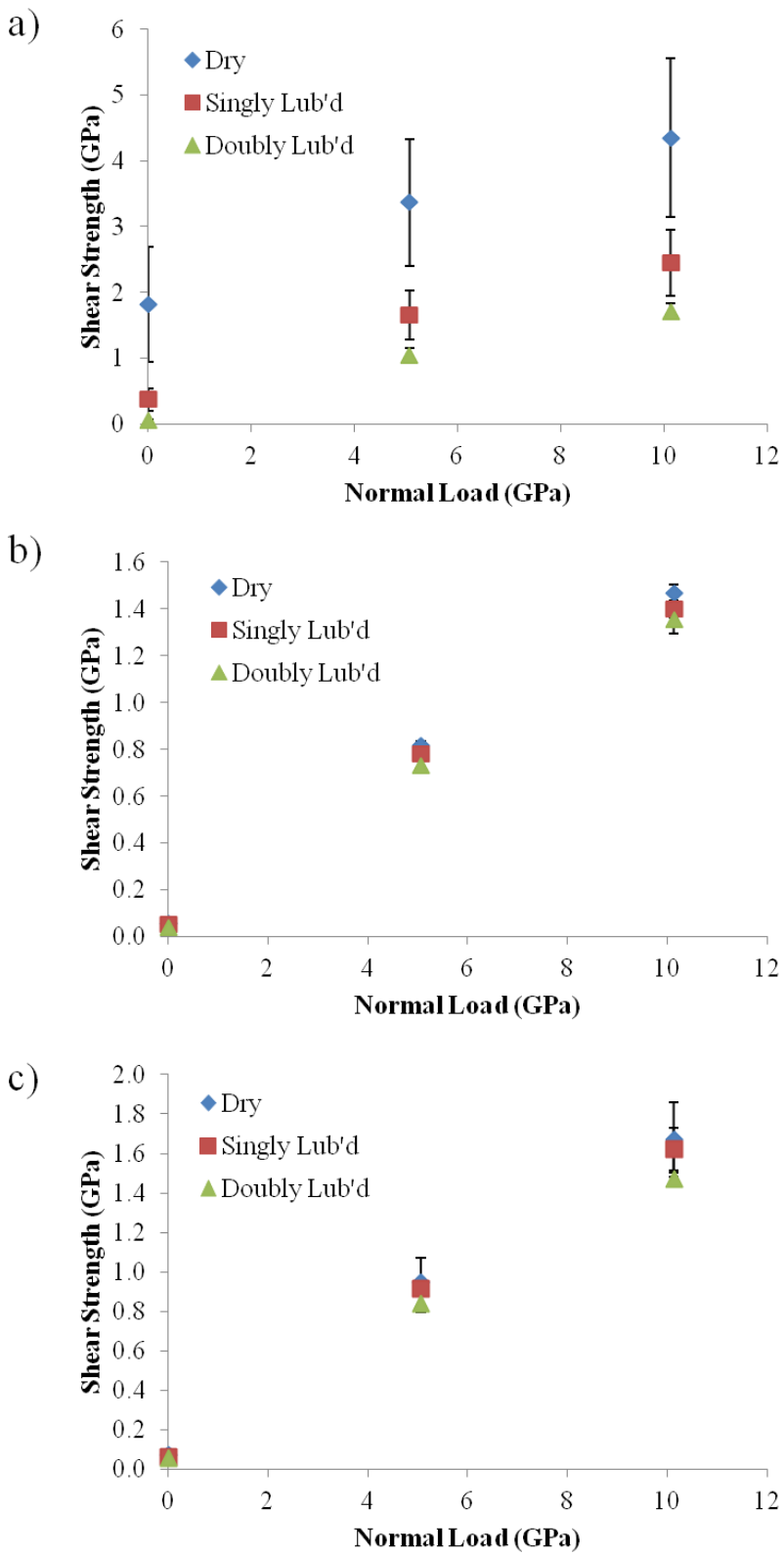

Figure 4.1. a) PC/PC models with a dry, singly lubricated, or doubly lubricated interface. Standard deviation error bars are included for the 16, 4 and 4 simulations, respectively. b) PU/PU models with a dry, singly lubricated, or doubly lubricated interface. Standard deviation error bars are included for the 16, 4 and 4 simulations, respectively. c) PC/PU

models with a dry, singly lubricated, or doubly lubricated interface. Error bars represent one standard deviation of the shear strengths obtained in the 24, 6, and 6 simulations, respectively.

The data in Figure 4.1a show that lubrication dramatically reduces the shear strength of the PC/PC interface. Specifically, moving from the dry interface to the singly lubricated model reduces the shear strengths by 1.4 to 1.9 GPa for the normal loads considered. The introduction of additional lubricant molecules leads to a further reduction in shear strengths at all loads. Meanwhile, the data in Figures 4.1b and 4.1c indicate that adding lubricant to the PU/PU and PC/PU interfaces has little effect on the shear strength. This is true in the absence of a normal load because the strengths of the dry PU/PU and PC/PU interfaces were already low. Meanwhile, the minimal effect of the lubricant at higher loads indicates that C18 is not particularly effective at reducing the friction forces associated with interfaces containing a PU component. The origin of this behaviour is examined in later sections of this chapter.

4.2 Comparison of Friction Coefficients

The friction coefficients for each interface with different levels of lubrication are provided in Table 4.1. The data illustrate that the friction coefficients for systems containing PU are consistently lower than those of systems containing only PC at the same level of lubrication. The data also show that the friction coefficient decreases as the amount of lubricant is increased. This effect is most pronounced for the PC/PC model, with the friction coefficient decreasing from 0.249 to 0.163 upon moving from the dry to doubly lubricated interface. The reduction in the friction coefficients with lubrication is less evident for the PU/PU and PC/PU interfaces, with the changes in the friction coefficients being in the second or third decimal place. The reduced effect of lubrication on the friction coefficients of interfaces containing PU is consistent with the minimal effect of the lubricant on the shear strengths of these interfaces.

Table 4.1. Coefficients of friction for the PC/PC, PU/PU. and PC/PU interfacial models with different levels of lubrication. The errors represent one standard deviation of the average friction coefficients for the 4, 4, and 6 models of the PC/PC, PU/PU and PC/PU systems, respectively.

	Dry	*Singly Lubricated*	*Doubly Lubricated*
PC/PC	0.249 ± 0.054	0.205 ± 0.034	0.163 ± 0.012
PU/PU	0.139 ± 0.004	0.133 ± 0.003	0.130 ± 0.006
PC/PU	0.158 ± 0.019	0.154 ± 0.010	0.139 ± 0.003

4.3 Comparison of Distribution Plots

The data in Chapter 3 provide insights into the structural changes associated with the slip process. In this section, these data are analyzed in detail for each interface to arrive at a description of the slip mechanism for the different systems considered in this study. This analysis was performed in the following manner. The structure of the system used to evaluate the FWHM reported in Chapter 3 was obtained. This corresponds to a structure slightly after slip occurred in all cases. The cell was divided into 10 equal fractions along the *z* direction, and the order parameter distribution (OPD), slip distribution (SD) and component distribution (CD) were calculated within each of these height fractions as described in Sections 2.7.3 through 2.7.5, respectively. A fraction distribution (FD) corresponding to the amount of a given component in a height fraction relative to the total amount of material in the same height fraction was also evaluated for systems containing more than one component.

In the context of elucidating slip mechanisms, it is important to recall the following features of the SD, OPD, CD and FD plots. The SD provides insight into how far the system has moved in a given fraction along *z* relative to neighbouring fractions over a particular time step. This quantity is useful in determining the position(s) along *z* at which slipped occurred. The OPD provides insight into the extent the material has aligned with the slip direction. The CD plot indicates the percentage of the total amount of a given component that is present in each fraction. Integrating one CD curve over one full cell height yields 100%. The FD plot indicates how much

each component in the system contributes to the total amount of material in a given fraction. It is effectively a normalization of the CD plot, such that the combined amount of material in each height fraction adds up to 100%. This is especially useful when there are multiple components that do not have equal amounts of material. This graph is not provided in models containing only one component, since the value would be 1 for all height fractions.

To help identify any correlations between the location of slip, alignment of the system and composition, the SD, OPD, and CD plots were stacked for each interface. The FD plot was also included in the stacked graphs when more than one component was present in the system. In all cases, the SD plot is at the top, the OPD plot is second from the top, the CD plot is at the bottom when only one component is present, or second from the bottom when two components are present with the FD plot on the bottom. These stacked graphs are included in Figures 4.2 through 4.13.

In all cases, the stacked plots have identical *x* axes corresponding to the fraction along the *z* axis. Since key characteristics are sometimes at the top or bottom of the cell, the plots are duplicated to show two repeated cells, such that the *x* axis reaches 200% or 20 fractions. Note that the scales along the *y* axes are not the same in plots for different systems. Within the CD and FD plots, colours for PC, PU and C18 will consistently be light blue, red, and green, respectively.

Plots are shown from simulations in which the PC4, PU4, and PC1/PU4 models were sheared along the *x* direction in the absence of a normal load. In most cases, analogous results were obtained for other models and at other normal loads. Cases where differences in the plotted properties, or correlations between them, were observed are noted as appropriate. These differences were most commonly observed for the mixed PC/PU models.

4.3.1 Bulk Materials

As described in Chapter 3, simulations were performed in which models of bulk PC, PU and C18 were sheared. The SD, OPD, and CD plots corresponding to these systems are examined in this section. The plots for the bulk PC, PU and C18 systems are contained in Figures 4.2 through 4.4.

PC

The distribution plots for the bulk PC model are shown in Figure 4.2. The CD plot indicates that each height fraction contains between 9 and 11 % of the total material, which is consistent with an even distribution of material throughout the system. The OPD suggests that the entire system reorganizes when slip occurs, with this parameter exhibiting a relatively narrow range of values (between 0.26 and 0.40) for all height fractions. The SD plot exhibits a distinct peak in the 8^{th} height fraction with a relatively narrow width, which corresponds to the position at which slip occurred. This peak is aligned with a local minimum in the CD plot, which suggests that slip occurs at a point where the density of the system is low. However, one should keep in mind the variations in the density across different height fractions are relatively small.

PU

The distribution plots for the bulk PU model are shown in Figure 4.3. The CD ranges again from 9 to 11% for each of the 10 height fractions. The OPD values range from 0.3 to 0.5, indicating that the entire material undergoes a large degree of alignment toward the slip direction. There is a distinct peak in the SD, which aligns closely with the maximum in the CD plot. In contrast to bulk PC, this indicates that bulk PU undergoes slip at a point where the density is highest. Once again, it is important to keep in mind the fact that the density is similar

across all fractions before drawing any inferences regarding the relationship between slip location and local density.

C18

The distribution plots for the bulk C18 model are shown in Figure 4.4. The CD varies between approximately 8 and 12%, which corresponds to a greater variation in the local material density than was observed for the bulk PC and PU systems. The OPD plot includes negative values, which corresponds to some of the bonds in the material aligning more closely to the *y* or *z* directions than along the slip direction. The CD plot resembles a layered structure, which was developed in the course of shearing. The SD shows two peaks, one taller and broader than the other, which both correlate to minima in the CD. Neither of these slip regions correspond to the peak in the OPD, which suggests that ordering does not occur in the slip mechanism of the bulk C18 model.

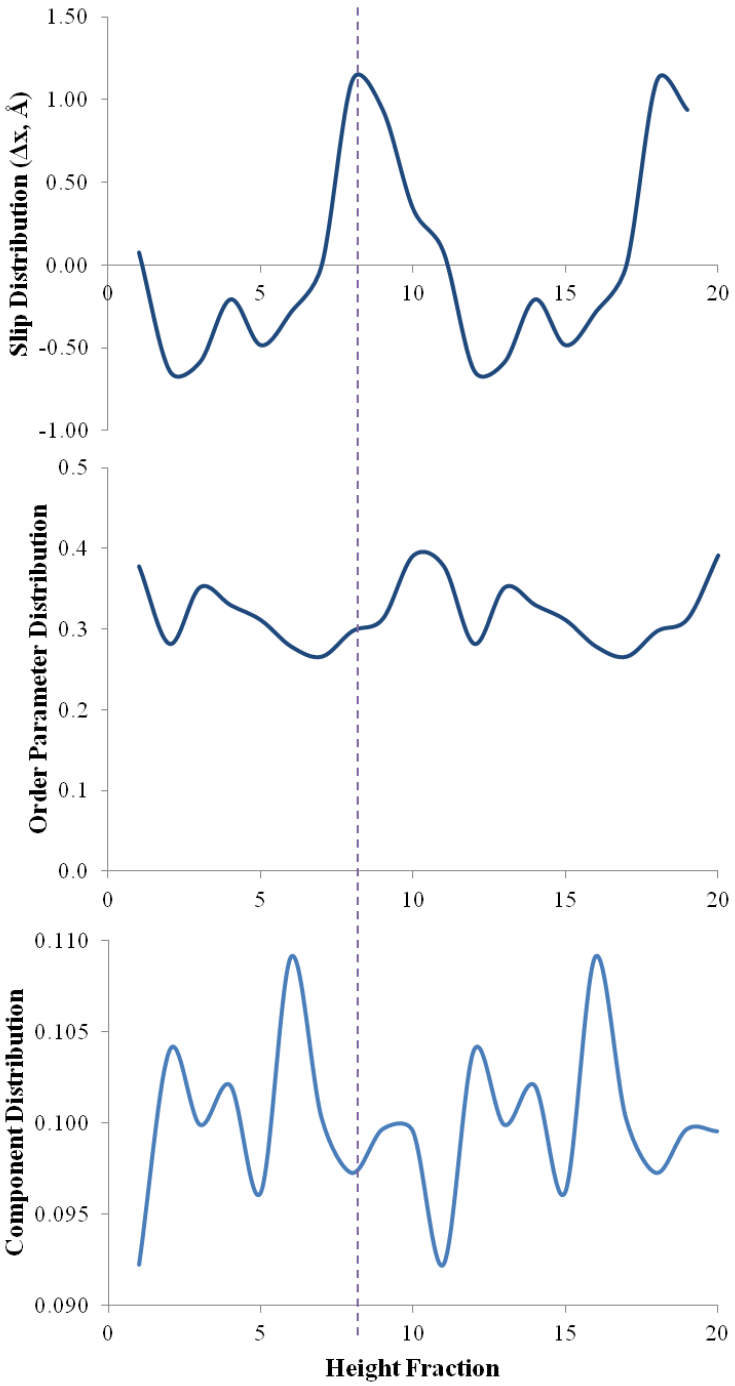

Figure 4.2. Distribution plots for the bulk PC model. The model was sheared in the *x* direction with zero normal load. The plots have been repeated twice along the *x* axis, representing a duplication of the simulation cell, to better illustrate features that occur near the top and/or bottom of the cell.

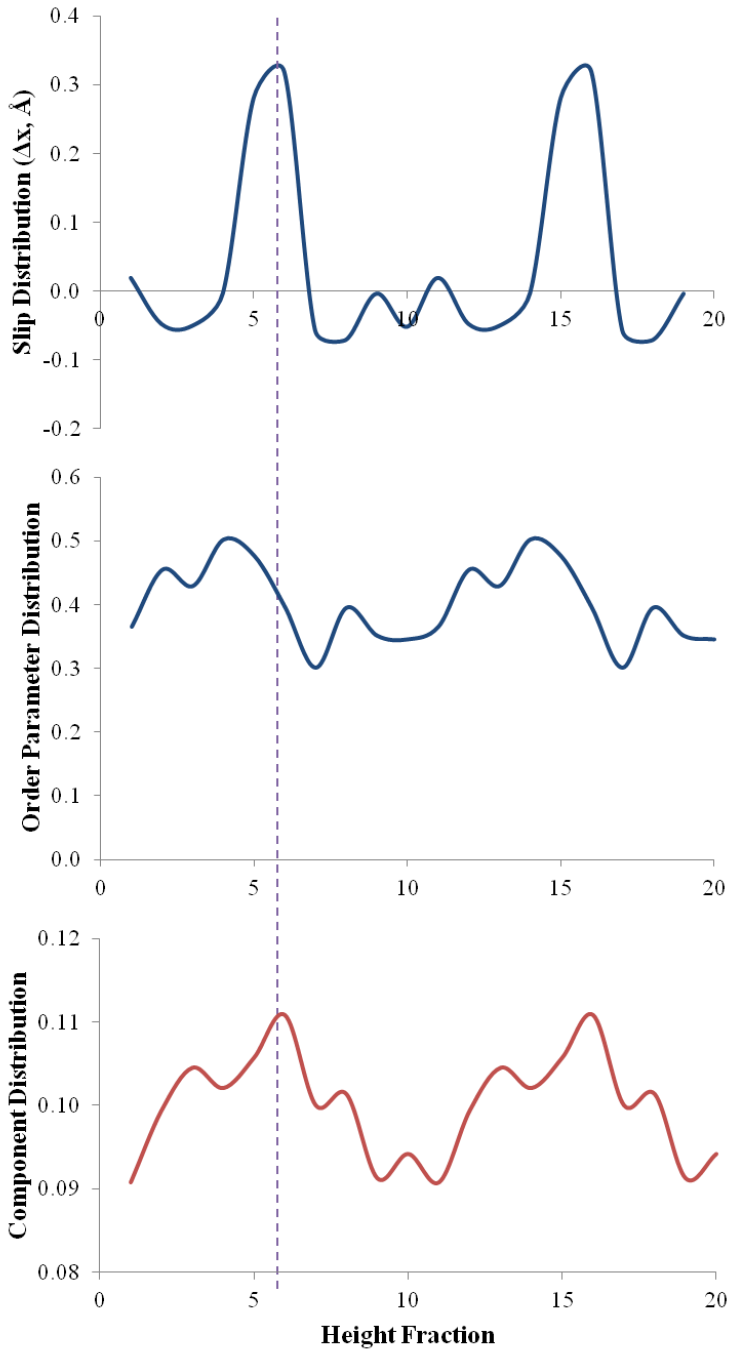

Figure 4.3. Distribution plots for the bulk PU model. The model was sheared in the *x* direction with zero normal load. The plots have been repeated twice along the *x* axis, representing a duplication of the simulation cell, to better illustrate features that occur near the top and/or bottom of the cell.

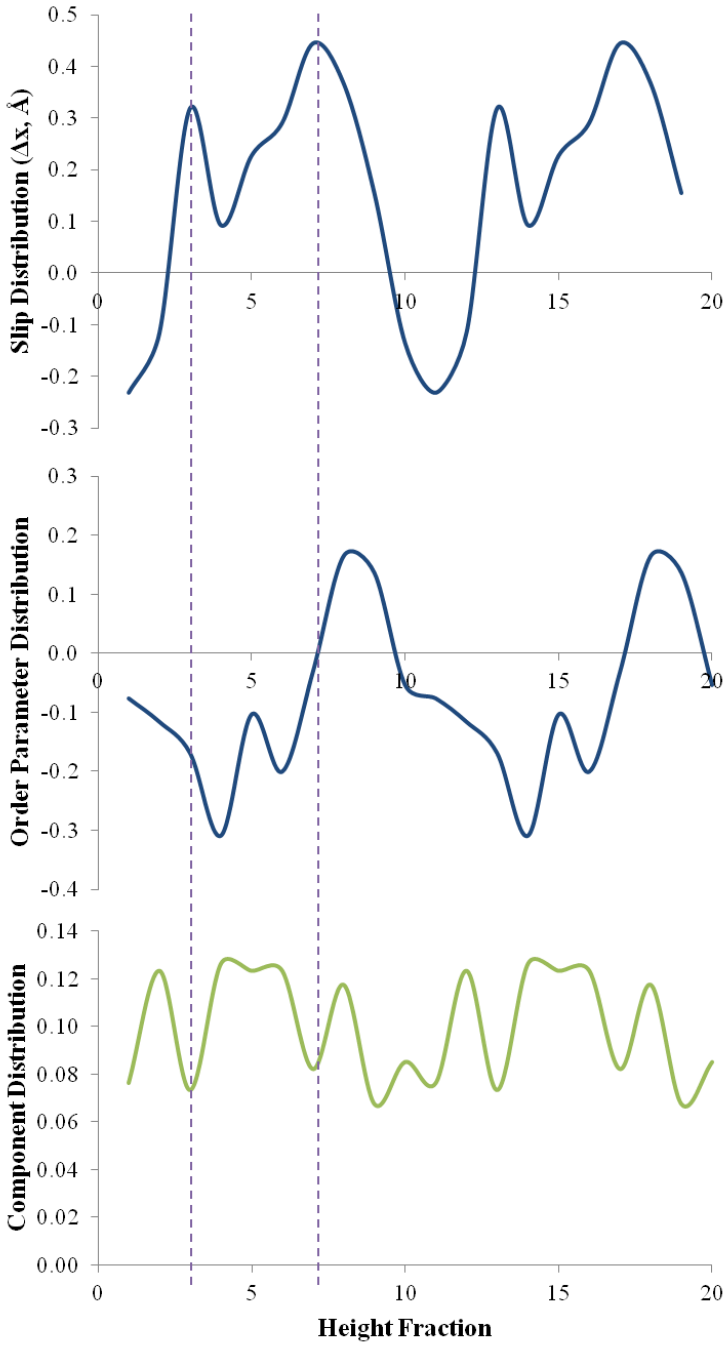

Figure 4.4. Distribution plots for the bulk C18 model. The model was sheared in the *x* direction with zero normal load. The plots have been repeated twice along the *x* axis, representing a duplication of the simulation cell, to better illustrate features that occur near the top and/or bottom of the cell.

4.3.2 Dry Interfacial Systems

The SDs, OPDs, and CDs were calculated for the various interfaces considered in this work. The FD was also calculated for the PC/PU interface to better illustrate the distribution of the individual components in the system. These plots are shown and discussed in what follows. The plots for the PC/PC, PU/PU, and PC/PU interfaces are provided in Figures 4.5 through 4.7.

PC/PC

The distribution plots for the dry interfacial PC/PC model are shown in Figure 4.5. The CD ranges from 8 to 12%, and the minimum in height fraction 12 in this plot likely corresponds to the position of the interface that was initially placed between the two PC slabs. Note that due to entanglement between the polymers on the surfaces of these slabs, the interface is not clearly defined, yet is rather associated with a region of lower density. There is a sharp peak in the SD plot that corresponds to the position at which slip occurred and correlates well with the position of the minimum in the CD plot. Meanwhile, very little alignment of the material with the slip direction is evident in any of the height fractions in the OPD plot. Overall, this indicates that slip in the PC/PC interface involves the two PC slabs moving past each other at the interface with very little change in the structure of either slab.

PU/PU

The distribution plots for the dry interfacial PU/PU model are shown in Figure 4.6. The CD is approximately 0.1 for all 10 height fractions, suggesting a relatively even density distribution. As a result, it is difficult to identify the interface that had been introduced during the construction of this model. Rather, the polymers on either side of the interface have mixed with each other. A clear maximum in the SD plot is evident, with a small shoulder in the peak. The OPD plot exhibits clear peaks indicating that a significant alignment of the bonds in the

polymers with the slip direction occurs in localized regions of the material. The positions of the peaks in the SD and OPD plots correlate well with each other. Overall, this indicates that localized alignment of the polymers is associated with slip in the dry PU/PU interface.

PC/PU

The distribution plots for the dry interfacial PC/PU model are shown in Figure 4.7. There is more than one component in the models, and as such the FD is provided in addition to the SD, OPD and CD plots. The points at which the curves for the compositions of the PU and PC components cross in the CD and FD plots indicate the locations of the interfaces between these materials. These interfaces are located around the 4^{th} and 10^{th}-11^{th} height fractions. Two interfaces are present because one interface was purposely introduced into the middle of the cell, whereas a second interface between these materials was introduced as a result of applying periodic boundary conditions along the *z* axis. It is noted that this additional interface would not be present in the real system. In addition, regions that are entirely PC or entirely PU can be identified.

Well defined maxima are present in the SD and OPD plots. The bands associated with these peaks are contained primarily in the PU portion of the system and do not extend across the interface. This indicates that slip occurs within the PU component as opposed to taking place at the interface between these components. A few of the dry PC/PU models exhibited slip motion in the interface region, but rarely without a second slip region either at the second unique interface or within the PU component. This may be due to the significant differences in the strengths of the PU and PC components, with PU being much weaker, as evidenced by the shear strengths of the bulk materials. Specifically, slip is unlikely to occur within the PC component because that material has a high shear strength. The entanglement of PC polymers with PU polymers across

the interface may strengthen the interface compared to the shear strength of the pure PU component, causing slip to occur in the PU component.

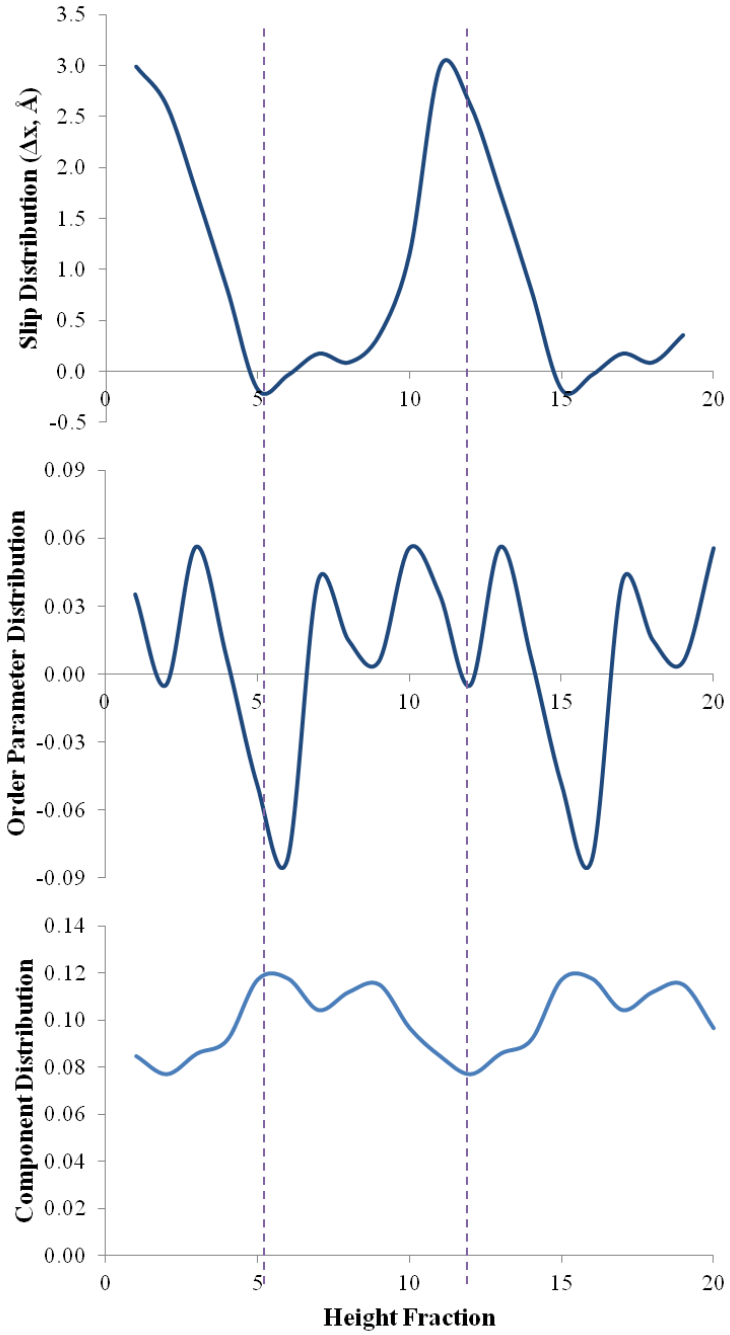

Figure 4.5. Distribution plots for the dry PC/PC interface model. This is PC4, sheared in the *x* direction with zero normal load. The plots have been repeated twice along the *x* axis, representing a duplication of the simulation cell, to better illustrate features that occur near the top and/or bottom of the cell.

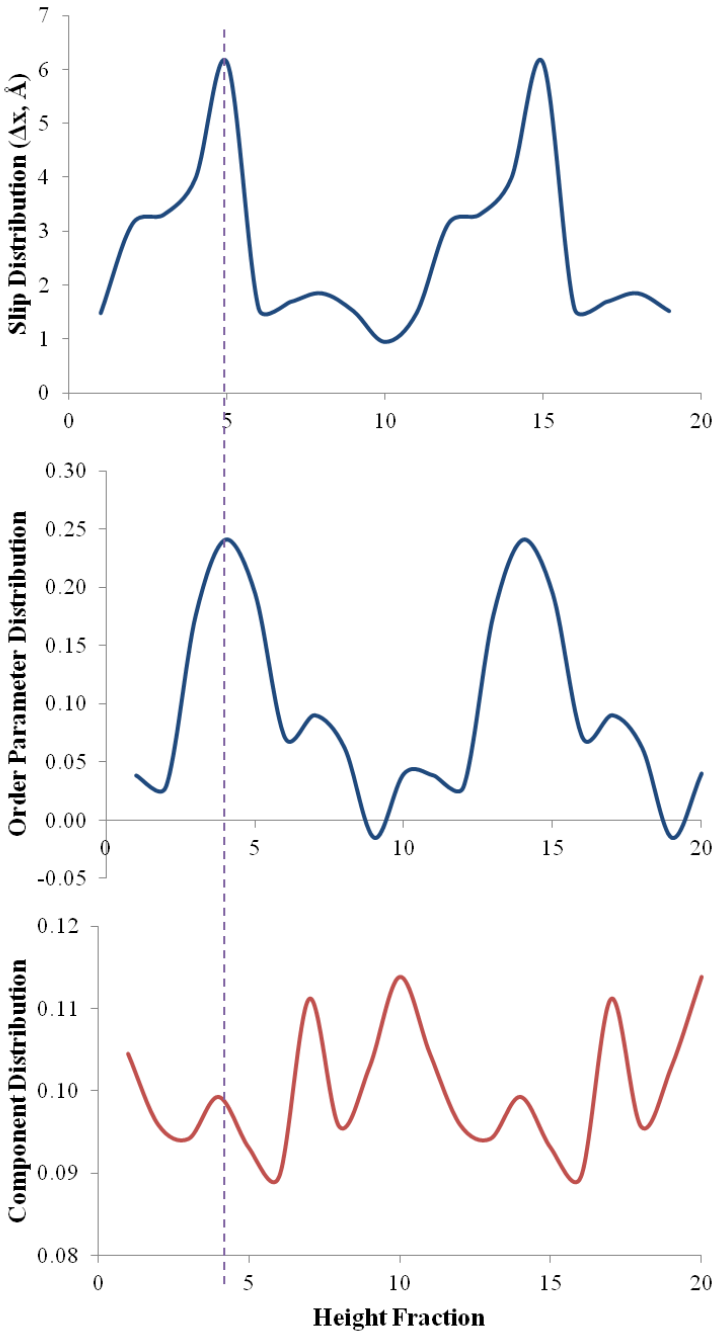

Figure 4.6. Distribution plots for the dry PU/PU interface model. This is PU4, sheared in the *x* direction with zero normal load. The plots have been repeated twice along the *x* axis, representing a duplication of the simulation cell, to better illustrate features that occur near the top and/or bottom of the cell.

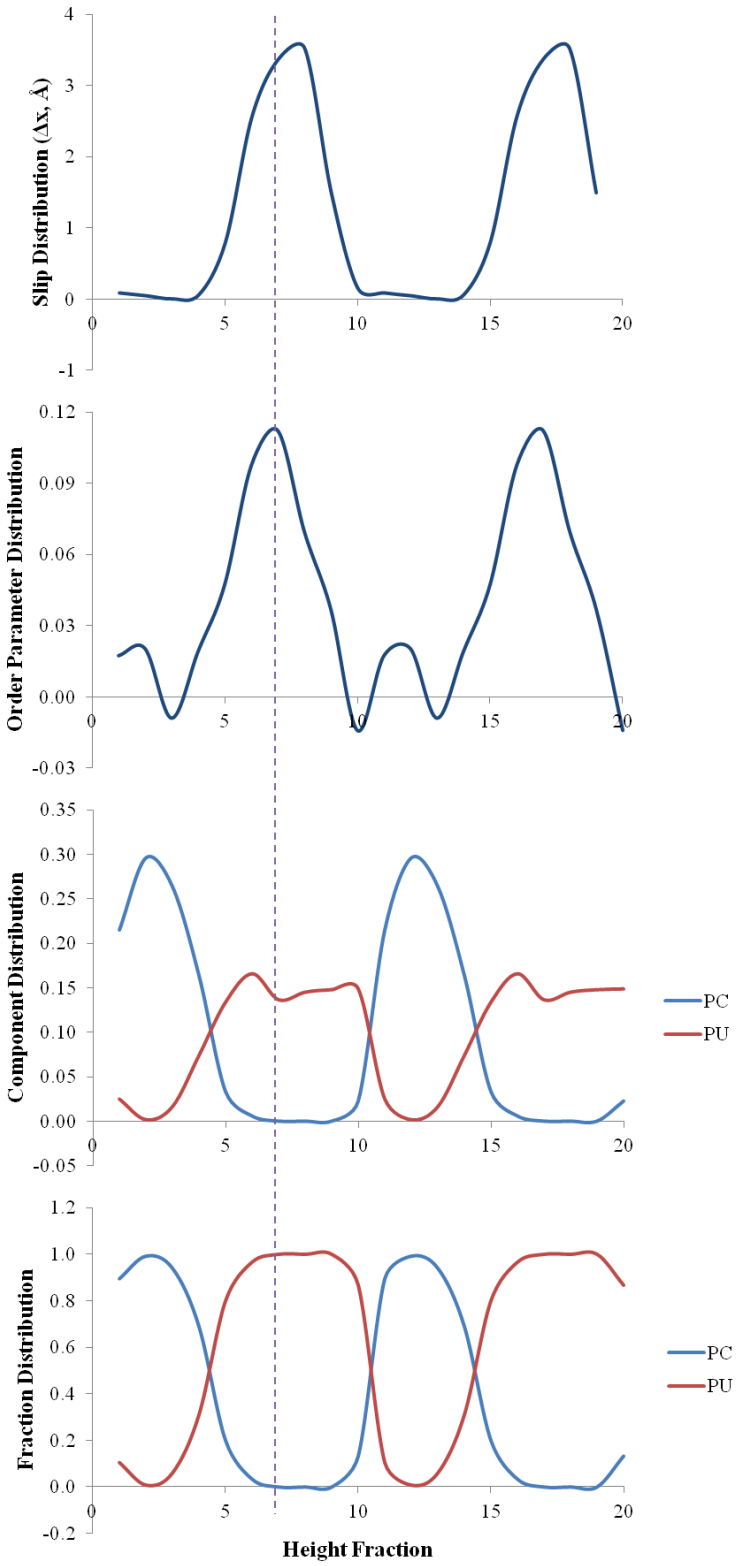

Figure 4.7. Distribution plots for the dry PC/PU interface model. This is PC1/PU4, sheared in the *x* direction with zero normal load. The plots have been repeated twice along the *x* axis, representing a duplication of the simulation cell, to better illustrate features that occur near the top and/or bottom of the cell.

4.3.3 Lubricated Systems (2 Molecular Layers)

The SDs, OPDs, CDs, and FDs were calculated for the various interfaces lubricated with two molecular layers of C18. These plots are shown and discussed in what follows. The plots for the PC/C18/PC, PU/C18/PU, and PC/C18/PU interfaces are provided in Figures 4.8 through 4.10.

PC/C18/PC

The distribution plots for the singly lubricated interfacial PC/C18/PC model are shown in Figure 4.8. The CD and FD plots show the locations of the PC and C18 components. The data demonstrate that a well-defined interface does not exist, with the PC fraction in the FD plots being greater than 0.5 for height fractions. The data also illustrate that the C18 lubricant occupies a relatively localized region in the system. As a whole, this suggests the C18 lubricant has mixed with the PC components in the area of the interface that was introduced when constructing the model.

There is a well-defined peak in the SD plot. This peak is aligned closely with the peak associated with C18 in the CD and FD plots, which indicates that slip occurs at the region with the highest amount of the lubricant. The OPD plot indicates very little of the bonds aligning with the slip direction, with all values in this plot residing between approximately -0.03 and 0.06. Overall, this suggests that slip in the PC/C18/PC models occurs in a localized region around the point at which the lubricant was introduced with very little change in the structure of the system.

PU/C18/PU

The distribution plots for the singly lubricated interfacial PU/C18/PU model are shown in Figure 4.9. The CD and FD plots indicate that the C18 lubricant resides in a relatively localized region of the model, whereas significant amounts of PU are present throughout the cell. There

are clear regions composed entirely of PU, which correspond to the PU slabs. Meanwhile, PU maintains values of at least 0.4 in the FD plot in the region where the C18 lubricant exists. This region corresponds to the point where the interface was introduced when constructing this model, yet these results indicate that a well-defined interface is no longer present in the system.

There is a well-defined peak in the SD plot that is aligned with the position that contains most of the C18 lubricant. Several peaks are present in the OPD plot. These peaks reach values greater than those observed in the PC/C18/PC system, yet are lower than those reached during slip in the dry PU/PU interface. This suggests that an intermediate amount of alignment between the bonds in the system and the slip direction occurs for this interface. One of the peaks in the OPD plot is aligned with the position at which slip occurs and at which the presence of C18 is a maximum, indicating that slip involves the alignment of the lubricant with the slip direction. The presence of a second peak in the OPD plot within a region composed entirely of PU suggests that the structure of this material is also affected by slip. This suggests that the bulk of the PU slab is not protected from the effects of shear, even with two molecular layers of lubricant.

PC/C18/PU

The distribution plots for the singly lubricated interfacial PC/C18/PU model are shown in Figure 4.10. The CD and FD plots indicate the presence of one slab composed of PC and another composed of PU that are separated by two types of interfaces. One interface contains the C18 lubricant and was introduced during the construction of the model. The second interface does not contain the lubricant and arises from the application of periodic boundary conditions along the *z* direction. Mixing of the materials is evident across both interfaces.

The SD plots exhibit two distinct peaks. A large peak is present within the PU slab at a position near where the PC component begins to contribute to the FD at the interface that does

not contain lubricant. This indicates that the majority of slip occurs near this interface, which is only present due to the application of periodic boundary conditions and would not be found in the real system. A smaller peak in the SD plot is aligned with the height fraction containing the lubricant, indicating that some slip occurs at this point. Large peaks in the OPD plot exist in the height fractions associated with the interface introduced via periodic boundary conditions. Overall, these results indicate that slip involves the reorganization of the PU material and occurs within the PU slab. The minimal amount of slip occurring at exactly either interface may be due to the mixing of PU and PC components across these interfaces, which may increase the strengths of the material at these locations, which led to slip within the weaker PU component. Though these plots show slip at the lubricated interface as well as within the PU component, half of the singly lubricated PC/C18/PU models still only exhibit slip within the PU component during slip in the absence of a normal load. This behaviour is analogous to that observed for the dry PC/PU example examined above.

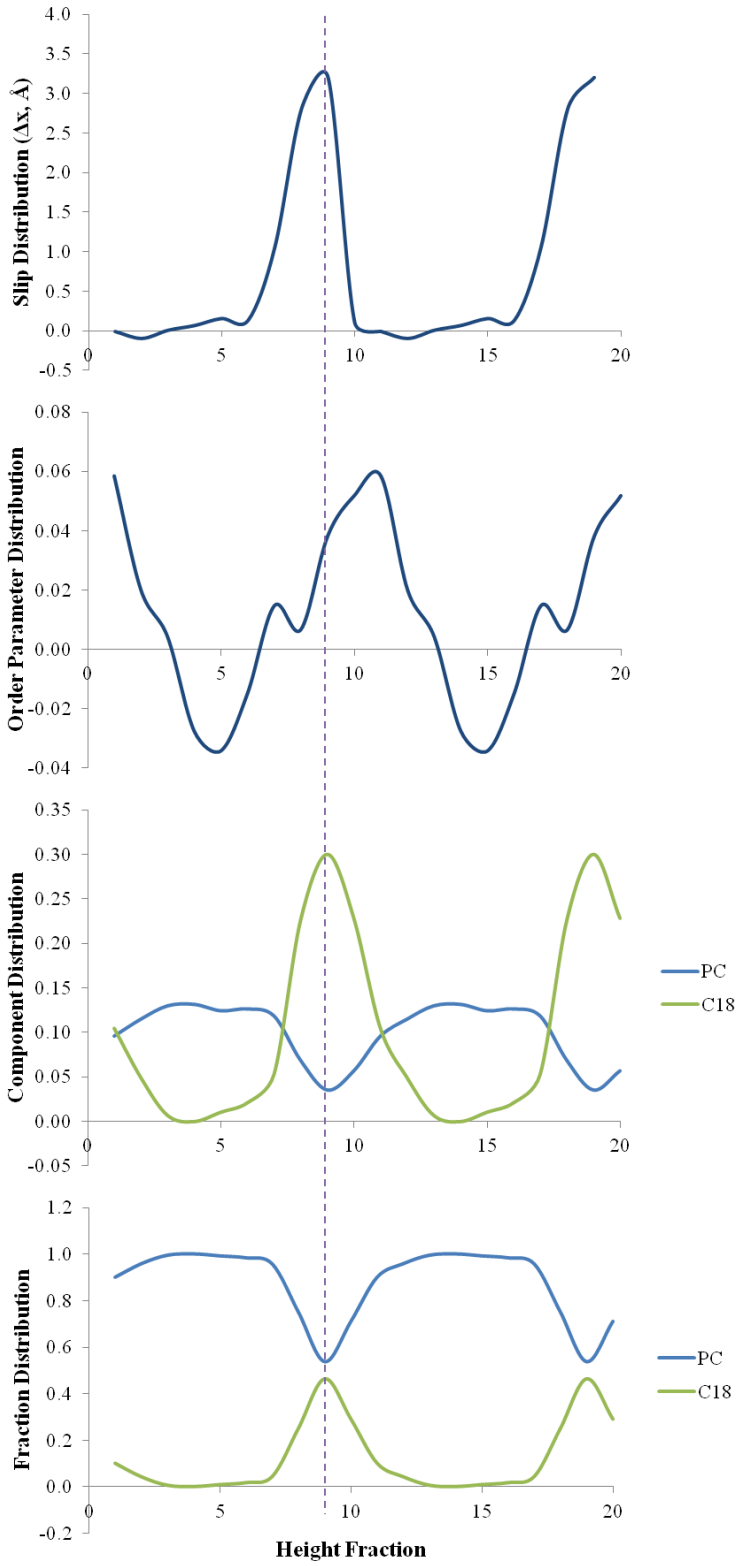

Figure 4.8. Distribution plots for the singly lubricated PC/C18/PC interface model. This is PC4, sheared in the *x* direction with zero normal load. The plots have been repeated twice along the *x* axis, representing a duplication of the simulation cell, to better illustrate features that occur near the top and/or bottom of the cell.

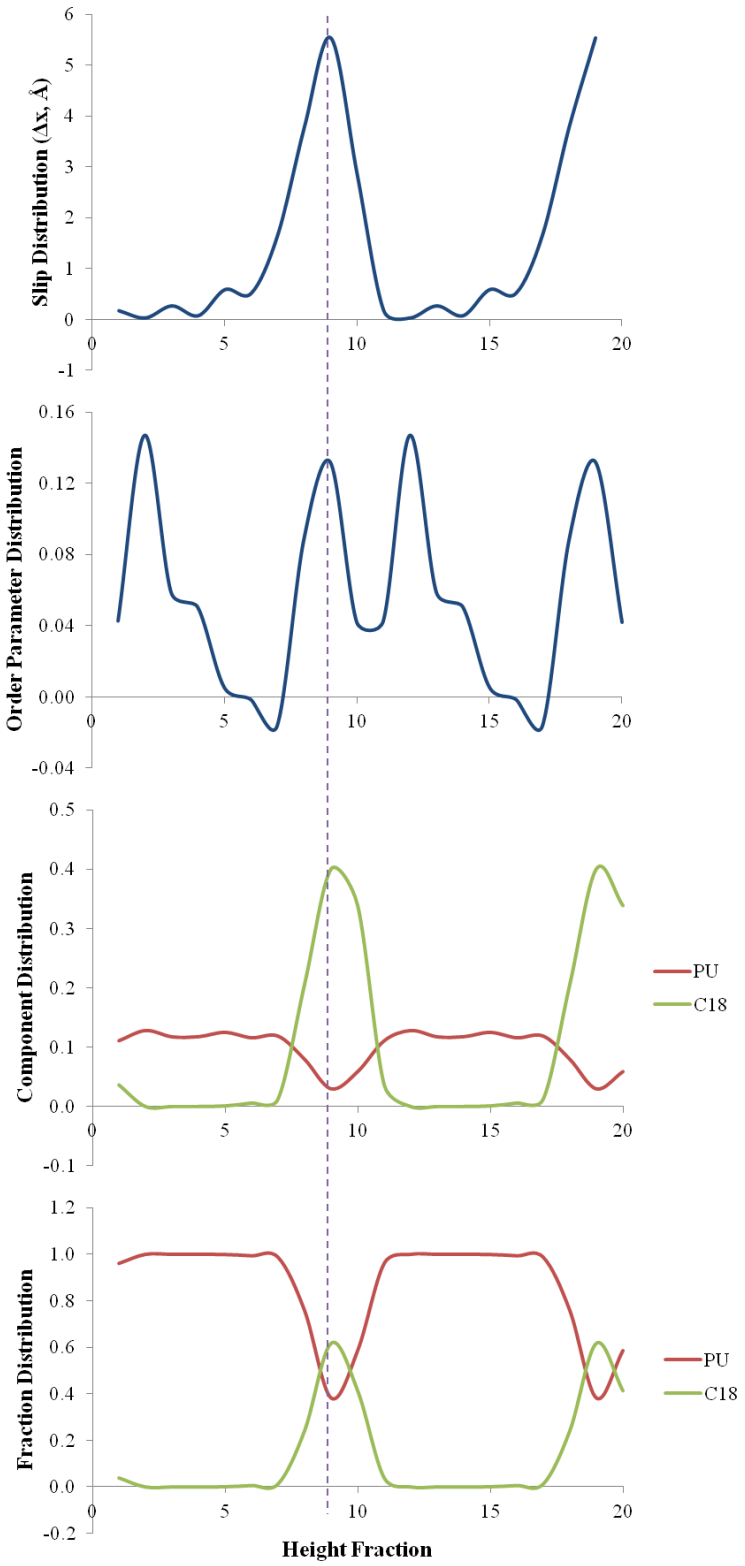

Figure 4.9. Distribution plots for the singly lubricated PU/C18/PU interface model. This is PU4, sheared in the *x* direction with zero normal load. The plots have been repeated twice along the *x* axis, representing a duplication of the simulation cell, to better illustrate features that occur near the top and/or bottom of the cell.

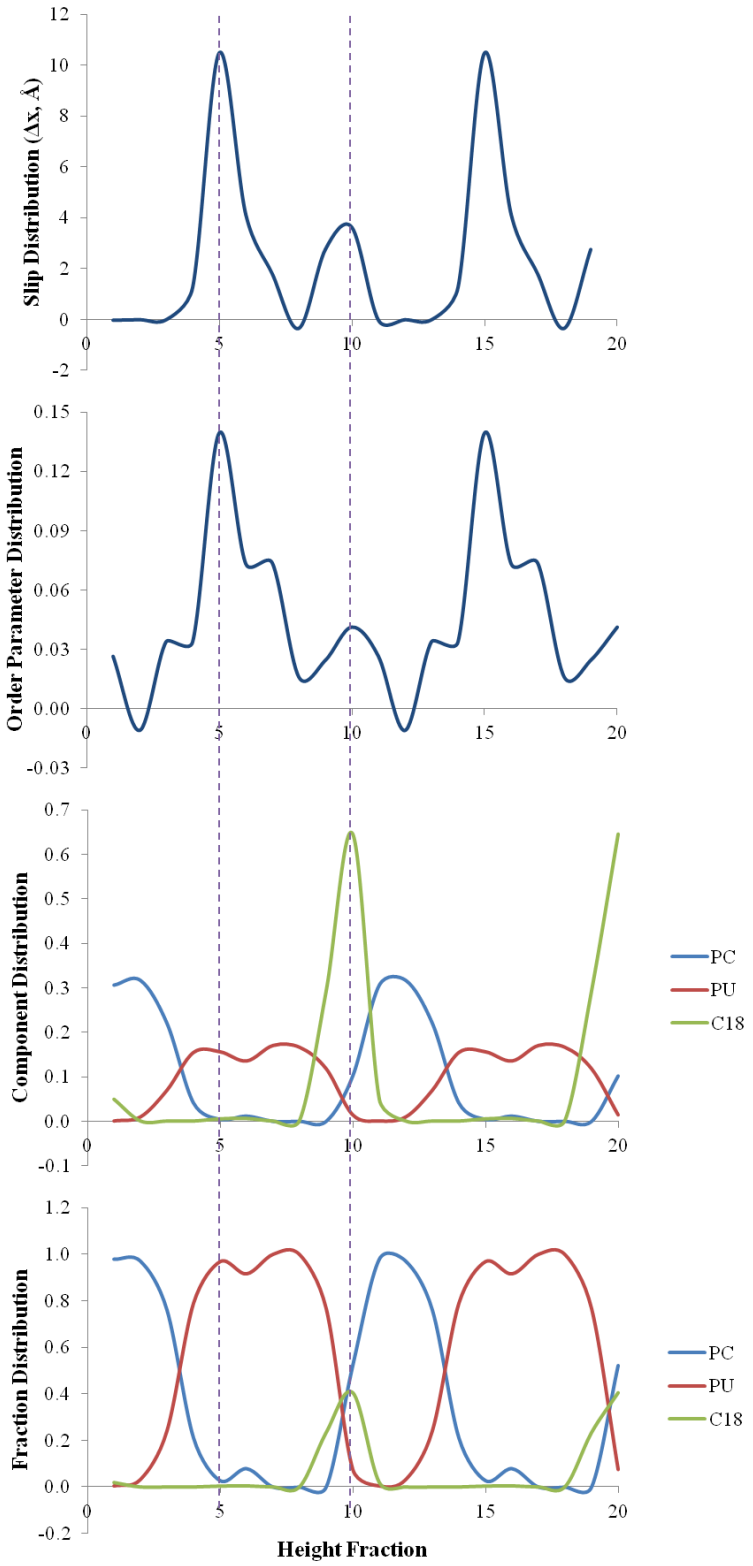

Figure 4.10. Distribution plots for the singly lubricated PC/C18/PU interface model. This is PC1/C18/PU4, sheared in the *x* direction with zero normal load. The plots have been repeated twice along the *x* axis, representing a duplication of the simulation cell, to better illustrate features that occur near the top and/or bottom of the cell.

4.3.4 Lubricated Systems (4 Molecular Layers)

The SDs, OPDs, CDs, and FDs were calculated for the various interfaces lubricated with four molecular layers of C18. These plots are shown and discussed in what follows. The plots for the PC/2C18/PC, PU/2C18/PU, and PC/2C18/PU interfaces are provided in Figures 4.11 through 4.13.

PC/2C18/PC

The distribution plots for the doubly lubricated interfacial PC/2C18/PC model are shown in Figure 4.11. The CD and FD show the distribution of the PC and C18 components. The C18 maximum lies at the PC minimum, and is able to reach an FD value of about 90%, suggesting the presence of relatively well-defined interface, with minimal interaction between the two PC slabs. There is a single well-defined peak in the SD plot that is aligned with one side of the PC/C18 interface. There is also a clear peak in the OPD plot that aligns with the C18 component. This suggests that slip occurs via an alignment of the C18 molecules along the slip direction, which allows the PC slab on one side of the interface to move relative to the remainder of the system.

PU/2C18/PU

The distribution plots for the doubly lubricated interfacial PU/2C18/PU model are shown in Figure 4.12. The CD and FD plots show the distribution of the PU and C18 components. The C18 maximum lies at the PU minimum, and reaches an FD value of about 90%, suggesting that the two PU surfaces now have minimal interaction with each other. A single well-defined peak exists in the SD plot and is aligned with the C18 lubricant. The OPD exhibits two peaks. One is aligned with that in the SD plot, whereas the second, smaller peak corresponds with a region just inside the PU slab. Overall, these results suggest that slip occurs through a process in which the C18 molecules align with the slip direction and move past each other. However, despite slip

occurring within the lubricant portion of the system, structural changes do still occur within the PU slab.

PC/2C18/PU

The distribution plots for the doubly lubricated interfacial PC/2C18/PU model are shown in Figure 4.13. The CD and FD plots show the distribution of all three components in this model. These plots indicate the presence of distinct PU and PC slabs that are separated by two interfaces. The first interface contains the C18 lubricant, which is apparently mixed significantly with both the PU and PC components except in the 9^{th} height fraction, where C18 adopts a value of approximately 0.9 in the FD plot. The second interface involves direct interactions between the PU and PC slabs, and is a result of the periodic boundary conditions used in the calculations. A clear peak is present in the SD plot and is aligned with the interface between the C18 and PU components. Two peaks exist in the OPD plot. The first is aligned with the C18 component, whereas the second lies within the PU component near the PU/PC interface. Overall, these data indicate that slip involves the alignment of the C18 molecules, but involves the movement of the PU slab past the C18 lubricant. Meanwhile, the peak in the OPD plot within the PU slab indicates that the structure of PU is affected by the slip process. At zero normal load, only two of the six models exhibited localized slip as shown in this example. Two others exhibited slip within the PU component (albeit to a lesser extent) as shown in the singly lubricated PC/C18/PU example, while the final two only slipped within the PU component, as shown in the dry PC/PU example. Complementing this trend, the C18 FD became less localized as the slip region moved to the PU component.

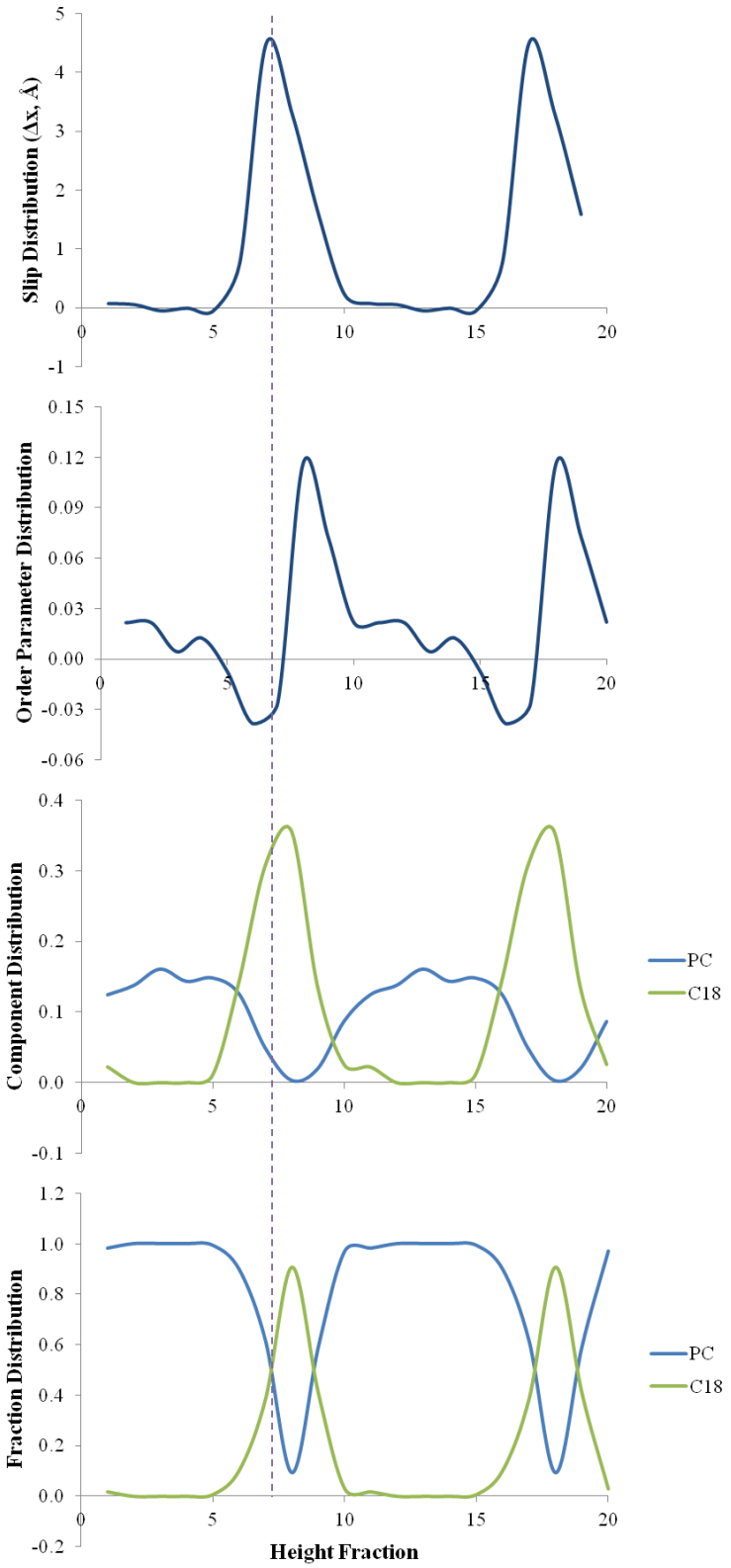

Figure 4.11. Distribution plots for the doubly lubricated PC/2C18/PC interface model. This is PC4, sheared in the *x* direction with zero normal load. The plots have been repeated twice along the *x* axis, representing a duplication of the simulation cell, to better illustrate features that occur near the top and/or bottom of the cell.

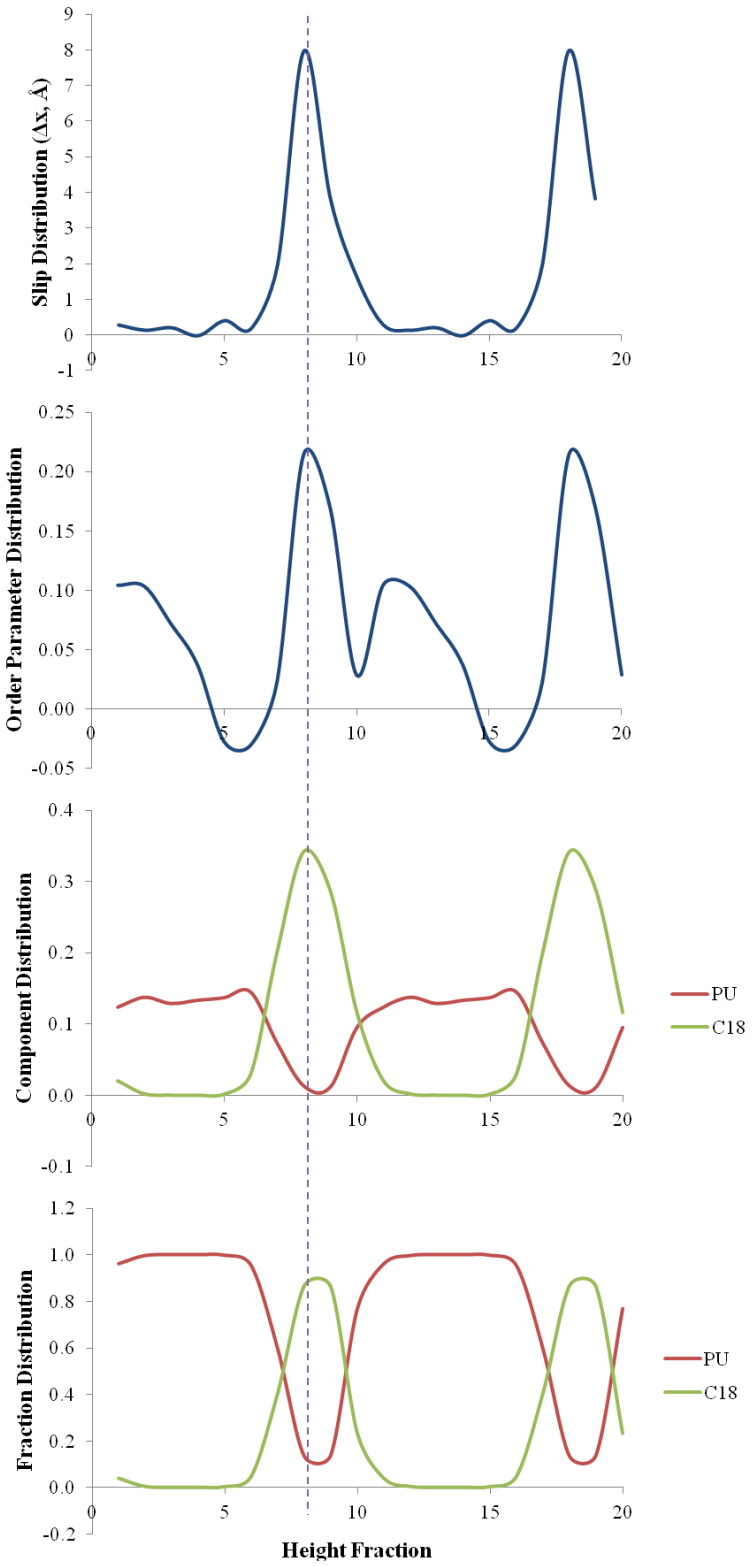

Figure 4.12. Distribution plots for the doubly lubricated PU/2C18/PU interface model. This is PC4, sheared in the *x* direction with zero normal load. The plots have been repeated twice along the *x* axis, representing a duplication of the simulation cell, to better illustrate features that occur near the top and/or bottom of the cell.

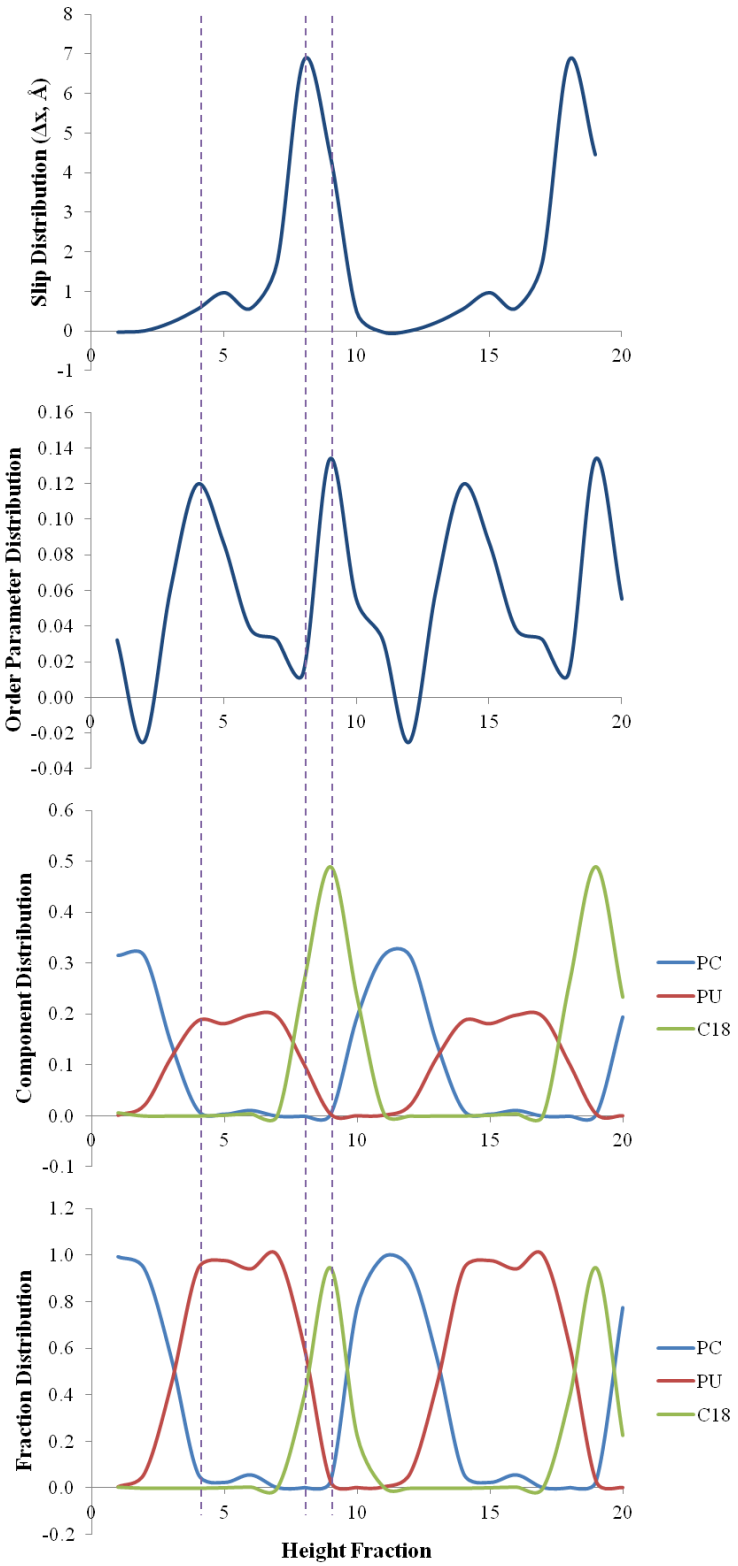

Figure 4.13. Distribution plots for the doubly lubricated PC/2C18/PU interface model. This is PC1/2C18/PU4, sheared in the *x* direction with zero normal load. The plots have been repeated twice along the *x* axis, representing a duplication of the simulation cell, to better illustrate features that occur near the top and/or bottom of the cell.

4.3.5 Slip Mechanisms, Friction and Wear

The analysis presented above sheds light on the correlations between locations, changes in structure and material composition associated with the slip processes for the models considered in this work. An examination of these details highlights three different slip mechanisms that are related to the composition of the interface. Qualitative illustrations of these mechanisms are given in Figure 4.14. These mechanisms and their relationships to lubrication and wear of the interfaces are discussed in what follows.

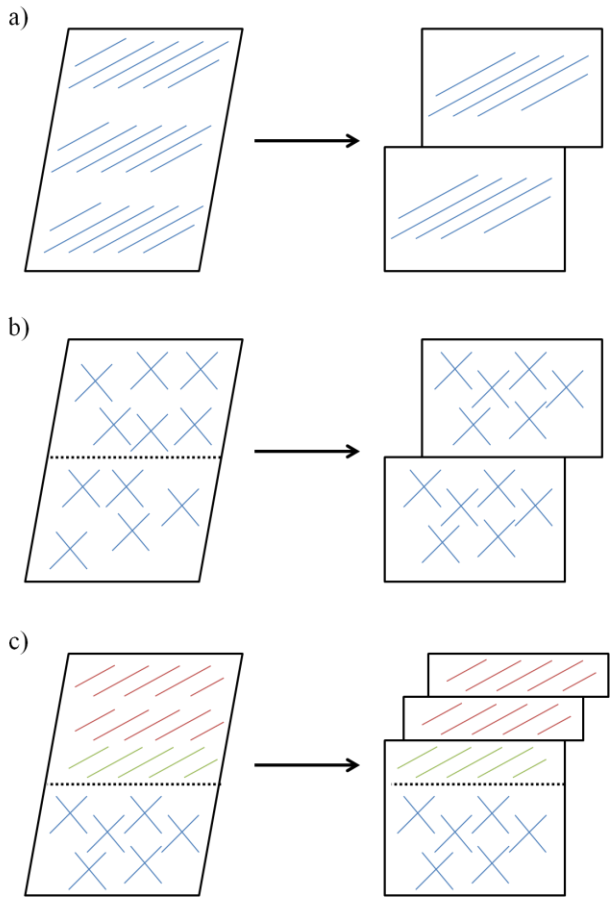

Figure 4.14. Schematics of the three general slip mechanisms, before and after slip. The dotted line is where an interface was intended. a) Bulk PC or bulk PU exhibit ordering and localized slip. b) Dry or lubricated interfacial PC exhibits no ordering in the PC component, as well as localized slip. The lubricant is not shown here. c) Any interfacial model containing PU. No orientation is shown in the lower PC component, though if no PC is present, the lower component should exhibit ordering as well. The red and green portions represent either PU and C18 respectively, or pure PU. They both exhibit ordering, and slip occurs within them. Slip is typically not localized.

The first slip mechanism (see Figure 4.14a) applies to the bulk PU and PC systems. In both of these systems, slip occurred at a localized position in the system yet alignment of the bonds with the slip direction was prevalent throughout the entire system. This behaviour is consistent with a slip process in which the material initially undergoes uniform shear, which leads to changes in structure throughout the entire material. These changes in structure are associated with alignment of the bonds along the shear direction. At some point, the shear stress exceeds the strength of the material and slip occurs. Slip occurs in a localized region within the material. The region in which slip occurs is not correlated with any fixed feature of the system, but is rather a dynamic feature that is dependent upon the weakest point the system at the time in the simulation when the shear stress reached the shear strength.

The second apparent slip mechanism (see Figure 4.14b) occurs for the dry and lubricated PC/PC interfaces. In this case, slip occurs in a localized region near the interface between the two PC slabs. The OPD plots indicate minimal orientation of the bonds along the slip direction. This suggests that the PC slabs move as rigid units during the shear and slip processes. The introduction of an interface between the slabs leads to this behaviour by introducing a weak point in the system, and the incorporation of lubricant weakens the interface further. As such, lubrication is found to have a significant effect on reducing the shear strengths of PC/PC interfaces.

The final slip mechanism (see Figure 4.14c) occurs for interfaces containing a PU component. The calculations show the dry interfaces containing PU and the bulk C18 system have similar, low shear strengths. As such, the introduction of the lubricant does not necessarily cause the lubricated interfaces to be weaker than the dry interfaces in systems containing PU. The results of simulations on the various models containing a PU component indicate the slip

event can occur at the lubricated interface, within the PU slab or a combination of both. The flexibility in the position at which slip occurs is due to the similarities in the strengths of the PU interface and C18, and the slip position observed in any given simulation is likely related to which part of the system was weakest when the shear stress reached the shear strength in those specific cases. Despite the variability in the positions at which slip occurs when PU is present, the slip process itself always involves the alignment of portions of the PU component with the shear direction. Thus, the general slip mechanism for systems containing a PU component likely involves uniform shear of the PU component, as well as the C18 lubricant when present, followed by slip at a position that is weakest when the shear strength is reached in the simulations. The similarity in the strengths of the C18 component and PU-containing interfaces is most likely responsible for the small reduction in shear strengths of interfaces containing PU when the lubricant is introduced.

The different slip mechanisms provided insight into the effects of lubrication on the shear strengths (or alternatively friction forces) associated with slip in this system. The PC/PC interfaces exhibit the slip mechanisms shown in Figure 4.14b, which involves the two PC slabs moving past one another as rigid units. In this case, the shear strength of the system will be dictated by the mechanical properties of the interface between the slabs. In the absence of the lubricant, the PC slabs interact directly, with some entanglement of PC polymers across the interface. Under such circumstances, the strength of the interface will be related to that of the PC component. The addition of the C18 lubricant to the interface reduces the interactions between the PC slabs, causing the mechanical properties of the interface to become increasingly dictated by those of the lubricant as the amount of lubricant present increases. This leads to the significant reduction of the shear strengths of the PC/PC interface with the addition of lubricant.

The strengths of interfaces containing a PU component are not affected significantly by the addition of the lubricant. This is due to the fact that slip occurs via the mechanisms in Figure 4.14c for these interfaces. In this mechanism, the PU component is always directly involved in the slip process. As such, the shear strengths of such systems are determined to a large degree by the strength of PU. In addition, the C18 lubricant and dry PU interfaces have similar shear strengths, and thus the addition of C18 cannot lead to a significant reduction in the strength of the interface.

The identified slip mechanisms also provide some insight into the wear that can occur in these systems. In this context, wear is associated with irreversible changes in the structure of the system. With the exception of bulk PC, all slip mechanisms for systems containing a PC component involving the PC slab(s) moving as solid units with little change in their structure due to shear and/or slip. This indicates that the PC component is resistant to wear, which makes sense in light of the high strength of that material. Meanwhile, all slip mechanisms involving PU involve considerable changes in the structure of the PU component via alignment of the bonds in this component along the slip direction. These structural changes occur at locations throughout the PU component and are not necessarily localized to the regions at which slip occurs. Overall, this indicates that the PU component is sensitive to wear even in the presence of a lubricant. This behaviour likely arises from the low shear strength of the PU component considered in this work.

Chapter 5: Conclusions

Great interest exists in the field of tribology, with the intent of gaining understanding and insight into the mechanisms of friction, lubrication, and wear. These three phenomena affect all devices involving surfaces that move relative to one another, and thus tribology is related to numerous industrial applications. The Xerox Research Centre of Canada (XRCC) has a particular interest in the tribological properties of printer components, with the aim of developing longer-lasting printers. XRCC has particular interest in the slip and wear mechanisms associated with the contact between the commercial photoconducting drum in laser printers and the blade used to clean excess toner off the drum because wear of the cleaning blade generally limits the usable lifetime of the printer. The goal of this thesis was to use chemical simulations to gain insights into the processes that occur during slip at the drum/blade interface and the role of a simple model lubricant at this interface.

The study employed force field (FF) based molecular dynamics (MD) simulations, which have a long history of use in the context of studying tribological phenomena. The simulations employed the Dreiding FF, which is a very generic potential that can only be expected to accurately capture qualitative features of chemical systems. The calculations were performed using model systems representing the commercial photoconducting drum (polycarbonate, referred to as PC throughout), the cleaning blade (polyurethane, referred to as PU throughout) and a simple lubricant (octadecane, referred to as C18 throughout). Bulk and layered models composed of these materials were compressed and sheared to examine how they responded to applied stresses and strains. These simulations provided quantitative data regarding the shear strengths and friction coefficients of these model systems, as well as details regarding the atomic-level changes in structure that occur during slip, which were examined through the use of

order parameters that quantified how the bonds in the system aligned with the slip direction. These details were used to identify slip and wear mechanisms, and to assess the effectiveness of the lubricant.

The calculated shear strengths indicated that PC is significantly more resistant to shear than either of the PU or C18 models. The PC/PC interface was found to have a higher friction coefficient than the other two interfaces examined, which both contained PU. In addition, the introduction of the C18 lubricant significantly reduced the friction coefficient and shear strengths for the PC/PC interface, yet had little effect on these properties for interfaces containing a PU component. In the context of structure, the order parameter indicated that PC was resistant to structural changes when an interface was present, i.e. in all simulations of the PC/PC and PC/PU systems with or without lubricant. Meanwhile, the order parameter suggested that PU was susceptible to structural change in all cases. These details can be understood in terms of the relative strengths of these materials. Essentially, PC possesses a much higher strength than either PU or C18, and thus structural changes occur in the PU or C18 components in interfaces containing PC in contact with these components. Meanwhile, PU and C18 exhibit relatively low shear strengths, and thus systems containing PU and C18 do not exhibit a distinct weak point without substantial levels of lubrication. Instead, the structural changes that accommodate shear occur at locations throughout the PU and/or C18 components in contacts containing these materials. For our models, these results suggest that the PU component is not protected from wear, even when there is no slip motion within the slab. When the C18 component was thicker and more localized, it partially or wholly relocated the slip region from the PU component to the lubricated interface.

The observed behaviour was condensed into three main slip mechanisms. The first mechanism describes slip in the bulk PC or PU systems in which the entire material experiences ordering while undergoing a localized slip event. The second slip mechanism describes slip in the dry and lubricated PC/PC models. Here the PC components experience limited ordering, while the main slip and ordering regions are restricted to the interface and lubricant. The final slip mechanism is more general, and encompasses any layered model containing a PU component. The PU may order and/or slip at any given region from the top to bottom of the slab, and is not necessarily localized. When a C18 component is also present, it does not necessarily exhibit more ordering or slip than the PU component until it is thick and well defined enough to be the weakest part of the model. Any present PC component does not contribute to ordering or slip motion.

Overall, these results indicate that the relative strengths of the materials and lubricants in the contact can play a critical role in achieving effective lubrication to reduce friction and wear. Specifically, the materials forming the contact must both be significantly stronger than the lubricant to ensure that the lubricant corresponds to the weak location in the system. If this is achieved, slip and structural changes will occur preferentially within the lubricant component. Of course, such considerations regarding the mechanical properties of the materials forming the contact must be balanced against other requirements related to the purposes of these materials in the printer itself.

When drawing such conclusions regarding the modifications needed to alter the friction and wear properties of the interface, it is important to keep in mind the limitations of such MD simulations. The following limitations may affect the qualitative outcome of the simulations. One particular obstacle that was encountered was obtaining highly smooth surfaces. The rough

surfaces within the interfaces considered in this study may have increased the shear strengths and may also have required the use of a larger amount of lubricant to form an easily shearable layer between the surfaces. In addition, approximations regarding structure were made when constructing the model systems to conform to computing limitations of the MD simulations, which permit simulations on systems containing a few thousand atoms, and to permit the construction of the amorphous models. These limitations restricted the numbers, sizes and compositions of the polymers used in this study. In particular, the PU component did not have any cross-linking between the polymers, whereas such cross-links are likely present in the elastomer used in printers. The addition of cross-links would likely increase the strength of the PU component, which may render that component less susceptible to ordering and slip. This would be particularly true in the presence of the lubricant. An additional limitation stems from the use of periodic boundary conditions along the *z* direction, which introduced two distinct interfaces. This limitation could be overcome by including lubricant molecules in the center of the cell, as was done here, as well as at the interface between periodically repeated cells. Of course, this approach would require the inclusion of more atoms in the simulation cell.

The following limitations may affect the quantitative results. A very general FF model was used in this work. To achieve results that are meaningful in a quantitative sense, it would likely be necessary to employ a model that had been parameterized specifically for the systems considered here. The systems examined in this study were sheared at strain rates on the order of 10^9 s^{-1}, which are several orders of magnitude greater than strain rates used in experiments, and hence velocity effects may play a role. The simulations employed nanoscopic model systems, whereas shear strength is size dependent. As such, the calculated shear strengths are likely several orders of magnitude higher than the corresponding values one would obtain in

experiments. Scaling laws can be used bridge the gap between the theoretical and experimental values, however. The simulations were performed with the temperature maintained at 300 K, whereas the temperature of printer components may be higher while the printer is running. The C18 lubricant used does not exactly reflect that used in printers, and thus it would be useful to consider a wider range of lubricants in the simulations to better match experimental results. Overcoming these limitations could be the focus of future studies.

References

1. Laboratory, A. N. Large-Scale Manufacturing of Nanoparticulate-Based Lubrication Additives, 2009. U.S. Department of Energy.

2. Holmberg, K., Andersson, P., and Erdemir, A. Global Energy Consumption due to Friction in Passenger Cars. *Trib. Int.* **2012,** *47*, 221-234.

3. Barrett, C. J. Nanotechnology: A Brief Overview. Barrett Research Group. http://barrett-group.mcgill.ca/tutorials/nanotechnology/nano02.htm.

4. Gross, L., Mohn, F., Moll, N., Lijeroth, P., and Meyer, G. The Chemical Structore of a Molecule Resolved by Atomic Force Microscopy. *Science* **2009,** *325*, 1110-1114.

5. Chopinet, L., Formosa, C., Rols, M. P., Duval, R. E., Dague, E. Imaging Living Cells Surface and Quantifying its Properties at High Resolution Using AFM in QI mode. *Micron* **2013,** *48*, 26-33.

6. Baykara, M. Z., Schwendemann, T. C., Altman, E. I., Schwaz, U. D. Three-Dimensional Atomic Force Microscopy - Taking Surface Imaging to the Next Level. *Adv. Mat.* **2010,** *22* (26-27), 2838-2853.

7. Ando, Y., and Ino, J. The Effect of Asperity Array Geometry on Friction and Pull-Off Force. *Journal of Tribology* **1997,** *119*, 781-787.

8. Makaram, P., Joh, J., del Alamo, J. A., Palacios, T., Thompson, C. V. Evolution of Structural Defects Associated with Electrical Degradation in AlGaN/GaN High Electron Mobility Transistors. *Appl. Phys. Lett.* **2010,** *96*, 233509-233509-3.

9. Loyola-Rodriguez, J. P., Zavala-Alonso, V., Reyes-Vela, E., Patino-Marin, N., Ruiz, F., and Anusavice, K. J. Atomic Force Microscopy Observation of the Enamel Roughness and Depth Profile After Phosphoric Acid Etching. *Microscopy* **2010,** *59*, 119-125.

10. Scopelliti, P. E., Borgonovo, A., Indriero, M., Giorgetti, L., Bongiorno, G., Carbone, R., Podesta, A., Milano, P. The Effect of Surface Nanometre-Scale Morphology on Protein Adsorption. *PLoS ONE* **2010,** *5* (7), e11862.

11. Beach, E. R., and Drelich, J. Atomic Force Microscope Pull-off Force Measurements for Insulin in Contact with Acrylonitrile-Butadiene-Styrene and Polypropylene Surfaces at Various Humidities. *J. Adhesion Sci. Tech.* **2012,** *25*, 435-449.

12. Kim, J. K., Lee, D. E., Lee, W. I., and Suh, K. Y. Measurement of Pull-off Force on Imprinted Nanopatterns in an Inert Liquid. *Nanotech.* **2010,** *21,* 295306.

13. Marszalek, P. E., and Dufrene, Y. F. Stretching Single Polysaccharides and Proteins Using Atomic Force Microscopy. *Chem. Soc. Rev.* **2012,** *41,* 3523-3534.

14. Lu, Q., Wang, J., Faghihnejad, A., Zeng, H., and Liu, Y. Understanding the Molecular Interactions of Lipopolysaccharides During E. Coli Initial Adhesion with a Surface Forces Apparatus. *Soft Matter* **2011,** *7,* 9366-9379.

15. Ruths, M., Alcantar, N. N., and Israelachvili, J. N. Boundary Friction of Aromatic Silane Self-Assembled Monolayers Measured with Surface Forces Apparatus and Friction Force Microscopy. *J. Phys. Chem. B* **2003,** *107,* 11149-11157.

16. Valtiner, M., Banquy, X., Kristiansen, K., Greene, G. W., Israelachvili, J. N. The Electrochemical Surface Forces Apparatus: The Effect of Surface Roughness, Electrostatic Surface Potentials, and Anodic Oxide Growth on Interaction Forces, and Friction between Dissimilat Surfaces in Aqueous Solutions. *Langmuir* **2012,** *28* (36), 13080-13093.

17. Kamijo, T., Kasuya, M., Mizukami, M., Kurihara, K. Direct Observation of Double Layer Interactions between the Potential-Controlled Gold Electrode Surfaces Using the Electrochemical Surfaces Forces Apparatus. *Chem. Lett.* **2011,** *40* (7), 674-675.

18. Yu, J, Banquy, X., Greene, G. W., Lowrey, D. D., Irraelachvili, J. N. The Boundary Lubrication of Chemically Grafted and Cross-Linked Hyaluronic Acid in Phosphate Buffered Saline and Lipid Solutions Measured by the Surface Forces Apparatus. *Langmuir* **2012,** *28* (4), 2244-2250.

19. Valtiner, M., Kristiansen, K., Greene, G. W., Israelachvili, J. N. Effect of Surface Roughness and Electrostatic Surface Potentials on Forces Between Dissimilar Surfaces in Aqueous Solution. *Adv. Mat.* **2011,** *23* (20), 2294-2299.

20. Kim, H.-J., Yoo, S.-S., and Kim, D.-E. Nano-Scale Wear: A Review. *Int. J. Precis. Eng. Manuf.* **2012,** *13* (9), 1709-1718.

21. Hsu, S. M., Zhang, J., and Yin, Z. The Nature and Origin of Tribochemistry. *Trib. Lett.* **2002,** *13,* 131-139.

22. Hsu, S. M., and Gates, R. S. Effect of Materials on Tribochemical Reactions Between Hydrocarbons and Surfaces. *J. Phys. D: Appl. Phys.* **2006,** *39,* 3128-3137.

23. Dong, J. X., and Hu, Z. S. A Study of the Anti-Wear and Friction-Reducing Properties of the Lubricant Additive, Nanometer Zinc Borate. *Trib. Int.* **1998,** *31* (5), 219-223.

24. Mattei, L., Puccio, F. D., Piccigallo, B., Ciulli, E. Lubrication and Wear Modelling of Artificial Hip Joints: A Review. *Trib. Int.* **2011,** *44* (5), 532-549.

25. Haseeb, A. S. M. A., Fazal, M. A., Jahirul, M. I., Masjuki, H. H. Compatability of Automotive Materials in Biodiesel: A Review. *Fuel* **2011,** *90* (3), 922-931.

26. Palacio, M., Bhushan, B. A Review of Ionic Liquids for Green Molecular Lubrication in Nanotechnology. *Trib. Lett.* **2010,** *40,* 247-268.

27. Hayes, R. L., Ho, G., Oritz, M., and Carter, E. A. Prediction of Dislocation Nucleation During Nanoindentation of Al_3Mg by the Orbital-Free Density Functional Theory Local Quasicontinuum Method. *Phil. Mag.* **2006,** *86* (16), 2343-2358.

28. Mikulski, P. T., Gao, G., Chateauneuf, G. M., Harrison, J. A. Contact Forces at the Sliding Interface: Mixed Versus Pure Model Alkane Monolayers. *J. Chem. Phys.* **2005,** *122*, 024701.

29. Carkner, C. J. and Mosey, N. J. Slip Mechanisms of Hydroxylated α-Al_2O_3 (0001)/(0001) Interfaces: A First-Principles Molecular Dynamics Study. *J. Phys. Chem. C* **2010,** *114*, 17709-17719.

30. Prandtl, L. Ein Gedankenmodell zur kineticshen Theorie der festen Körper. *Z. Angew. Math. Mech.* **1928,** *8,* 85-106.

31. Tomlinson, G. A. A Molecular Theory of Friction. *Phil. Mag.* **1929,** *7,* 905-939.

32. Briscoe, B. J., and Evans, D. C. B. The Shear Properties of Langmuir-Blodgett Layers. *Proc. R. Soc. Lond. A* **1982,** *380,* 389-407.

33. Derjaguin, B. V. Mechanical Properties of the Boundary Lubrication Layer. *Wear* **1988,** *128,* 19-27.

34. Israelachvili, J. N., and Berman, A. D. Interfacial and Boundary Friction: Molecular Tribology. In *Handbook of Micro/Nanotribology;* Bhushan, B., Ed.; CRC Press: Boca Raton, FL, 1999; p 400.

35. Carkner, C. J., Haw, S. H., and Mosey, N. J. Effect of Advesive Interactions on Static Friction at the Atomic Scale. *Phys. Rev. Lett.* **2010,** *105,* 056102.

36. Belytschko, T., Gracie, R., and Ventura, G. A Review of Extended/Generalized Finite Element Methods for Material Modeling. *Modelling Simul. Mater. Sci. Eng.* **2009,** *17,* 043001.

37. Reddy, J. N., and Gartling, D. K. *The Finite Element Method in Heat Transfer and Fluid Dynamics,* 3rd ed.; CRC Press: Boca Raton, FL, 2010.

38. Bucalem, M. L., and Bathe, K.-J. *The Mechanics of Solids and Structures - Hierarchial Modeling and the Finite Element Solution;* Springer, 2011.

39. Dumont, E. R., Grosse, I. R., Slater, G. J. Requirements for Comparing the Performance of Finite Element Models of Biological Structures. *J. Theo. Biol.* **2009,** *256* (1), 96-103.

40. Panagiotopoulou, O. Finite Element Analysis (FEW): Applying an Engineering Method to Functional Morphology in Anthropology and Human Biology. *Ann. Human Biol.* **2009,** *36* (5), 609-623.

41. Gao, J., Luedtke, W. D., Gourdon, D., Ruths, M., Israelachvili, J. N., and Landman, U. Frictional Forces and Amontons' Law: From the Molecular to the Macroscopic Scale. *J. Phys. Chem. B* **2004,** *108,* 3410-3425.

42. Harrison, J. A., Guangty, G., Schall, J. D., Knippenberg, M. T., and Mikulshi, P. T. Friction Between Solids. *Phil. Trans. R. Soc. A* **2008,** *366,* 1469-1495.

43. Dong, Y., Li, Q., and Martini, A. Molecular Dynamics Simulation of Atomic Friction: A Review and Guide. *J. Vac. Sci. Tech.* **2013,** *31,* 030801.

44. Dai, L., Minn, M., Satyanarayana, N., Sinha, S. K., and Tan, V. B. C. Identifying the Mechanisms of Polymer Friction through Molecular Dynamics Simulation. *Langmuir* **2011,** *27,* 14861-14867.

45. Galuschko, A., Spirin, L., Kreer, T., Johner, A., Pastorino, C., Wittmer, J., and Baschnagel, J. Frictional Forces between Strongly Compressed, Nonentangled Polymer Brushes: Molecular Dynamics Simulations and Scaling Theory. *Lengmuir* **2010,** *26* (9), 6418-6429.

46. Gao, G., Cannara, R. J., Carpick, R. W., Harrison, J. A. Atomic-Scale Friction on Diamond: A Comparison of Different Sliding Directions on (001) and (111) Surfaces Using MD and AFM. *Langmuir* **2007,** *23,* 5394-5405.

47. Brukman, M. J., Gao, G., Nemanich, R. J., Harrison, J. A. Temperature Dependence of Single-Asperity Diamond-Diamond Friction Elucidated Using AFM and MD Simulations. *J. Phys. Chem.* **2008,** *112,* 9358-9369.

48. Jabbarzadeh, A., Atkinson, J. D., and Tanner, R. I. The Effect of Branching on Slip and Rheological Properties of Lubricants in Molecular Dynamics Simulation of Couette Shear Flow. *Trib. Int.* **2002,** *35*, 35-46.

49. Washizu, H., and Ohmori, T. Molecular Dynamics Simulations of Elastohydrodynamic Lubrication Oil Film. *Lub. Sci.* **2010,** *22*, 323-340.

50. Luo, H., Fan, W., Li, Y., and Nan, G. Lubrication Properties of Biodiesel: Experimental Investigation and Molecular Dynamics Simulations. *Appl. Mech. Mat.* **2013,** *316-317*, 1075-1079.

51. Mendonça, A. C. F., Pádua, A. A. H., and Malfreyt, P. Nonequilibrium Molecular Simulations of New Ionic Lubricants at Metallic Surfaces: Prediction of the Friction. *J. Chem. Theory Comput.* **2013,** *9* (3), 1600-1610.

52. Zilibotti, G., and Righi, M. C. Ab Initio Calculation of the Adhesion and Ideal Shear Strength of Planar Diamond Interfaces with Different Atomic Structure and Hydrogen Coverage. *Langmuir* **2011,** *27*, 6862-6867.

53. Kim, K., Lambrecht, W. R. L., and Segall, B. Elastic Constants and Related Properties of Tetrahedrally Bonded BN, AIN, GaN, and InN. *Phys. Rev. B* **1996,** *53* (24), 16310-16326.

54. Wang, L.-F., Ma, T.-B., Hu, Y.-Z., Wang, H., and Shao, T.-M. Ab Initio Study of the Friction Mechanism of Fluorographene and Graphane. *J. Phys. Chem. C* **2013,** *117*, 12520-12525.

55. Haw, S. H. and Mosey, N. J. Tribochemistry of Aldehydes Sheared between (0001) Surfaces of α-Alumina from First-Principles Molecular Dynamics. *J. Phys. Chem. C* **2012,** *116*, 2132-2145.

56. Kawahara, I. Cleaning Member, Cleaning Device, Assembly, and Image Forming Device. US 8290391 B2, October 16, 2012.

57. Thayer, B. E., Burry, A. M., Zona, M. F. Apparatus and Method for Xerographic Printer Cleaning Blade Lubrication. US 8406675 B2, March 26, 2013.

58. Burek, J. A. "Laser printers are second cousins to photocopiers." How It Works: Laser Printer.

59. Thayer, B. E., Seyfried, R. W. Variable Interference Cleaning Blade Method. US 7917049 B2, March 29, 2011.

60. Plimpton, S. Fast Parallel Algorithms for Short-Range Molecular Dynamics. *J. Comp. Phys.* **1995,** *117,* 1-19.

61. Kazanjian, A. R. Review of Properties of Polycarbonate Resins. *Polymer-Plastics Technology and Engineering* **1973,** *2* (2), 123-160.

62. Schlueter, E. L. Jr., Smith, J. F., Sharf, L. M. High Wear Resistance Low Compression Set Polyurethane. US 5656720, August 12, 1997.

63. Hu, N.-X., Liu, Y., Skorokhod, V., Wu, Y., Klenkler, R. A. Apparatus and Methods for Delivery of a Functional Material to an Image Forming Member. US 20120201585 A1, August 9, 2012.

64. Frisch, A. E., Dennington, R. D., Keith, T. A., Neilsen, A. B. and Holder, A. J. *GaussView, revision 3.0.8, Gaussian, Inc.;* Pittsburgh, PA, 2003.

65. Fitzgerald, E. R., Fitzgerald, R. E. Automated Measurement System for Dynamic Mechanical Properties of Viscoelastic Materials. *Polymer Bulletin* **1987,** *18* (2), 167-174.

66. Martyna, G. J., Tobias, D. J., Klein, M. L. Constant Pressure Molecular Dynamics Algorithms. *J. Chem. Phys.* **1994,** *101* (5), 4177-4189.

67. Mayo, S. L., Olafson, B. D., Goddard, Wm. A. III. Dreiding: A Generic Force Field for Molecular Simulations. *J. Phys. Chem.* **1990,** *94* (96), 8897-8909.

68. Breneman, C. M., Wilberg, K. B. Determining atom-centered monopoles from molecular electrostatic potentials - the need for high sampling density in formamide conformational-analysis. *J. Comp. Chem.* **1990,** *11,* 361-373.

69. Montgomery, J. A. Jr., Frisch, M. J., Ochterski, J. W., and Petersson, G. A. A complete basis set model chemistry. VI. Use of density functional geometries and frequencies. *J. Chem. Phys.* **1999,** *110,* 2822-2827.

70. Montgomery, J. A. Jr., Frisch, M. J., Ochterski, J. W., and Petersson, G. A. A complete basis set model chemistry. VII. Use of the minimum population localization method. *J. Chem. Phys.* **2000,** *112,* 6532-6542.

71. Sigma-Aldrich. www.sigmaaldrich.com.

72. Caudwell, D. R., Trusler, J. P. M., Vesovic, V., and Wakeham, W. A. The Viscosity and Density of n-Dodecane and n-Octadecane at Pressures up to 200 MPa and Temperatures up to 473 K. *Int. J. Thermophys.* **2004,** *25* (5).

73. Ghosh, S. K. A Model for the Orientational Order in Liquid Crystals. *Il Nuovo Cimento D* **1984,** *4* (3), 229.

74. Mosey, N. J., and Carter, E. A. Shear Strength of Chromia Across Multiple Length Scales: An LDA + U Study. *Acta Materialia* **2009,** *57,* 2933-2943.

75. MatWeb Material Property Data. www.matweb.com.